

## INFORMATION TO USERS

This manuscript has been reproduced from the microfilm master. UMI films the text directly from the original or copy submitted. Thus, some thesis and dissertation copies are in typewriter face, while others may be from any type of computer printer.

**The quality of this reproduction is dependent upon the quality of the copy submitted.** Broken or indistinct print, colored or poor quality illustrations and photographs, print bleedthrough, substandard margins, and improper alignment can adversely affect reproduction.

In the unlikely event that the author did not send UMI a complete manuscript and there are missing pages, these will be noted. Also, if unauthorized copyright material had to be removed, a note will indicate the deletion.

Oversize materials (e.g., maps, drawings, charts) are reproduced by sectioning the original, beginning at the upper left-hand corner and continuing from left to right in equal sections with small overlaps. Each original is also photographed in one exposure and is included in reduced form at the back of the book.

Photographs included in the original manuscript have been reproduced xerographically in this copy. Higher quality 6" x 9" black and white photographic prints are available for any photographs or illustrations appearing in this copy for an additional charge. Contact UMI directly to order.

# UMI

A Beil & Howell Information Company  
300 North Zeeb Road, Ann Arbor MI 48106-1346 USA  
313/761-4700 800/521-0600



RICE UNIVERSITY

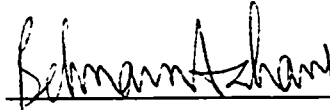
**Principle and Practice of Optical Code-Division  
Multiple Access Communication**

by

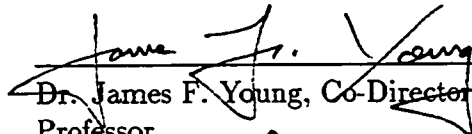
**Lim Nguyen**

A THESIS SUBMITTED  
IN PARTIAL FULFILLMENT OF THE  
REQUIREMENTS FOR THE DEGREE  
**Doctor of Philosophy**

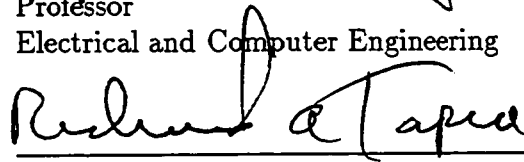
APPROVED, THESIS COMMITTEE:



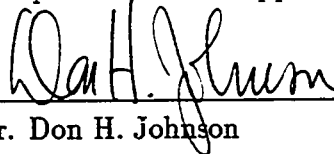
Dr. Behnaam Aazhang, Director  
Professor  
Electrical and Computer Engineering



Dr. James F. Young, Co-Director  
Professor  
Electrical and Computer Engineering



Dr. Richard A. Tapia  
Professor  
Computational and Applied Mathematics



Dr. Don H. Johnson  
Professor  
Electrical and Computer Engineering

Houston, Texas

May, 1996

**UMI Number: 9631105**

---

**UMI Microform 9631105**  
**Copyright 1996, by UMI Company. All rights reserved.**

**This microform edition is protected against unauthorized  
copying under Title 17, United States Code.**

---

**UMI**  
**300 North Zeeb Road**  
**Ann Arbor, MI 48103**

# **Principle and Practice of Optical Code-Division Multiple Access Communication**

Lim Nguyen

## **Abstract**

This research examines the theoretical and experimental aspects of code-division multiple access (CDMA) communication in the incoherent, or direct detection, optical domain. We develop new modulation and detection principles that permit all-optical implementation of the bipolar,  $+1/-1$ , code and correlation detection available in the radio frequency (RF) CDMA systems. This is possible in spite of the non-negative, or unipolar,  $+1/0$ , nature of the incoherent optical system that only detects and processes the signal intensity. The unipolar optical system using the new principles is equivalent to the bipolar RF system in that the correlation properties of the codes are completely preserved.

The optical CDMA system can be realized either in time or frequency domain encoding with all-optical components. All-optical implementation is extremely important in practice because the symbol rates of the individual users are far less than the bandwidth of the optical fiber. Frequency domain or spectral amplitude encoding significantly increases the number of available codewords that can be assigned to the subscribers, and is the focus of this work.

The spectral amplitude encoding uses incoherent, broad bandwidth superfluorescent fiber source (SFS) that has the limiting signal-to-noise ratio characteristics associated with thermal light. Measurements of the photodetector illuminated by an erbium-doped SFS confirm that the noise distribution follows a negative binomial probability mass function as predicted for the photoelectron counting statistics of thermal light. The analysis based on this statistical model results in improved performance over the Gaussian assumption, which predicts a performance floor. The analysis also shows that optical CDMA system, even with the use of orthogonal codes, is interference limited.

We implement an experimental prototype system that demonstrates the first use of bipolar codes for spectral amplitude CDMA. The experimental results validate the modulation and detection principles and demonstrate the feasibility of optical CDMA systems based on those principles.

## Acknowledgments

I would like to express my gratitude to my advisors, Dr. Aazhang and Dr. Young, whose guidance and patience have been enormously critical to my study. Their enthusiasms have made the research effort a tolerable endeavor.

I would also like to extend my gratitude to Dr. Johnson and Dr. Tapia for their precious time and effort to graciously serve on my doctoral committee. I also thank them for introducing the subjects of detection, estimation and optimization to me.

I appreciate the friendship of my fellow students, with special thanks to Tasshi Dennis and Yile Guo for their collaboration. I also would like to thank Dr. Wilson and Bruce Brinson for their help in various aspects of the experiments.

I would like to acknowledge the U.S. Air Force Phillips Laboratory and Palace Knight program that provided the partial support for my study. I appreciate the assistance of Frank Fisk and Karl Gass from Kirtland AFB and Lu Voronyak from Randolph AFB.

My deepest thanks belong to my parents whose boundless sacrifices continue to be my source of inspiration and motivation. Their love, and the unyielding support of my brothers and sisters, are immeasurable.

Finally, this research journey would have been absolutely meaningless without my wife, Lieu, and sons, Albert and Arthur, standing by and going through it all with me in so many ways.

to my parents

Lan and Canh Nguyen



in the memory of my sister

Thanh Thuy

# Contents

Abstract	ii
Acknowledgments	iv
List of Illustrations	x
<b>1 Introduction</b>	<b>1</b>
1.1 Preliminaries . . . . .	1
1.2 Research Outline . . . . .	9
<b>2 Optical CDMA with Bipolar Codes</b>	<b>13</b>
2.1 Bipolar Correlation in a Unipolar System . . . . .	14
2.2 Modulation and Detection Principles . . . . .	16
2.3 Multi-channel Optical Communication . . . . .	19
2.3.1 System Model . . . . .	21
2.3.2 Likelihood Ratio Decision . . . . .	24
2.3.3 Correlations of Multi-dimensional Codes . . . . .	28
2.3.4 Remark . . . . .	30
2.4 Implementation . . . . .	30
2.4.1 Time Domain Encoding . . . . .	32
2.4.2 Spectral Amplitude Encoding . . . . .	34
2.5 Summary . . . . .	37
<b>3 Photoelectric Current Distribution of a SFS</b>	<b>39</b>

3.1	Theoretical Basis . . . . .	40
3.2	Experimental Description . . . . .	43
3.3	Measurement Results . . . . .	47
3.3.1	Histograms . . . . .	48
3.3.2	Moment Analysis . . . . .	54
3.4	Remarks . . . . .	56
3.5	Summary . . . . .	57
<b>4</b>	<b>Performance of Spectrum-sliced WDMA</b>	<b>58</b>
4.1	Spectrum-sliced WDMA System Model . . . . .	59
4.2	BER Analysis . . . . .	62
4.3	Numerical Examples . . . . .	66
4.4	Performance under Gaussian Background Noise . . . . .	68
4.5	Remarks . . . . .	75
4.6	Summary . . . . .	76
<b>5</b>	<b>Performance of Spectral Amplitude CDMA</b>	<b>78</b>
5.1	System Description . . . . .	79
5.2	SNR Analysis . . . . .	85
5.3	Probability of Error Analysis . . . . .	91
5.4	Summary . . . . .	97
<b>6</b>	<b>Experimental Demonstration of Optical CDMA</b>	
	<b>System</b>	<b>98</b>
6.1	Experimental Description . . . . .	98
6.2	System Characterization . . . . .	108

6.3	Measurements . . . . .	111
6.4	Results . . . . .	114
6.5	Discussions . . . . .	118
6.6	Summary . . . . .	120
<b>7</b>	<b>Conclusions</b>	<b>121</b>
	<b>Bibliography</b>	<b>126</b>

## Illustrations

1.1	Optical CDMA in a fiber optic LAN. . . . .	2
2.1	Bipolar correlation in a unipolar system. . . . .	15
2.2	Block diagrams of the encoder and the decoder. . . . .	18
2.3	Differential decoder configuration. . . . .	20
2.4	Multi-channel optical communication system. . . . .	22
2.5	Time and frequency domain encoding. . . . .	31
2.6	Schematic diagram of time domain encoder and decoder. . . . .	33
2.7	Schematic diagram of an example all-optical spectral encoder. . . . .	35
3.1	Experimental configuration to measure the photoelectric current distribution. . . . .	46
3.2	Background noise distribution of the measurement system. . . . .	49
3.3	Sampled signal fluctuation of the detector output voltage. . . . .	51
3.4	Distribution of the voltage signal fluctuation. . . . .	52
3.5	Normalized moments. . . . .	55
4.1	Block diagram of a spectrum-sliced WDMA system. . . . .	60
4.2	Number of channels in a spectrum-sliced WDMA system. . . . .	67
4.3	BER comparison with an ideal receiver. . . . .	69

4.4	BER comparison with Gaussian background noise. . . . .	72
5.1	Incoherent optical CDMA system based on spectral amplitude encoding of bipolar codes. . . . .	80
5.2	Encoding of a broadband spectrum. . . . .	81
5.3	Block diagram of a binary FSK, spectrum-sliced WDMA system. . .	84
5.4	SNR comparison of spectral CDMA and FSK-WDMA. . . . .	90
5.5	Probability of error versus the number of users. . . . .	94
5.6	Probability of error versus mode number per chip, $M_o$ . . . . .	95
5.7	Probability of error versus optical power. . . . .	96
6.1	Experimental setup of the spectral amplitude CDMA system prototype.	99
6.2	ASE spectrum of erbium-doped SFS. . . . .	101
6.3	Encoder and decoder configurations. . . . .	102
6.4	Geometrical configuration of the spectrum processor. . . . .	103
6.5	Spectral amplitude code patterns. . . . .	106
6.6	Amplitude mask patterns. . . . .	107
6.7	Relative dispersion of the encoder/decoder system. . . . .	109
6.8	Resolution of the encoder/decoder system. . . . .	110
6.9	ASE spectrum measurements. . . . .	112
6.10	Encoded and decoded ASE spectra. . . . .	113
6.11	Correlation of the spectral codes. . . . .	115
6.12	Effect of the multiple-access interference. . . . .	117

# Chapter 1

## Introduction

In this study we examine the theoretical and experimental aspects of code-division multiple access (CDMA) communication in the incoherent, or direct detection, optical domain. We begin by motivating the problem and then consider new modulation and detection principles for incoherent optical CDMA systems that employ bipolar codes and correlation detection. An overview of the performance analysis will be given, as well as some descriptions of the experiments and laboratory demonstrations of the proposed principles.

### 1.1 Preliminaries

In a communication network, there are many simultaneously active users out of a larger pool of subscribers with authorized access to the network. In the most general network connectivity, each user can transmit and receive information to and from every other user, as illustrated in Figure 1.1. The fiber optic local area network (LAN) is modeled as a passive  $J \times J$  star coupler that provides network connections between the  $J$  users. The network resources therefore must be shared among the users in this multiple access scenario, with the bandwidth being one of the fundamentally impor-

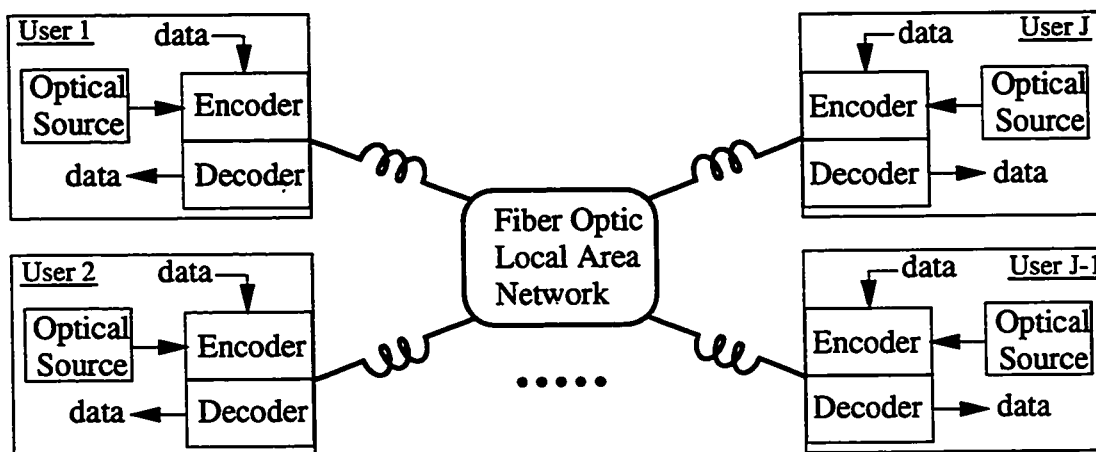


**Figure 1.1** Optical CDMA in a fiber optic LAN.

The fiber optic LAN is modeled as a passive  $J \times J$  star coupler that provides full connectivity between the users.



tant resources. In this respect, the optical domain presents great potential due to the enormous bandwidth at the optical frequency. For example, the low-loss window of the single-mode optical glass fiber has a bandwidth of about 25,000 GHz each at the 1300 nm and 1550 nm wavelength windows. Graded-index plastic fiber, currently achieving a more modest 20 GHz bandwidth over a distance of 100 m, is becoming attractive due to its potentially lower implementation cost for short-distance LAN applications.

The usual approach to optical communication system design has been to apply the techniques of the RF and microwave system where the bandwidth resource is at a premium; the highest microwave frequency is only a small fraction of the bandwidth of the optical fiber. The limiting speed of the electronic components, typically a few GHz in practice, however places a considerable restriction on the optical system performance in term of the bandwidth utilization. In order to realize the potential of the optical fiber, optical communication system design therefore should be based on the unique characteristics of the optical domain. It should enable the use of the virtually-unlimited bandwidth resource of the fiber medium to address some of the network issues, specifically the multiple access, or multi-user, requirement. That is, how the interference from the simultaneously active users can be controlled so that they can co-exist.

One approach to address the multi-user requirement is the frequency-division multiple access (FDMA) protocol. In FDMA, the bandwidth is partitioned into non-

overlapping segments and assigned to the subscribers in a predetermined manner. Each subscriber has the interference-free use of his allocated bandwidth segment at all time, much like the radio broadcasting station system. If the subscriber access to the network is bursty, FDMA is not efficient in the bandwidth utilization. Moreover, as new subscribers arrive, the bandwidth resource must be re-allocated which may not be feasible nor desirable.

Another more flexible multi-user protocol is time-division multiple access (TDMA). Here, non-overlapping, band-limited time slots are assigned to the subscribers so that each has the interference-free use of the entire bandwidth during the allocated time slot. New subscribers can be accomodated simply by increasing the number of time slots. Like FDMA, this protocol has inefficient bandwidth utilization in a bursty network. Each subscriber has very short duty cycle transmission and requires time slot synchronization for proper operation. Since only one user is allowed to access the network at any time, this protocol is really a coordinated single user system. Common variants of this approach are the token-ring and Ethernet networks that depend on a higher level of protocols for multiple-access collision avoidance and resolution.

Code-division multiple access is the most flexible protocol; it allows each subscriber the full use of the bandwidth resource at all times. The subscribers are differentiated from one another by the use of distinct signature sequences. The multiple-access interference (MAI) due to the time and frequency overlapping signals from the

simultaneously active users is controlled by choosing signature sequences that have ideally zero, or low, crosscorrelation values. CDMA is highly suited for bursty networks; its full use of the bandwidth resource results in good system performance that degrades gracefully as the number of active users increases. This interference-limited performance, coupled with other attributes that have proven effective in combating the mobile communication environment, has caused CDMA to receive considerable attention for the next generation of digital cellular phone technologies.

In the optical domain, FDMA is commonly known as wavelength-division multiple access (WDMA). The number of wavelengths or channels is small due to the wavelength stability and tuning range of the diode lasers. Non-linear effects in the optical fiber, such as four-wave mixing, contribute to place an upper limit on WDMA system. Optical TDMA requires short-pulsed diode lasers (or high-speed diode laser/modulator) whose transform-limited bandwidth is far less than fiber bandwidth. The pulse propagation suffers from the dispersion effect in the optical fiber, limiting the transmission distance unless nonlinear techniques like solitons or dispersion compensations are used. Thus, besides the inherent inefficiency in the bandwidth utilization, these protocols have additional limitations when introduced to the optical fiber medium.

The desirable characteristics of the CDMA protocol make it an attractive approach toward the goal of using the optical bandwidth resource to meet the practical network requirement of supporting a large pool of subscribers, not all of whom require access

to the network at the same time, while providing access to many simultaneously active users. Historically, CDMA is an application of the secured and anti-jamming communication techniques developed for the military in the RF domain. It is based on the spread spectrum principles that distribute the signal energy of the user over a bandwidth much larger than required by the binary information symbol rate. The bandwidth expansion is accomplished by modulating the information symbol with the so-called spreading codes, or signature sequences, that are uniquely assigned to different users. This allows the receiver to differentiate them by means of the correlation detection. The huge bandwidth of the optical fiber relative to the symbol rate means that the size of the code book can be very large. Practically, in order to realize this bandwidth advantage the encoding (bandwidth expansion) and correlation (bandwidth contraction) operations on the signal at the transmitter and receiver, respectively, must be performed optically to circumvent the speed limitation of the electronic system which can then be allowed to operate at the much slower symbol rate.

A comprehensive reference on the spread-spectrum communication techniques in the RF domain can be found in [1] and [2]. Increasingly, these techniques are finding applications in the digital cellular CDMA telephone system [3]. The performance characterization of CDMA systems in the RF domain has been well-studied for additive Gaussian noise [1], [4], [5], impulsive [6], [7], multipath and fading channels [8], [9], [10]. These studies have considered the conventional matched filter or cor-

relation detector, as well as various optimal [11] and suboptimal multi-user detector schemes [12], [13], [14], [15] that yield improved performance at the expense of an increase in the receiver complexity.

The success of the RF CDMA system depends crucially on the use of well designed bipolar sequences with good correlation properties [16], [17]. There has been a large body of work devoted to the search for good codes; among them are the  $m$ -sequence, Gold and Kassami sequences, Barker and Walsh codes. These sequences of  $+1/-1$  values exist in the RF domain because the electromagnetic field, or the phase of the signal, can be detected. The application of CDMA techniques of the RF system to the optical domain, however, has not been very successful, primarily due to the non-negative nature of the direct detection optical channel. By direct detection, we mean that the optical field is square-law detected by a photodetector; thus only the signal intensity can be detected and processed. As a result, in incoherent optical systems only unipolar sequences that take on  $+1/0$  values exist. The bipolar codes of the RF domain were therefore thought to be inapplicable to the optical system. With correlation detection, the unipolar spreading codes are restricted to be sparse or optical orthogonal codes (OOC's) [18], [19], [20]. In order to have good correlation properties, these codes generally have low weight relative to their length and therefore are inefficient. Also, the number of available codes are too few for practical application.

Research in optical CDMA has been focusing in two general areas: studying systems that employ unipolar codes, or adapting bipolar codes to the optical domain

[21]. Systems that employ unipolar codes have been proposed for coherent and non-coherent correlation detectors in [22], [23], [24], [25], and subsequently studied using the Poisson photodetection model [26]. The system capacity has been shown to increase by combining CDMA with M-ary pulse-position modulation (PPM) at the expense of an increase in the system complexity [27]. High performance detection via optimum demodulation was developed in [28], with the multi-user detection scheme considered in [29]. Unfortunately, these studies indicate that such systems are not very practical due either to the lack of good codes or to the design complexity.

The second research direction in optical CDMA has concentrated in adapting the bipolar codes, either by using coherent phase or subcarrier modulation and demodulation, or by employing a balanced receiver. The former approach [30], [31], [32], [33] is simply a direct extension of the RF techniques with an optical carrier, and requires electronic correlation. The latter approach relies on sequence inversion keying (SIK) that transmits the unipolar version of the bipolar codes, followed by a unipolar-bipolar correlation with a balanced receiver [34], [35], [36], [37]. Since the true bipolar codes and correlations are not employed, some sort of balanced or special codes, offset removal, or electronic correlation are required that precludes a general, all-optical implementation of the bipolar codes and correlations.

Direct detection has the extremely desirable attribute that all-optical processing of the transmitted and received signals is feasible; it also does not require a coherent phase reference. This enables the interface between the electronic symbol source

and the optical system to operate at the symbol rate. The restriction on the optical bandwidth utilization imposed by the limiting speed of the electronic components is thus completely eliminated. What is needed, therefore, is a modulation and detection method that puts the bipolar codes of the RF domain to use in the optical domain without losing any of their correlation properties. Moreover, in order to make optical CDMA system a practical reality, this method should also lend itself toward mitigating the problems associated with the optical fiber medium and with the limitation imposed by practical light sources. The investigation of such a method and its practical implementation, then, are the aims of this research effort.

## 1.2 Research Outline

In Chapter 2, we propose new modulation and detection principles that permit all-optical implementation of the bipolar,  $+1/-1$ , codes and correlation detector that have been developed for the RF systems. This is possible in spite of the unipolar nature of the incoherent optical systems. The optical CDMA system is equivalent to its RF counterpart in that the correlation of the bipolar codes is completely preserved. The proposed principles can be interpreted as the generalization of the binary PPM or FSK (frequency-shifted keying) modulation systems. We develop a multi-channel optical communication model for the new modulation and detection methods that includes the shot noise nature for the photodetection process. We show that the proposed principles are the result of the optimum detection based on the likelihood

ratio test for a multi-channel optical system that distributes the spreading codes over many channels to overcome the restrictions on the signal set. Based on the modulation and detection principles that have been developed, an optical CDMA scheme is realized by encoding the spectral amplitude of incoherent, broad bandwidth light sources such as the superfluorescent fiber source. This approach directly manipulates the amplitude spectrum of the light according to the binary symbol values in a manner that is decoupled from the symbol rate. As a result, with spectral encoding, the users may transmit their data at variable rates with no modification to the spreading codes being used. Additionally, cyclic shifts of codes that have low offset autocorrelation values can be used. This property will significantly increase the number of available codewords that can be assigned to the network subscribers.

Since the SFS is used as the transmitting light source, a proper analysis of the system performance requires an accurate statistical model for the detector current due to the SFS. The prevailing Gaussian assumption for the current noise statistics has led to the non-physical prediction that the performance of a WDMA system employing the SFS cannot be improved by increasing the optical power. Chapter 3 reports the experiments to measure the distribution of the photoelectric current from a photodiode under illumination from a spectrum-sliced, erbium-doped SFS. The results show that the statistical distribution of the current fluctuation is in fact non-Gaussian. It follows a negative binomial (NB) distribution that describes the photoelectron



counting statistics of thermal light. This is consistent with the statistical model of the SFS as a thermal light source.

We consider the spectrum-sliced WDMA system that employs the SFS in chapter 4. The limiting signal-to-noise ratio (SNR) characteristics associated with the SFS result in the prediction of a BER floor when invoking the Gaussian assumption. However, the analysis based on the NB noise statistics shows that the system performance improves as the received power increases, despite the limiting SNR that is proportional to the ratio of the spectral bandwidth and the symbol rate. This has significant implication for practical spectral amplitude CDMA systems: given a symbol rate and a source bandwidth, trade-offs between the bandwidth of the spectral chip, hence the code length and the number of subscribers, and the received power are possible.

The performance of spectral amplitude CDMA system is considered in Chapter 5. The analysis is based on the NB statistics and the additive light model to account for the thermal characteristics of the SFS. The SNR and the probability of error were computed and compared to binary FSK, spectrum-sliced WDMA system. The results demonstrated the interference-limited behavior of CDMA that places a performance penalty on the system due to the thermal nature of the SFS. Chapter 6 describes a free-space, experimental CDMA system prototype that employs an erbium-doped SFS. To our knowledge it is the first to demonstrate the use of bipolar codes for spectral amplitude CDMA. The measurement results verify the relative correlations of

the example bipolar codes to show that the information symbol can be recovered. The multiple-access interference has also been shown to be rejected. The prototype results validate the modulation and detection methods and demonstrate the practicality of optical CDMA system based on those principles.

The conclusion of the study is presented in Chapter 7. The modulation and detection principles that we have developed have finally placed optical CDMA on the same footing as its RF counterpart in terms of the spreading codes utilization, while still retaining the inherent advantages of the optical domain. We discuss future research issues that concern the improvement in the design and performance of the prototype system. We conclude with a few comments on a number of potential research topics that could be undertaken from the work described herein.

## Chapter 2

### Optical CDMA with Bipolar Codes

The application of CDMA techniques developed in the radio domain to optical fiber LANs has been a research topic of considerable interest. Practically, a LAN must support a large pool of subscribers, not all of whom require access to the network at the same time, while providing access to many simultaneously active users. The success of the direct-sequence CDMA systems in the radio domain is a direct result of the use of well-designed bipolar,  $+1/-1$ , codes and bipolar correlation detectors to control the multiple access interference from other users to the desired user. However, due to the positive nature of the incoherent optical channel in which only the intensity of the signal is detected, it is generally thought that the bipolar codes are inapplicable to the incoherent optical CDMA systems. Various schemes that have been proposed [35], [36], [37] require balanced or special codes, offset removal, or electronic correlations that preclude the general, all-optical, application of the bipolar codes. In this chapter, we present new modulation and detection methods that allow all-optical implementation of the bipolar codes and correlation detectors in the incoherent optical domain. A multi-channel optical communication system that includes the shot noise nature for the photodetection process is described that provides a model for the new

modulation and detection principles. We describe an optical CDMA scheme that is based upon spectral amplitude encoding of a broadband source using the principles that have been developed.

## 2.1 Bipolar Correlation in a Unipolar System

We define a unipolar system to be a non-negative system whose spreading codes take on the values of +1 or 0. The incoherent, or direct detection, optical channel is an example of a unipolar system. By direct detection, we mean that the optical field is square-law detected by the photodetector; thus only the signal intensity can be detected and processed. In order to apply the bipolar codes in a unipolar system, the question of considerable interest is the computation of its correlation using only unipolar operations. Computing the correlation between two sequences is commonly referred to as the shift and multiply-add, or multiply-accumulate, operation. Figure 2.1 illustrates a zero-shift correlation of the example bipolar codes of length 11:  $X_1 = (1, -1, 1, 1, -1, 1, -1, 1, -1, -1, 1)$  and  $X_2 = (1, 1, 1, -1, 1, -1, 1, 1, -1, 1, -1)$ . The multiply-add operation (a) gives  $R_{12}(0) = -3$ . This result can also be computed with the unipolar operations of counting and summation, as shown in (b). By separately counting the total numbers of matched and mismatched polarities of the code elements, followed by a difference operation, the same correlation value is obtained. Thus, the bipolar codes and their correlation properties can be fully preserved in the unipolar system. This is accomplished by recoding the bipolar code  $X$  to two comple-

The multiply-add operation of the bipolar system (a) can be computed via countings and summations, followed by a difference operation in a unipolar system (b).

mentary unipolar codes  $U, \bar{U}$  of the same length according to the polarity of  $X$ . The bipolar correlation is then computed by a “compound” correlator that operates on  $U, \bar{U}$  and consists of four unipolar correlators, two summations, and one subtraction. This representation is formalized in the next section.

## 2.2 Modulation and Detection Principles

Consider a bipolar sequence  $x(n)$  of period  $N$  that takes values from  $\{-1, 1\}$ .  $x(n)$  can be expressed as the difference of two unipolar sequences of the same period, say  $u(n)$  and  $\bar{u}(n)$ , that take values from  $\{0, 1\}$ , where  $u(n)$  is obtained from  $x(n)$  by replacing each  $-1$  with  $0$  and  $\bar{u}(n)$  is its binary complement. That is:  $x(n) = u(n) - \bar{u}(n)$ , with  $u(n) \triangleq [1 + x(n)]/2$ , and  $\bar{u}(n) \triangleq [1 - x(n)]/2$ . Similarly, let  $v(n)$  be the unipolar sequence obtained from another bipolar sequence  $y(n)$ , also of period  $N$ . Then the periodic and aperiodic crosscorrelation functions of  $x(n)$  and  $y(n)$  can be computed in terms of the unipolar crosscorrelation functions as follows:

$$\begin{aligned} \theta_{x,y}(l) &\triangleq \sum_{n=0}^{N-1} x(n)y(n+l) \\ &= [\theta_{u,v}(l) + \theta_{\bar{u},\bar{v}}(l)] - [\theta_{u,\bar{v}}(l) + \theta_{\bar{u},v}(l)] \end{aligned} \quad (2.1)$$

$$\begin{aligned} C_{x,y}(l) &\triangleq \begin{cases} \sum_{n=0}^{N-1-l} x(n)y(n+l), & 0 \leq l \leq N-1 \\ \sum_{n=0}^{N-1+l} x(n-l)y(n), & 1-N \leq l \leq 0 \\ 0, & |l| \geq N \end{cases} \\ &= [C_{u,v}(l) + C_{\bar{u},\bar{v}}(l)] - [C_{u,\bar{v}}(l) + C_{\bar{u},v}(l)] \end{aligned} \quad (2.2)$$

The modulation and detection principles based on the above results are illustrated in Figure 2.2. We describe their operation in the time domain for simplicity and consistency with the conventional description of CDMA techniques where the time waveform is encoded. The operation of these principles can be realized either in time or spectral amplitude encoded systems and their implementations are described in Sec. 2.4. Referring to Figure 2.2, the transmitted symbols are encoded by two intensity modulation waveforms arriving at the receiver:

$$s_A(t) = \Lambda \left\{ \sum_{i=-\infty}^{\infty} [b_i \sum_{n=0}^{N-1} U(n) \Pi_{T_c}(t - nT_c - iT) + \bar{b}_i \sum_{n=0}^{N-1} \bar{U}(n) \Pi_{T_c}(t - nT_c - iT)] \right\}, \quad (2.3)$$

$$s_B(t) = \Lambda \left\{ \sum_{i=-\infty}^{\infty} [b_i \sum_{n=0}^{N-1} \bar{U}(n) \Pi_{T_c}(t - nT_c - iT) + \bar{b}_i \sum_{n=0}^{N-1} U(n) \Pi_{T_c}(t - nT_c - iT)] \right\}. \quad (2.4)$$

$b_i$  is the binary,  $+1/0$ , symbol and  $\Pi_{T_c}(t)$  is the unit rectangular chip waveform that is zero outside  $[0, T_c)$ .  $T$ ,  $T_c$  are the symbol and chip duration, respectively, and  $\Lambda$  is the chip intensity. The signature codes  $U$  and  $\bar{U}$  are obtained from a length- $N$  bipolar codeword as described previously. We denote a codeword by an upper case letter -  $U$ , to distinguish it from the sequence, denoted by a lower case letter -  $u$ , that consists of a series of codewords. The cross-bar switch transmits the 2-tuple  $(U, \bar{U})$  for, say, symbol "1" and  $(\bar{U}, U)$  for symbol "0". The decoder structure is in accordance with (2.1) and (2.2) using two identical matched filter pairs. Each pair has

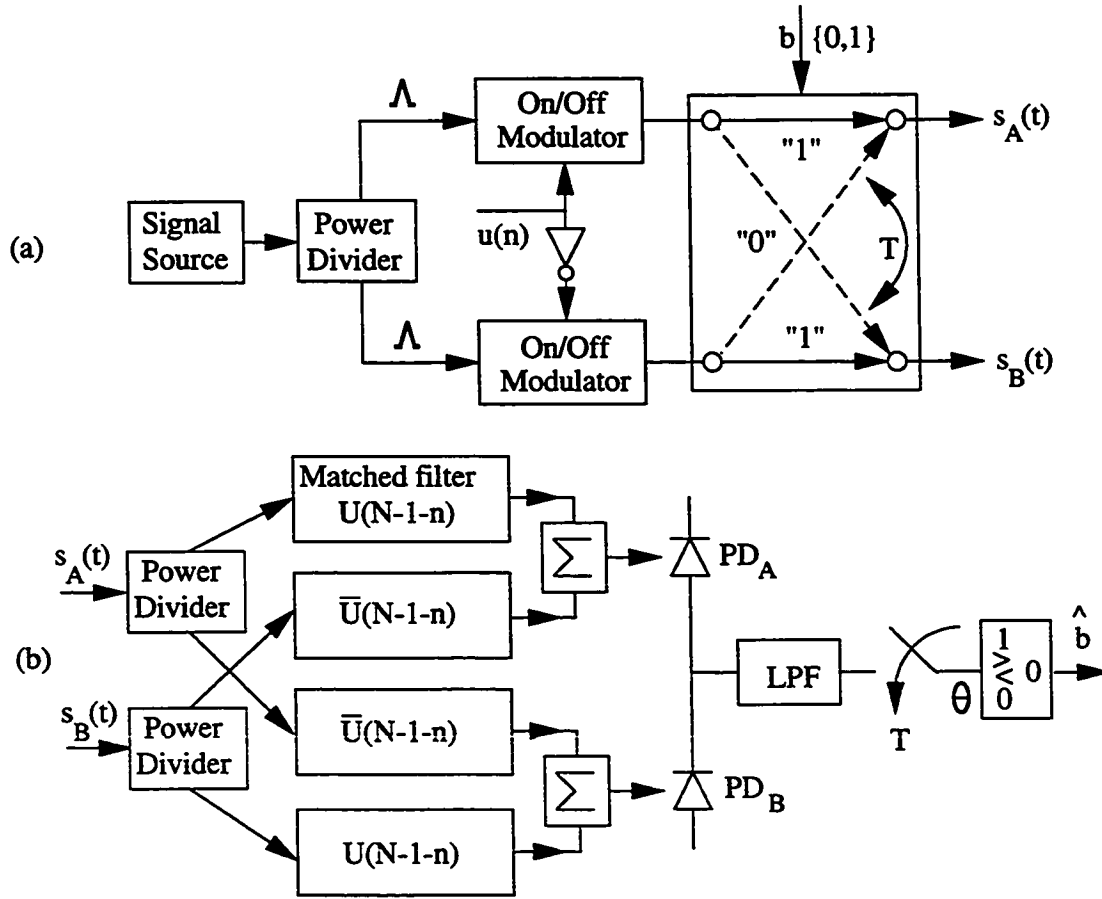


**Figure 2.2** Block diagrams of the encoder and the decoder.

By means of the cross-bar switch, the encoder transmits  $(U, \bar{U})$  for, say, symbol "1", and  $(\bar{U}, U)$  for symbol "0" (a). The impulse responses of the matched filters in the decoder are matched to  $U$  and  $\bar{U}$  (b). The output of the balanced photodetector pair is proportional to the bipolar correlation between the codes of the encoder and the decoder, as given by (2.1) and (2.2).



two unipolar matched filters with impulse responses  $h(t) = \sum_{n=0}^{N-1} U(N-1-n)\Pi_{T_c}(t-nT_c)$ , and  $\bar{h}(t) = \sum_{n=0}^{N-1} \bar{U}(N-1-n)\Pi_{T_c}(t-nT_c)$ . The outputs of each of the two complementary unipolar correlator pairs are optically summed and photodetected. The two photodiodes are connected in a balanced configuration so that their outputs are subtracted. The output current of the balanced detectors is therefore proportional to the bipolar correlation between the bipolar codes of the encoder and the decoder. The result is low-pass filtered, sampled, and compared to a zero threshold to estimate the transmitted symbol.

As the matched filter pairs are identical, a configuration that requires only one pair and one photodetector is feasible. This is accomplished with an appropriate repetitive transmission, by which the symbols are Manchester-coded prior to modulation via the cross-bar switch in Figure 2.2a. The decoder consists of one unipolar correlator pair and one photodetector, followed by a half-symbol delay and a comparator as illustrated in Figure 2.3. The comparator output is decimated by a factor of 2 due to the Manchester coding in the encoder. We note that a particular case of the above general schemes, for which  $u(n) = (1)$ , a unit sequence, can be viewed as the binary PPM or non-coherent FSK modulation system.

## 2.3 Multi-channel Optical Communication

We consider the above modulation and detection principles in the general context of a multi-channel optical communication system model that includes the shot noise

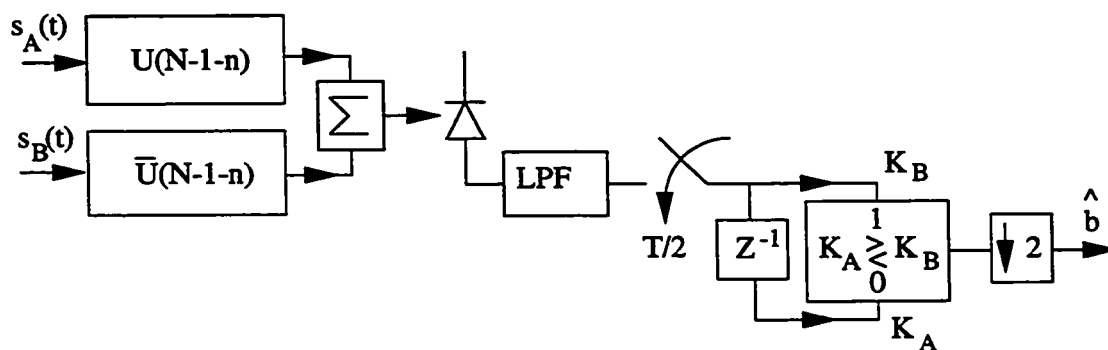


**Figure 2.3** Differential decoder configuration.

The encoder is identical to Figure 2.2a, with the additional requirement that the data symbol  $b$  is Manchester-coded prior to transmission. The comparator output in the decoder must be decimated by a factor of 2 due to this Manchester coding.

nature for the photodetection process. The optimum detection based on the likelihood ratio test for multi-dimensional waveforms in the Gaussian channel has been shown to be a straightforward extension of the single waveform case [38]. In the shot noise or Poisson channel, optimum detection for one-dimensional intensity waveforms have been studied [39], [40]. Here we will show that the scheme described in Sec. 2.2 is in fact the result of optimum detection for a multi-channel optical communication system that distributes the spreading codes over many channels to overcome the restrictions on the signal set.

### 2.3.1 System Model

Figure 2.4 illustrates a multi-channel optical communication system. The intensity of the optical source is modulated by two sets of  $Q$ -dimensional, unipolar, code vectors  $\underline{U}$  and  $\underline{V}$  according to the transmitting symbol  $b$  onto  $Q$  channels, where:

$$\underline{U} = [U_1 \cdots U_Q], \quad (2.5)$$

$$\underline{V} = [V_1 \cdots V_Q]. \quad (2.6)$$

The unipolar codes,  $U_q$  and  $V_q$ ,  $q = 1, 2, \dots, Q$ , are column vectors of length  $N$ :

$$U_q = \text{col}(U_{q,0} \ U_{q,1} \ \cdots \ U_{q,N-1}), \quad (2.7)$$

$$V_q = \text{col}(V_{q,0} \ V_{q,1} \ \cdots \ V_{q,N-1}), \quad (2.8)$$

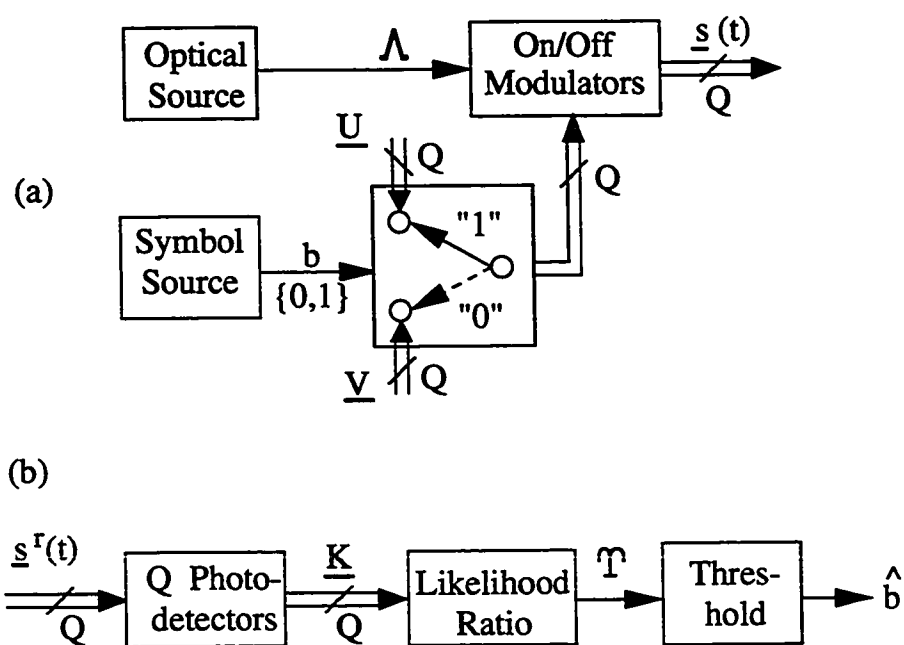


**Figure 2.4** Multi-channel optical communication system.

whose elements,  $U_{q,n}$  and  $V_{q,n}$ ,  $n = 0, 1, \dots, N-1$ , are of unipolar values. The  $Q$ -dimensional intensity waveform vector  $\underline{s}^r(t)$  arriving at the detectors are given by:

$$\underline{s}^r(t) = \text{col}[s_1(t) \cdots s_Q(t)], \quad (2.9)$$

where each waveform  $s_q(t)$  has been encoded by  $U_q$  and  $V_q$  according to:

$$\begin{aligned} s_q(t) = \Lambda \{ & \sum_{i=-\infty}^{\infty} [b_i \sum_{n=0}^{N-1} U_{q,n} \Pi_{T_c}(t - nT_c - iT) + \\ & \bar{b}_i \sum_{n=0}^{N-1} V_{q,n} \Pi_{T_c}(t - nT_c - iT)] \}. \end{aligned} \quad (2.10)$$

The photon arrival rate,  $\Lambda$ , is constant for all chips. The receiver is taken to be synchronized to the transmitter. We further assume that the duration of the received chip waveform  $\Pi_{T_c}(t)$  does not exceed the chip duration  $T_c$ . The photodetectors, one for each channel, are modeled as  $Q$  independent Poisson counting processes whose outputs are independent Poisson random vectors:

$$\underline{K} = [K_1 \cdots K_Q], \quad (2.11)$$

where  $K_q$  is a column vector of length  $N$  whose elements are the counts measured by the  $q^{th}$  detector during each chip interval  $T_c$  in a symbol period  $T = NT_c$ :

$$K_q = \text{col}(K_{q,0} \ K_{q,1} \ \cdots \ K_{q,N-1}). \quad (2.12)$$

The elements  $K_{q,n}$  are independent Poisson random variables with the mean count number given by  $\bar{K}_{q,n}$  according to:

$$\bar{K}_{q,n}|H_1 = U_{q,n} \bar{K}_c + d_q, \quad (2.13)$$

$$\bar{K}_{q,n}|H_0 = V_{q,n} \bar{K}_c + d_q, \quad (2.14)$$

where  $\overline{K}_c = \Lambda T_c$  is the mean count per chip due to the signal intensity and  $d_q$  is the average count due to the dark current of the  $q^{th}$  detector.

### 2.3.2 Likelihood Ratio Decision

The binary detection hypothesis for the observed Poisson count vector  $\underline{K} = \underline{k}$  is:

$$H_1 : \Pr\{\underline{K} = \underline{k}\} = \prod_{q=1}^Q \prod_{n=0}^{N-1} \frac{(U_{q,n}\overline{K}_c + d_q)^{k_{q,n}}}{k_{q,n}!} e^{-(U_{q,n}\overline{K}_c + d_q)} \quad (2.15)$$

$$H_0 : \Pr\{\underline{K} = \underline{k}\} = \prod_{q=1}^Q \prod_{n=0}^{N-1} \frac{(V_{q,n}\overline{K}_c + d_q)^{k_{q,n}}}{k_{q,n}!} e^{-(V_{q,n}\overline{K}_c + d_q)} \quad (2.16)$$

The likelihood ratio test is given as:

$$\Upsilon(\underline{k}) = \prod_{q=1}^Q \prod_{n=0}^{N-1} \left( \frac{U_{q,n}\overline{K}_c + d_q}{V_{q,n}\overline{K}_c + d_q} \right)^{k_{q,n}} e^{-(U_{q,n} - V_{q,n})\overline{K}_c} \underset{0}{\overset{1}{>}} \gamma, \quad (2.17)$$

where  $\gamma$  is the ratio of the *a priori* symbol probabilities. By taking the logarithm of the likelihood ratio, we obtain the sufficient statistic for equal *a priori* symbol probabilities:

$$\Upsilon(\underline{k}) = \sum_{q=1}^Q \sum_{n=0}^{N-1} k_{q,n} [\ln(U_{q,n}\overline{K}_c + d_q) - \ln(V_{q,n}\overline{K}_c + d_q)] - \overline{K}_c \sum_{q=1}^Q \sum_{n=0}^{N-1} (U_{q,n} - V_{q,n}) \underset{0}{\overset{1}{>}} 0. \quad (2.18)$$

The second summation is the difference in the weights, i.e., the numbers of +1's, of the  $Q$ -dimensional unipolar codes  $\underline{U}$  and  $\underline{V}$ . We make the reasonable assumption that the codes have equal – or balanced – weight, so that symbol “1” has the same energy

as symbol “0”, then (2.18) becomes:

$$\Upsilon(\underline{k}) = \sum_{q=1}^Q \sum_{n=0}^{N-1} k_{q,n} [\ln(U_{q,n} \overline{K}_c + d_q) - \ln(V_{q,n} \overline{K}_c + d_q)] \underset{0}{\overset{1}{>}} 0. \quad (2.19)$$

With  $U_{q,n}$  and  $V_{q,n} \in \{0, 1\}$ , it can be shown that (2.19) simplifies to:

$$\Upsilon(\underline{k}) = \sum_{q=1}^Q \ln(\overline{K}_c + d_q) k_q^T (U_q - V_q) \underset{0}{\overset{1}{>}} 0. \quad (2.20)$$

In this study, we assume that the dark current intensities of the photodetectors are identical:  $d_q \triangleq \overline{K}_d$ ,  $q = 1, 2, \dots, Q$ . The sufficient statistic then does not require knowledge of the optical power or the dark current intensities. We obtain the correlation, or matched-filter, detector from (2.20) as:

$$\Upsilon(\underline{k}) = \sum_{q=1}^Q k_q^T (U_q - V_q) \underset{0}{\overset{1}{>}} 0. \quad (2.21)$$

This can be written in terms of the matrix trace operation:

$$\Upsilon(\underline{K}) = \text{tr}[\underline{K}^T (\underline{U} - \underline{V})] \underset{0}{\overset{1}{>}} 0. \quad (2.22)$$

Thus, among the unipolar codes  $\underline{U}$  and  $\underline{V}$  that have equal weight, the probability of error is minimized if and only if:

$$\underline{V} = \overline{\underline{U}}. \quad (2.23)$$

That is, the unipolar codewords for encoding the binary symbols “1” and “0”, respectively, should have no overlapping element of the same value between them. This implies that the unipolar codes are obtained from a  $Q$ -dimensional bipolar code, in a

similar manner described in Sec. 2.2:

$$\underline{X} = \underline{U} - \overline{\underline{U}}, \quad (2.24)$$

or:

$$\underline{U} = \frac{\underline{1} + \underline{X}}{2}. \quad (2.25)$$

$\underline{X} = [X_1 \ \cdots \ X_Q]$  is a  $Q$ -dimensional bipolar code vector, where  $X_q = \text{col}(X_{q,0} \ X_{q,1} \ \cdots \ X_{q,N-1})$ . The elements  $X_{q,n}$  are of bipolar values, and  $\underline{1}$  is a  $Q$ -dimensional unity vector of all 1's.

Note that the code choice given by (2.23) maximizes the signal distance:

$$E[\Upsilon|b_1 = 1] - E[\Upsilon|b_1 = 0] \propto \text{tr}[(\underline{U} - \underline{V})^T(\underline{U} - \underline{V})] \quad (2.26)$$

$$= \text{tr}[\underline{U}^T \underline{U}] + \text{tr}[\overline{\underline{U}}^T \overline{\underline{U}}] = QN. \quad (2.27)$$

Also with the code choice of (2.23), the balanced weight requirement on  $\underline{U}$  and  $\underline{V}$  is equivalent to the condition that:

$$\sum_{q=1}^Q \sum_{n=0}^{N-1} U_{q,n} = QN/2, \quad (2.28)$$

or:

$$\sum_{q=1}^Q \sum_{n=0}^{N-1} X_{q,n} = 0. \quad (2.29)$$

That is, the total numbers of +1's and -1's in  $\underline{X}$  must be the same.

We can specialize the above results to the 2-channel case. If  $Q = 2$ , i.e.,  $\underline{U} = [U_1 \ U_2]$  and  $\underline{K} = [K_1 \ K_2]$ , then the sufficient statistic in (2.22) can be expressed as:

$$\Upsilon = (K_1^T U_1 + K_2^T U_2) - (K_1^T \overline{U}_1 + K_2^T \overline{U}_2). \quad (2.30)$$



We then invoke the infinitely divisible property of the Poisson random variables [41], allowing the four correlations in (2.30) to be performed optically prior to the optical summation and photodetection as shown in Figure 2.2. This means that as far as the photodetectors are concerned, the optical correlations between the received signals and the codewords are presumed to be incoherent, involving only the intensities of the signal in each chip.

The result in (2.30) shows that the modulation and detection principles developed in Sec. 2.2 is a particular case of the multi-channel system with  $U_2 = \overline{U}_1$ . This choice of codes can be obtained by considering the correlation detector described by (2.30) in the presence of interfering users. Due to the statistical nature of the photodetection process, the interfering users generate random noise that cannot be eliminated except in the trivial case that the chips or codes do not overlap. Multi-user detectors attempt to detect the users' symbols simultaneously, but they have high complexity compared to correlation detectors and require knowledge of the users' codes. These detectors also require separate measurement of the energy in each chip, precluding an all-optical implementations.

Without loss of generality, let user 1 be the desired user. For the correlation detector, it can be shown that the expected value of the sufficient statistic in (2.22) is independent of the interfering signals if and only if the  $Q$ -dimensional unipolar codes from the other users are orthogonal to user 1. That is:

$$\text{tr}[\underline{U}_j^T(\underline{U}_1 - \underline{V}_1)] = \text{tr}[\underline{V}_j^T(\underline{U}_1 - \underline{V}_1)] = 0, \quad j \neq 1. \quad (2.31)$$

With the code choice of (2.23), this simply means that:  $\text{tr}[\underline{U}_j^T(\underline{U}_1 - \overline{\underline{U}}_1)] = 0, j \neq 1$ .

By specializing this result for the 2-channel case, with  $\underline{U}_j = [U_{j1} \ U_{j2}]$  we obtain:

$$(U_{j1}^T U_{11} + U_{j2}^T U_{12}) - (U_{j1}^T \overline{U}_{11} + U_{j2}^T \overline{U}_{12}) = 0, j \neq 1. \quad (2.32)$$

By choosing  $U_{j2} = \overline{U}_{j1}$ , (2.32) becomes:

$$(U_{j1}^T U_{11} + \overline{U}_{j1}^T \overline{U}_{11}) - (U_{j1}^T \overline{U}_{11} + \overline{U}_{j1}^T U_{11}) = 0, j \neq 1, \quad (2.33)$$

or:

$$(U_{j1}^T - \overline{U}_{j1}^T)(U_{11} - \overline{U}_{11}) = X_j^T X_1 = 0, j \neq 1. \quad (2.34)$$

This is the bipolar correlation of the bipolar codes defined according to (2.24). Thus, orthogonality between the users according to (2.32) can be satisfied by using orthogonal codes such as Walsh codes.

### 2.3.3 Correlations of Multi-dimensional Codes

As we have seen, the complementary selection of the multi-dimensional unipolar code vectors  $\underline{U}$  and  $\underline{V}$  according to (2.23) defines a bipolar code vector  $\underline{X}$  described by (2.24). From (2.31), we define the correlation of the multi-dimensional unipolar codes as:

$$R_{j,k} \triangleq \text{tr}[\underline{U}_j^T(\underline{U}_k - \overline{\underline{U}}_k)], \quad (2.35)$$

where  $\underline{U}_j$  is obtained from  $\underline{X}_j$  according to (2.25). In terms of the bipolar codes, we have:

$$R_{j,k} = .5\text{tr}[\underline{X}_j^T \underline{X}_k] + .5(\text{tr}[\underline{U}_k^T \underline{U}_k] - \text{tr}[\overline{\underline{U}}_k^T \overline{\underline{U}}_k]), \quad (2.36)$$

which gives:

$$R_{j,k} = .5\text{tr}[\underline{X}_j^T \underline{X}_k]. \quad (2.37)$$

We have used the fact that the second term in (2.36) is zero with the equal energy or balance requirement according to (2.28) or (2.29). For  $Q = 1$ , this requirement precludes the application of many available bipolar codes. The extra dimension with  $Q = 2$  allows the particular bipolar to unipolar mapping that we have developed, i.e.,  $U_{j2} = \overline{U}_{j1}$ , such that the balance requirement is automatically satisfied. This enables the computation of bipolar correlations in a unipolar system, for any bipolar codes. This particular mapping, however, is not unique. Generally, let us denote  $X_{j1}$  and  $X_{j2}$  to be the bipolar codes associated with  $U_{j1}$  and  $U_{j2}$ , respectively. The balance requirement also tells us that the sum of the weight (the number of +1's) of  $X_{j1}$  and  $X_{j2}$  should be equal to the code length  $N$ . The correlation in the unipolar system then becomes:

$$R_{j,k} = .5(X_{j1}^T X_{k1} + X_{j2}^T X_{k2}). \quad (2.38)$$

It is clear that the bipolar code mapping that we have developed is equivalent to taking  $X_{j2} = -X_{j1} \triangleq -X_j$ . This automatically satisfies the balance requirement and (2.38) in fact yields the bipolar correlation:  $R_{j,k} = X_j^T X_k$ . In general, however, any bipolar code pair  $(X_{j1}, X_{j2})$  that is balanced according to (2.29), and has good correlation properties when computed via (2.38), is applicable in the 2-channel unipolar system.

### 2.3.4 Remark

The above formulation thus generalizes the notion of correlation (and orthogonality) of one-dimensional spreading codes into a multi-dimensional setting. This provides the framework that allows the code design to be tailored to the physical communication channel. We believe that a similar multi-channel CDMA approach in the RF, or Gaussian, channel would also allow greater flexibility in the code design there. For example, it could provide the means to implement direct-sequence spread spectrum modulation across channels that have non-contiguous transmission bandwidths, without resorting to the hybrid frequency hopping methods. Thus, combining channel attributes into the code designs can be advantageous in both optical and radio domains.

## 2.4 Implementation

All-optical implementations of the modulation and detection principles that have been developed are practical with either time or spectral encoding methods. All-optical design is extremely important in practice because the symbol rates of the individual users are far less than the bandwidth of the optical fiber. It allows the system electronics to operate at the symbol rates, while making full use of the available optical bandwidth. Figure 2.5 illustrates the two encoding approaches. In the time encoding scheme (Figure 2.5a), the signature code is represented by a series of short optical pulses during a symbol interval  $T$ . Each pulse occurs within a time chip

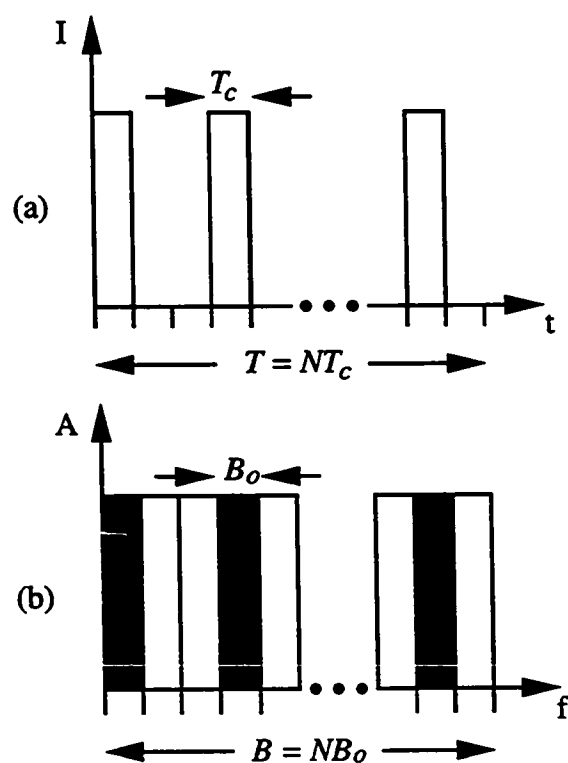


**Figure 2.5** Time and frequency domain encoding.

Frequency domain or spectral encoding (b) has an advantage over time encoding (a) due to the inherent synchronous nature of the spectral codes: cyclic shifts of codes with low autocorrelation can be assigned to subscribers, significantly increasing the number of available codewords.

interval  $T_c$ , where  $T_c = T/N$ . The encoded signal can be modeled as a constant intensity waveform that is modulated by the spreading sequence at the chip rate. In spectral encoding scheme, the signature code is encoded in the amplitude spectrum of the optical signal as shown in Figure 2.5b. The source spectrum is divided into  $N$  frequency bins, or spectral chips of size  $B_o$ . The optical power in each spectral chip is either blocked or transmitted according to the value of the elements in the spreading code. Thus, the amplitude spectrum of the light source is modulated by the codeword at the symbol rate. The spectral dimension of the code is independent of the temporal dimension of the data symbol, resulting in several advantages unique to spectral encoded system that is the focus of our work. For the sake of completion, we will also briefly describe the time encoded system.

#### 2.4.1 Time Domain Encoding

Figure 2.6 shows the schematic diagram of the time domain encoder and decoder. The encoder is realized with a short-pulsed source and fiber tapped delay-line filters. Notice that although the pulses are encoded at the chip rate via the passive filters, the cross-bar switch is modulated at the symbol rate. The total number of taps in the filter pair is  $N$ , which can be prohibitively large for long codes. The transmission channels, A and B, can be distinguished with two fibers (spatial multiplexing), two orthogonal polarizations (polarization multiplexing), two wavelengths (wavelength multiplexing), or simply by time-multiplexing the codewords. Depending on the

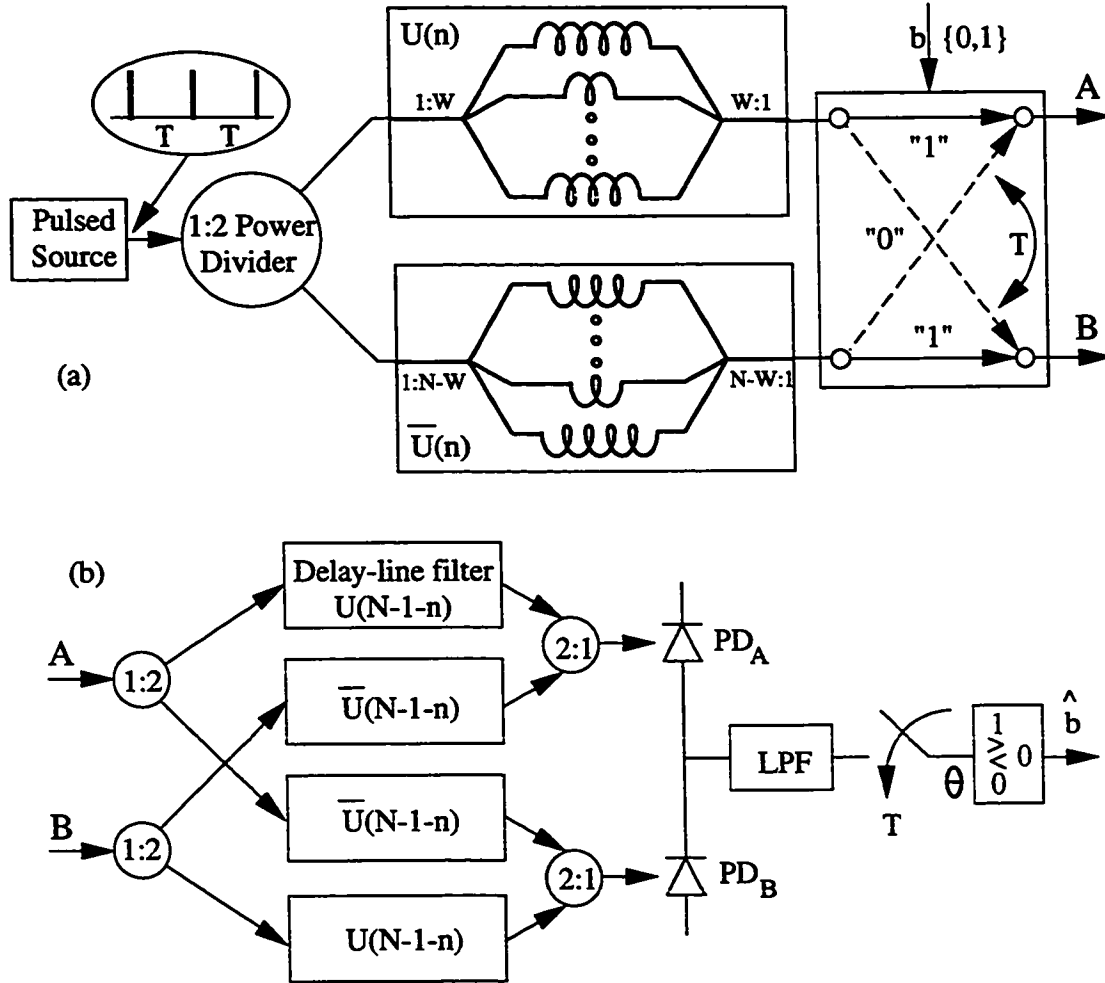


**Figure 2.6** Schematic diagram of time domain encoder and decoder.

Fiber tapped delay-line filters are used to generate the codewords in the encoder (a) and to implement the correlators in the decoder (b). The total number of taps in each filter pair is equal to the length of the code,  $N$  ( $W$  denoting the weight of the code).

transmission method, the received signals are accordingly demultiplexed, and delayed if time-multiplexed, prior to the correlation operations. The unipolar correlators can be realized also with fiber tapped delay-line filters that are matched to the codewords. Since the number of taps in the filters can be prohibitively large, the differential decoder configuration of Figure 2.3 can be employed to reduce the number of matched filters by one half, as well as eliminating one photodetector.

#### 2.4.2 Spectral Amplitude Encoding

An illustration of an all-optical spectral encoder,  $E(\lambda)$ , is shown in Figure 2.7. The spectrum of a broadband source is angularly dispersed by a grating and focused onto a spatial amplitude mask. The spectral bands, or chips, are selectively transmitted through the mask and recombined by another grating. The mask pattern represents the concatenated codewords  $U \oplus \bar{U}$  of length  $2N$ : we have effectively wavelength-multiplexed the two transmission channels required in Figure 2.2. A second encoder,  $\bar{E}(\lambda)$ , encodes  $\bar{U} \oplus U$  with the complement mask pattern encodes. The two output beams are selected for transmission according to the value of the binary symbol. The two modulators can also be implemented via a single, high-speed electro-optic switch operating at the symbol rate. The decoders at the receiver are identical to the encoders, with the output beams coupled to the balanced photodetector pair. The two beams can also be generated with a single two-dimensional mask by stacking the two mask patterns. Alternately, a single one-dimensional reflecting mask can be used



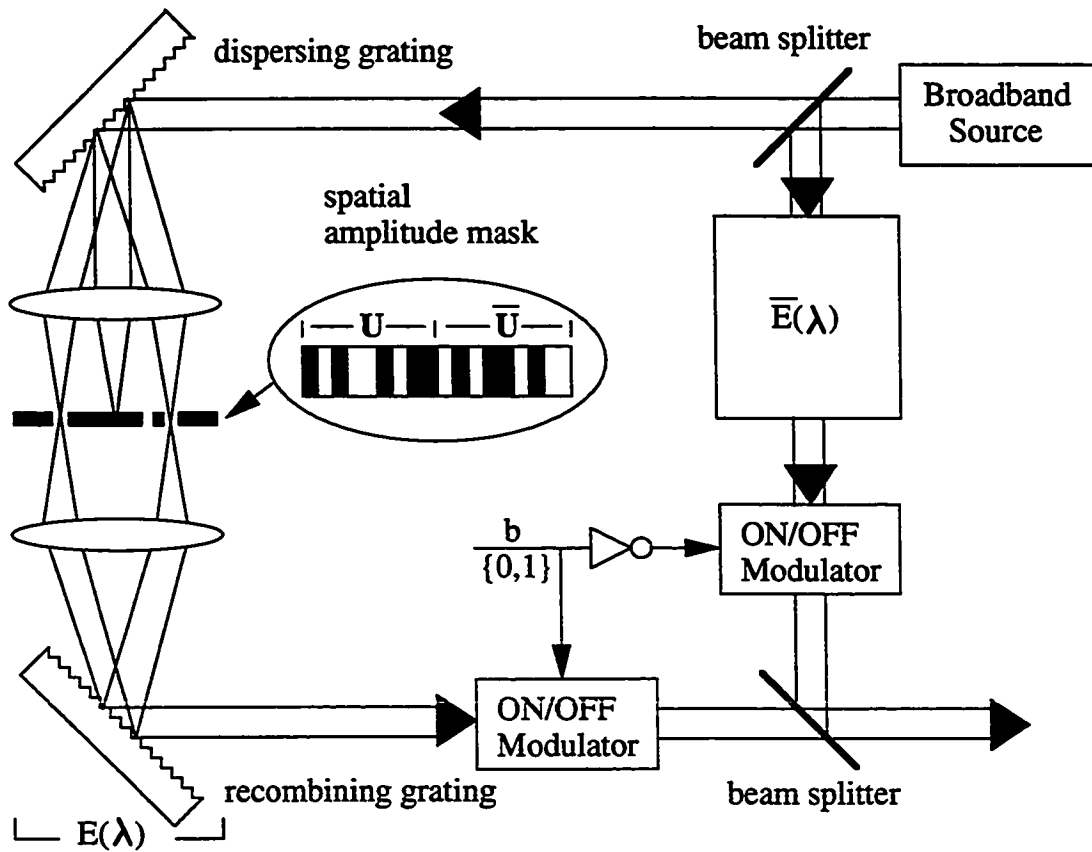


**Figure 2.7** Schematic diagram of an example all-optical spectral encoder.

The optical elements can be simplified with various geometrical configurations. The decoder is similar to the encoder, with the modulators replaced by two photodiodes connected in a balance configuration.

to provide  $U \oplus \bar{U}$  in the transmission and  $\bar{U} \oplus U$  in the reflection. This configuration can be efficient since all of the spectral power is utilized. A practical advantage of spectral encoding is that the flexibility in the optical design can greatly simplify the encoding and decoding functions described in Figure 2.2.

The idea of spectral encoding originated in [42] for coherent-phase optical CDMA. Incoherent spectral amplitude CDMA with multi-user detection was developed in [43]. The correlation detection of this encoding approach was analyzed in [44] and [45] for Hadamard codes and cyclic shifts of an  $m$ -sequence. The spectral encoded system offers several advantages because the spectral nature of the codes is largely decoupled from the temporal nature of the information symbols so that the code length is independent of the symbol rate. This enables the system electronics to operate at the symbol rate while making full use of the source bandwidth. Thus, unlike the time encoding scheme, the users can transmit their data at variable rates without a need to adjust the length of the spreading codes. This is a distinctly desirable attribute in a network that must support many subscribers with different transmission requirements. As spectral codes are always synchronous, Walsh codes can be used to provide orthogonality between users. Moreover, if the code has small offset periodic autocorrelation values, its cyclic shifts can be assigned to different users. For example, the two-valued autocorrelation property of the  $m$ -sequence can result in a simplification of Figure 2.2 and lead to the structure in [44]. In the case of the quasi-orthogonal bipolar Gold and Kasami codes, all  $N$  cyclic shifts of each

of the codewords can be used to give a code book of size  $N(N + 2)$  and  $N\sqrt{N + 1}$ , respectively. This is very desirable in applications that must support a large pool of subscribers with bursty access to the network.

In spectral amplitude encoding, the phase of the spectral components of the source is unimportant. As a result, although both time and spectral encoding methods require broad bandwidth sources, the source for spectral encoded system can be incoherent and therefore is much simpler than the short-pulsed lasers required for time encoded system. In this respect, the superfluorescent fiber source considered in Chapter 3 is ideal for spectral encoding scheme. Additionally, since the modulation of the optical signal is at the symbol rate, spectral encoded system with incoherent source is less affected by the fiber dispersion that causes broadening of optical pulses and limits the transmission distance.

## 2.5 Summary

We have developed new modulation and detection principles that allow all-optical application of the bipolar codes and correlation detection to the direct detection optical CDMA system. By representing the bipolar code as the difference of two unipolar codes, the bipolar correlation can be computed via a “compound” correlator that consists of four unipolar correlations, two summations, and one subtraction. All of these operations, except the subtraction that can be implemented simply with photodetection, can be performed optically without electronic speed restriction. Thus all

the well-designed codes that have been developed for the RF domain can be applicable to the incoherent optical domain. The structure of the encoder and decoder can be interpreted as a generalization of binary PPM or incoherent FSK modulations. The modulation and detection principles have been shown to be the results of the optimum detection based on the likelihood ratio test in a multi-channel optical communication system that includes Poisson statistics for the photodetection process. In this multi-channel model, the spreading codes are distributed over many channels to overcome the restriction on the signal set. The mapping from a bipolar code to the unipolar codes, which can be considered strictly from the bipolar correlation point of view, can be regarded as a particular case in a more general concept of correlation for multi-dimensional codes in a multi-channel framework. Practical, all-optical implementations of the modulation and detection principles, both in time and spectral domains, were discussed. The spectral encoded system has been shown to offer several practical advantages, and is the focus of this work.

## Chapter 3

### Photoelectric Current Distribution of a SFS

A major advantage of spectral amplitude encoding is the simplicity of the optical source. The broad bandwidth requirement, but without the attendant spectral phase characteristics of short-pulse lasers, can be satisfied by using simple light sources such as the light-emitting diodes (LEDs) or the superfluorescent fiber sources. LEDs are less attractive due to their low output power and inefficient coupling into single-mode fiber. SFSs were developed for fiber-optic gyroscopes because they can produce stable and intense broadband light with the low degree of coherence required to detect small rotational rates. When using the SFS for optical communication, a proper analysis of the system performance requires an accurate statistical model for the photodetector current. The excess noise from the thermal nature of the SFS limits the signal-to-noise ratio of the photodetector output. The prevailing Gaussian assumption for the noise statistics has led to the non-physical prediction that the system performance cannot be improved by increasing the optical power. The actual performance, however, depends on the true detection noise statistics. We measured the statistical distribution of the photoelectric current from a PIN photodiode illuminated by a spectrum-sliced, erbium-doped SFS. The histogram of the measurement data is best described by a

negative binomial model for the corresponding photoelectron count, not a Gaussian.

This is consistent with the statistical model of the SFS as a thermal light source.

### 3.1 Theoretical Basis

The output of a SFS is due to spontaneous atomic emission that is amplified in a single (or double) pass through a rare-earth doped, single-mode, optical fiber end-pumped by an external laser [46]. The incoherent light is emitted from the end face of the fiber in a single spatial mode and can have a very high intensity and a broad bandwidth. The light from the erbium-doped SFS has been shown to have the excess noise characteristics associated with thermal light [47]. The theory of photoelectron counting for thermal light has been well developed [48], [49], and gives the counting distribution for polarized light as a negative binomial (NB) probability mass function (pmf):

$$\Pr(K = k) = \frac{\Gamma(k + M)}{\Gamma(k + 1)\Gamma(M)} \left( \frac{E[K]}{M + E[K]} \right)^k \left( \frac{M}{M + E[K]} \right)^M, \quad (3.1)$$

where  $\Gamma(k + 1) = k\Gamma(k)$  is the gamma function,  $E[K]$  is the expected or mean count number and  $M$  is the degrees of freedom. This can also be obtained by treating the spontaneous photon emission in the fiber as the evolution of a birth-death-immigration (BDI) process with zero initial photon population. The general result has been derived by Li and Teich in [50] with coherent input light to a pumped erbium-doped fiber amplifier (EDFA). Without any input light, their result then gives the probability generating function for the corresponding photoelectron counting statis-

tics of the BDI process as:

$$\Phi_K(s) = \left[ 1 - \frac{E[K]}{M}(s-1) \right]^{-M}. \quad (3.2)$$

This is the probability generating function of the NB pmf [51] given by (3.1). The output of the SFS can therefore be modeled as thermal light.

In (3.1),  $E[K] = \eta PT/h\nu$ , where  $P$  is the average light intensity during the measurement interval  $T$ ,  $h\nu$  is the photon energy, and  $\eta$  is the quantum efficiency of the detector. The mode number of the incident light,  $M$ , which represents the number of coherence cells of the input light that affects the measurement of the photoelectron counts, describes the degrees of freedom of the NB pmf. We take the detection area of the photodetector to be less than the coherence area of the incident lightwave, so that the light is spatially coherent across the detection surface. The mode number of polarized light is then equal to the ratio of the measurement interval to the coherence interval,  $\tau_c$ , of the source:  $M = T/\tau_c$ , for  $T/\tau_c \gg 1$ . In terms of the optical and detection bandwidths:  $M = B_o/2B_e$ , where  $B_o$  and  $B_e$  are given by the following:

$$\tau_c = \frac{1}{B_o} \triangleq \int_0^\infty \left[ \frac{P(\nu)}{\int_0^\infty P(\nu) d\nu} \right]^2 d\nu, \quad (3.3)$$

$$B_e = \frac{1}{2T} \triangleq \int_0^\infty \left| \frac{H(f)}{H(0)} \right|^2 df. \quad (3.4)$$

$P(\nu)$  is the power spectral density of the input lightwave and  $H(f)$  is the frequency response of the detector. If  $T/\tau_c \ll 1$  then the intensity fluctuations within a measurement interval are correlated, thus  $M = 1$ , i.e., the measurement is always affected

by one coherence cell of the incident light (the relationship of  $M$  versus  $T/\tau_c$  has been found to weakly depend on the power spectrum only for  $.1 < T/\tau_c < 10$  [49]). Equation (3.1) then reduces to the Bose-Einstein distribution [52]. In spectrum-sliced WDMA applications,  $M$  is greater than unity because the optical bandwidth of each channel will be larger than the symbol rate. The SNR of the counting signal is given as:

$$SNR \triangleq \frac{E^2[K]}{\sigma_K^2} = \frac{E[K]}{1 + E[K]/M}, \quad (3.5)$$

where  $\sigma_K^2$  is the count variance, and is equal to  $M$  for  $E[K] \gg M$ . For partially polarized light:

$$SNR = \frac{E[K]}{1 + (1 + \mathcal{P}^2)E[K]/2M}, \quad (3.6)$$

where  $\mathcal{P}$  is the degree of polarization of the source [48]. The SNR therefore is equal to  $2M/(1 + \mathcal{P}^2) = B_o/(1 + \mathcal{P}^2)B_e$  for  $E[K] \gg 2M/(1 + \mathcal{P}^2)$ . This limiting SNR characteristic for high power level has been verified for the photoelectric current using polarized and unpolarized light from the erbium-doped SFS [47], [53], and is a fundamental limitation on the noise performance of fiber optic gyroscopes using the SFS. For unpolarized thermal light, the limiting SNR from (3.6) is  $2M = B_o/B_e$ ; the counting statistics are also given by the NB pmf, but with  $2M$  degrees of freedom [49].



### 3.2 Experimental Description

The ratio  $E[K]/M$ , known in the literature as the count degeneracy parameter, describes the excess noise due to the stochastic nature of the polarized light relative to the shot noise of the photodetection process. Since  $E[K]$  is proportional to the average integrated intensity  $PT$ , the count degeneracy parameter is equal to  $\eta P\tau_c/h\nu$  and therefore is proportional to the spectral intensity for sources with a uniform power spectrum according to (3.3). Previous experimental studies have employed either natural thermal light from a mercury, tungsten, or discharge lamp [54], [55], or pseudo-thermal light obtained by scattering coherent laser light from moving ground glass or from a large volume of targets in Brownian motion [49], [56]. As is well-known, if the count degeneracy parameter is very small, the count distribution tends to a Poisson pmf. This is the case with a natural thermal light source due to its weak spectral intensity. Pseudo-thermal light, on the other hand, can result in a large count degeneracy parameter, but it has a much narrower linewidth. The SFS, with its intense and broad bandwidth output in a single spatial mode, provides a unique device for experimental investigations of photoelectron counting statistics of thermal light without the afore-mentioned constraints.

As the excess noise exceeds the shot noise when the count degeneracy parameter is greater than unity, the stochastic fluctuation can be observed if the average “coherence energy” of the source, defined here as  $P\tau_c$ , that can be measured by the detector is much larger than the photon energy. Alternately, if we interpret the quantity

$P_c \triangleq h\nu/\tau_c$  as the “coherence power” of the photon, then the excess noise dominates if the average light intensity that can be detected is much larger than  $P_c$  \*. These quantities are characteristics of the source and are independent of the detector and the measurement interval. We define the threshold power of a photodetector as the input light level at which excess noise begins to dominate the detector output. For a polarized source with a bandwidth of 0.1 nm at 1550 nm wavelength, the threshold power corresponds to less than 2 nW and is equal to  $P_c$  for a detector with unity quantum efficiency. If the lightwave is partially polarized, the threshold power is larger by a factor of  $2/(1 + \mathcal{P}^2)$ . The threshold power can be larger than  $P_c$  in a system that has other noise components and a quantum efficiency less than unity, as the experiment will demonstrate.

According to the Central Limit Theorem, as  $M$  grows arbitrarily large (i.e. the number of modes in the incident lightwave goes to infinity), the NB distribution approaches a Gaussian distribution for a fixed value of the count degeneracy parameter [51]. It follows from the previous discussion that light sources with a uniform power spectrum satisfy this condition. Therefore while the NB distribution given by (3.1) is asymmetric, for a large source bandwidth relative to the detection bandwidth it is practically indistinguishable, near the central region, from a Gaussian distribution that has the same mean and variance. The experimental parameters therefore

---

\*If the coherence area of the incident lightwave is smaller than the detection area, then the corresponding quantities should be the coherence energy and power within a coherence area.

must be judiciously chosen so that (3.1) can be verified in the central region of the distribution.

The experimental setup is illustrated in Figure 3.1. An erbium-doped fiber (Corning-7834502) 8 m long was end-pumped by a diode laser (SDL-6312) at 980 nm wavelength through a dichroic mirror. The fiber ends were polished at  $15^\circ$  to prevent back reflections and possible laser oscillation. The backward amplified spontaneous emission (ASE) output through the dichroic mirror at 1550 nm is unpolarized and was coupled into a spectrometer (SPEX-HR460) to select a narrow linewidth at 1533 nm. The spectrum-sliced ASE at the spectrometer output was focused onto a low-noise InGaAs PIN photodiode (New-Focus 1611AC detector) that has a typical responsivity of 0.8 A/W. The detector incorporates transimpedance gain so that the output voltage is proportional to the photoelectric current of the PIN photodiode. The mean level of the voltage signal and its fluctuation were separately monitored with the DC and AC coupled outputs (typical gains of 1000 V/A and 250 V/A, respectively) of the detector. The output voltage fluctuation was further amplified by a low-noise, wide-band amplifier with a 31 dB gain, and then sampled by a high-speed sampler (SRS-SR255) with a 200 ps gate width. The noise bandwidth of the detection system was limited by the low-noise detector to about 1100 MHz, with a low frequency roll-off at about 10 KHz.

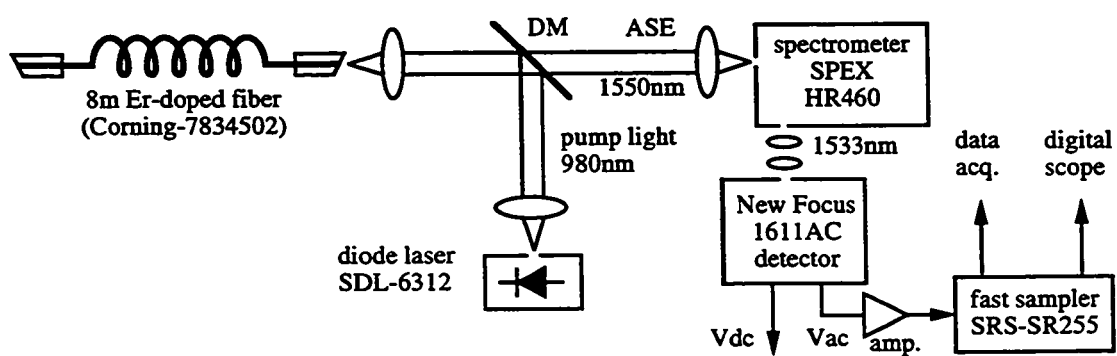


**Figure 3.1** Experimental configuration to measure the photoelectric current distribution.

### 3.3 Measurement Results

Measurement of the true statistics of the SFS requires an experimental compromise between conflicting requirements. Reliable measurement of the distribution of the photodetector response requires that excess noise be the principle contributor to the photoelectric current fluctuation, so that it dominates the background noise. This calls for high input power, hence a large sliced bandwidth. On the other hand, the sliced bandwidth must be kept sufficiently small so that the NB and the Gaussian models can be discriminated from each other near the central region of the distribution, as previously discussed. Given that the measured background noise is also Gaussian distributed, the feasible range of the experimental parameters for measurement of the true statistics is rather limited. From these considerations, the wavelength for the noise measurement should be chosen to be at the peak of the source spectrum, where the count degeneracy parameter is large. We do not expect a similar measurement, if feasible, at other wavelengths within the bandwidth of the erbium-doped SFS, or EDFA, to yield a different statistical description of the noise. As discussed in Sec. 3.4, there is no fundamental reason to suggest that the physics of the emission process across the bandwidth, the thermal nature of the light, should depend on the wavelength.

### 3.3.1 Histograms

The background noise of the measurement system is dominated by the detector noise and was determined by blocking the input light to the spectrometer. Figure 3.2 shows the measured distribution of the background noise and the calculated zero-mean Gaussian distribution whose variance is specified by the noise power. The large probability at the mean results from a quantization error of the fast sampler. The quantizer employs a sign bit plus eight other bits to cover a full scale. This makes the quantization resolution around the zero level to be twice as coarse as other levels. Thus, there are more output samples around zero than other signal levels. As a result, for a histogram of 32 bins, the ratio of the number of quantization steps in the center bin to the adjacent bins is approximately  $18/16 = 1.125$ . This is also approximately the relative size of the discrepancy that has been observed around the mean. If we ignore this point, the background noise is described by a Gaussian distribution very well.

In our experiment, the spectrometer was tuned to the spectral peak of the input ASE spectrum, at about 1533 nm wavelength. Initially, the output slit of the spectrometer was open wide enough so that excess noise dominated the voltage signal fluctuation. The linewidth of the spectrum-sliced ASE was sufficiently large so that the resulting large mode number caused the voltage fluctuation to appear symmetric around the mean level, as monitored on a digital oscilloscope. The output slit of the spectrometer was then gradually narrowed, effectively decreasing the mode number

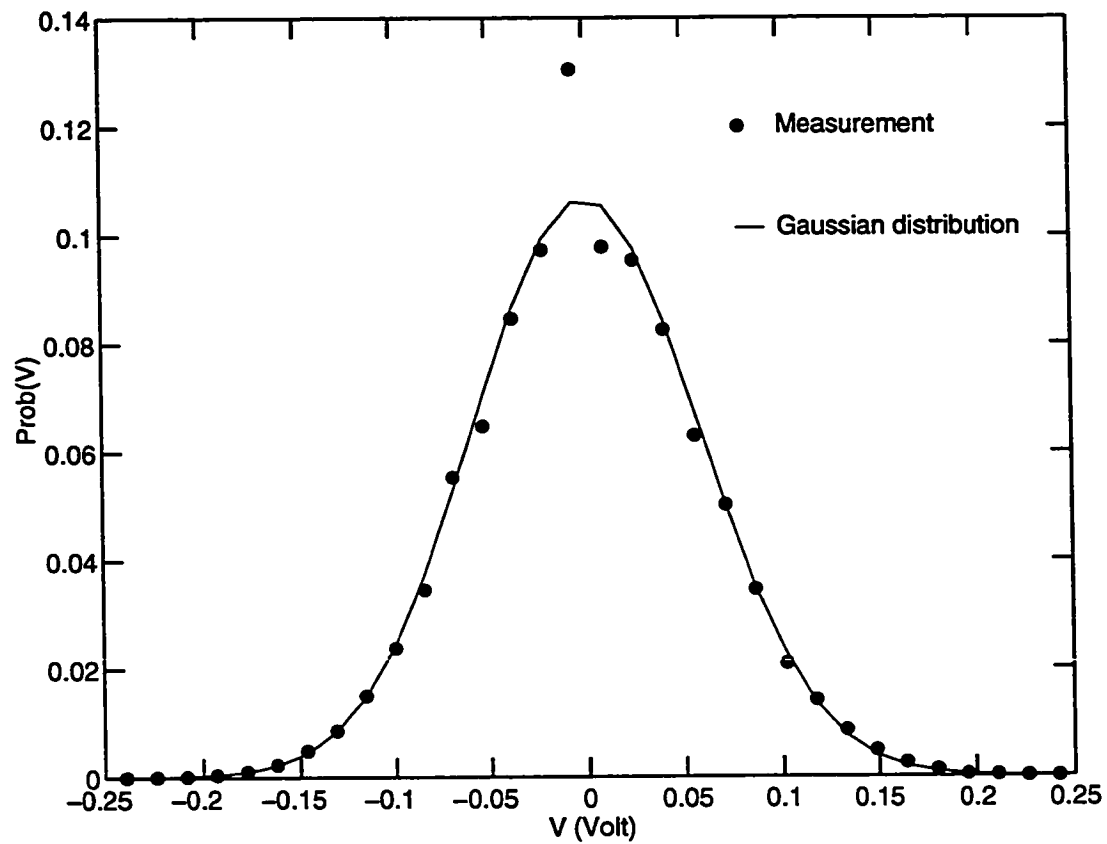


**Figure 3.2** Background noise distribution of the measurement system.

The voltage noise power is  $-11.7$  dBm in a 1100 MHz bandwidth. The noise distribution is well modeled by a Gaussian.

and reducing the excess noise level, until the fluctuation became asymmetric from the mean. The background noise level was sufficiently low so that this condition could be achieved while keeping the rms fluctuation power, as computed by the scope, at least 10 dB or more above the background noise power.

Figure 3.3 shows a plot of the output voltage signal fluctuation when the spectrometer was adjusted to obtain an optical linewidth of about 0.29 nm at the output slit. The power level of the unpolarized ASE into the photodetector was about  $45 \mu\text{W}$ , giving an rms voltage fluctuation power of 12.4 dB above the background noise of the measurement system. The threshold power of the system was approximately  $2 \mu\text{W}$  in comparison to the calculated  $P_c$  value of 5 nW at the measurement wavelength (the excess noise measurement can provide a good estimate of the effective input noise current density of the detector). Thus at the above input power and bandwidth, the light intensity exceeds  $P_c$  by almost 40 dB. The plot demonstrates that the fluctuation around the mean is asymmetric as predicted by (3.1), suggesting immediately that the noise statistics cannot possibly be a Gaussian.

The distribution of the voltage signal fluctuation according to the histogram of the measurement data is plotted in Figure 3.4. In order to compute the expected distribution, we assume that the output voltage is additive, that is, the sum of the background noise and the voltage fluctuation due to the incident light on the detector. These two components are assumed to be statistically independent random processes described by the Gaussian (Figure 3.2) and NB (with  $2M$  degrees of freedom for



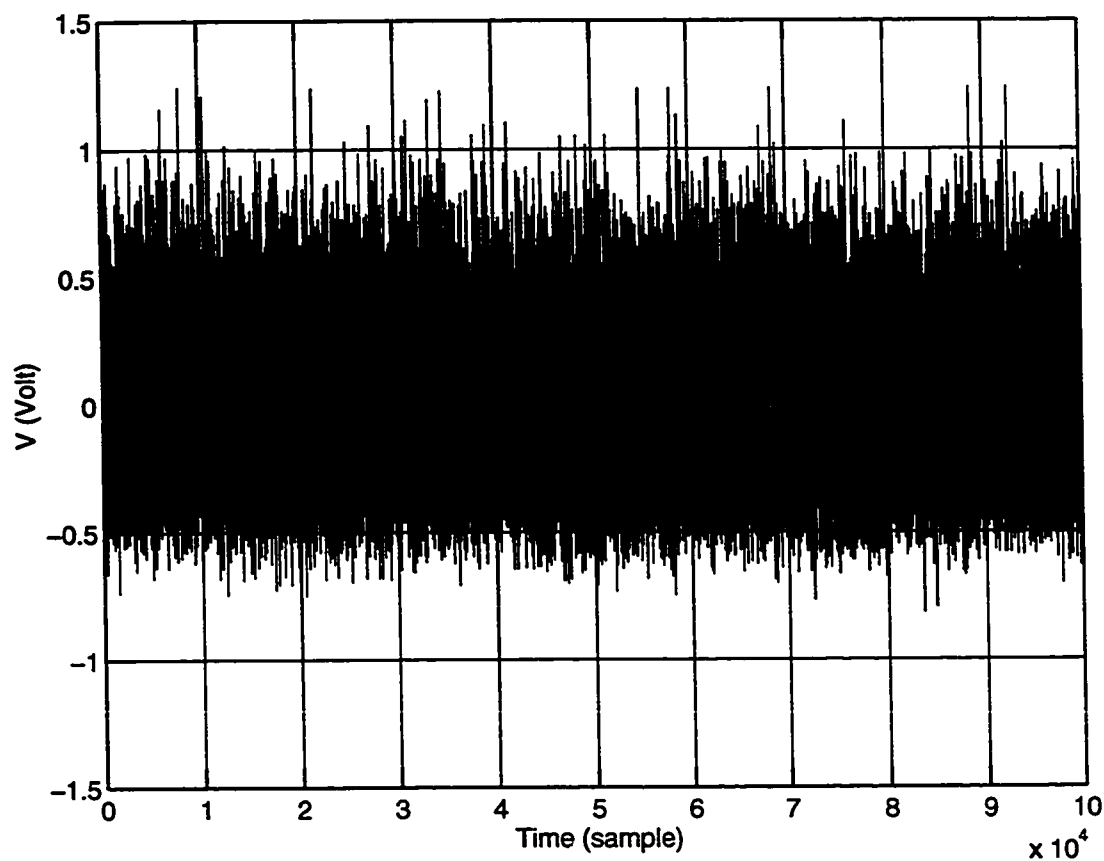


**Figure 3.3** Sampled signal fluctuation of the detector output voltage.

The input light is an unpolarized, spectrum-sliced, erbium-doped SFS at  $-13.5$  dBm. The rms power of the voltage fluctuation is  $+0.7$  dBm. The incident light has a linewidth of  $0.29$  nm at  $1533$  nm wavelength. The noise voltage is asymmetric, indicating that the underlying distribution cannot possibly be a Gaussian.

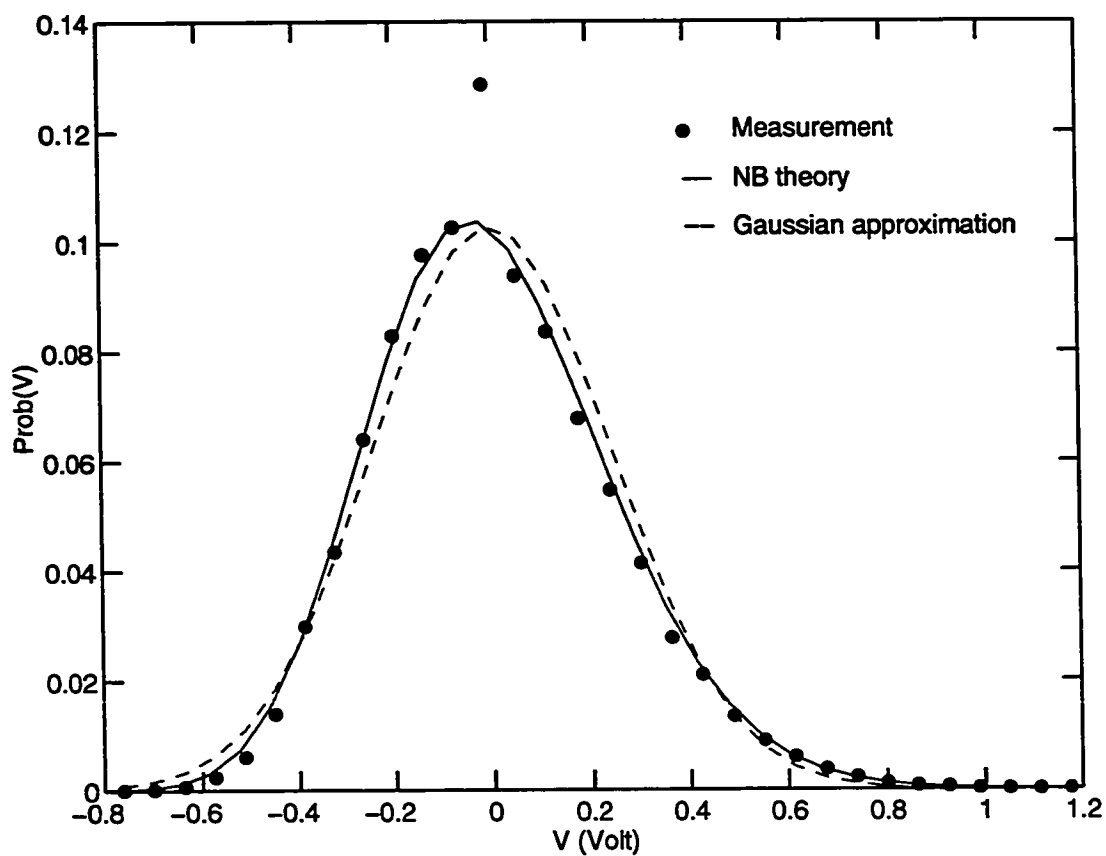


**Figure 3.4** Distribution of the voltage signal fluctuation.

The histogram of the voltage signal fluctuations measured in Figure 3.3 is assymmetric, indicating that the statistics cannot possibly be a Gaussian. The theoretical NB model with the calculated mode number of 31 and the Gaussian approximation are also shown.

unpolarized light) models, respectively. We calculated the theoretical NB distribution by converting the voltage bins of the histogram to photoelectron counts, so that the count probabilities could be computed from (3.1) for the corresponding bins. The DC voltage level provided the mean count for the NB model. The background noise power was subtracted from the rms fluctuation power, so that the mode number  $2M$ , or  $B_o/B_e$ , could be determined from (3.6) with  $\mathcal{P} = 0$ . The calculated NB distribution was then convolved with the Gaussian distribution of the background noise in Figure 3.2 to obtain the expected distribution with the calculated mode number of 31

The expected distribution with the mean removed is plotted in Figure 3.4 as the curve labeled “NB theory”. The curve shows good agreement with the measured distribution except for the systematic discrepancy at the mean as previously observed. A Gaussian model with the same variance as the measurement data is also shown. Notice that it cannot account for the asymmetry in the measured distribution. Using the calculated mode number of 31 and the detection noise bandwidth of 1100 MHz, we obtain a spectrum-sliced bandwidth of 34.1 GHz which is comparable to the linewidth of 0.29 nm, or 37 GHz at 1533 nm wavelength, as set by the spectrometer output slit. This suggests that the power spectrum of the fiber source at the measurement wavelength is uniform over the sliced linewidth, and that the spectrometer provides an essentially uniform spectral intensity across the selected width of the output slit.

### 3.3.2 Moment Analysis

The performance of low error rate systems is dominated by the low probability tails of the noise distribution. These details are difficult to see in the standard linear plots of the distributions in Figure 3.4, and in any case, visual comparison is not very useful. The measured and calculated distributions can be compared quantitatively using the normalized moment of order  $m$ , defined as

$$F(m) \triangleq \frac{E[V^m]}{E[V]^m} - 1, \quad (3.7)$$

for the detected signal. The high order moments are sensitive to the low-probability tail region, and a comparison of the normalized moments provides an indication of how well the statistical models agree with the experimental data. In (3.7),  $E[V^m]$  is the  $m^{\text{th}}$  moment of the voltage signal and  $E[V]$  is the mean signal level. With the assumed additive noise processes,  $F(m)$  was computed from the moment generating function that can be obtained as the product of the moment generating function from the NB model for the signal fluctuation due to the fiber source, and that from the Gaussian model for the background noise of the measurement system. The expected normalized moments are plotted as the points labeled “NB model” in Figure 3.5. Also shown are the normalized moments of the Gaussian approximation. The points labeled “Measurement” are the normalized moments of the measured distribution and were calculated from the histogram data. The plot demonstrates that the signal fluctuation is best described by the NB model; the Gaussian approximation starts

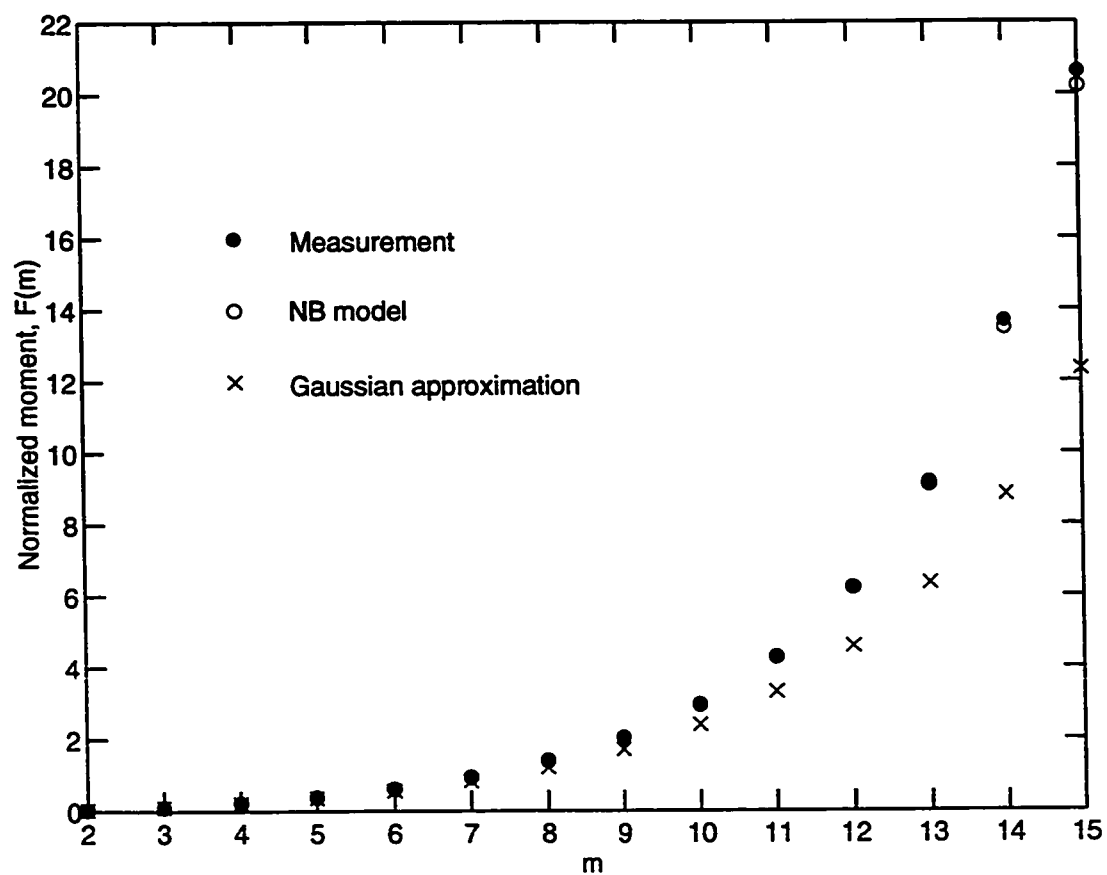


**Figure 3.5** Normalized moments.

The Gaussian approximation to the measurements is poor in the tail of the distribution, compared to the NB model.

to deviate from the measurement results at about the 8th moment. This plot also suggests that the Gaussian is a reasonably good distributional model for the central region, but that it fails to model the tail of the distribution. This behavior is an example of the well-known caveat of the Central Limit Theorem [57]. The results of the moment analysis imply that even with a large mode number of 31, the Gaussian approximation will yield a poor estimate of the tail probability. Since the tail of the signal distribution determines the BER performance of a digital communication system, we should expect the BER of the fiber source system to differ from that predicted by the Gaussian model.

### 3.4 Remarks

As a lightwave amplifier, the noise figure of the EDFA has been shown to be a function of the wavelength within the EDFA bandwidth due to the non-uniform fluorescent and gain spectrum profiles [58]. The statistical properties of the photocurrent noise, however, are a direct result of the physics of the light source. Since photons from the SFS are amplified spontaneous emission that has the characteristics of a thermal source regardless of the photon frequency, we expect the NB statistical description for the SFS to be wavelength independent.

### 3.5 Summary

We have described the measurement of the photoelectric current distribution of a PIN photodiode illuminated by a spectrum-sliced, erbium-doped SFS. The characteristic coherence power and energy were introduced to quantify the excess noise of the detector due to stochastic fluctuations in the incident lightwave. The experimental results confirm that the distribution is non-Gaussian and follows a negative binomial model that is predicted by the theory of photoelectron counting for thermal light. As a result, we should expect performance of the fiber source system to differ from that predicted by the Gaussian model.

## Chapter 4

### Performance of Spectrum-sliced WDMA

The superfluorescent fiber sources, particularly the erbium-doped fiber amplifier source, have been demonstrated as feasible light sources for spectrum-sliced WDMA optical communication systems [53], [59], [60], [61]. In Chapter 2, we have considered a spectral amplitude CDMA scheme that employs the SFS [62]. The thermal nature of the SFS causes the signal-to-noise ratio of the photodetector output to reach a limiting value due to the excess noise. As a result, the usual approach to the performance analysis that assumes a Gaussian distribution for the detected signal [53], [59], [60], [61], [63], [64] predicts a BER floor, hence a limited number of channels, that cannot be improved by increasing the optical power. This contradicts the intuitive notion that the system performance should improve as more power is received. To our knowledge, there is no experimental evidence, nor any theoretical derivation based on the physics of thermal light, to support using the Gaussian distribution to describe the statistics of the detector photocurrent noise. The Gaussian model is a mathematical convenience because the performance measure based on this model can be completely specified by the SNR. Its use is usually justified by invoking the Central Limit Theorem. A well-known caveat of this theorem for distributional



approximation is that it is very difficult to accurately estimate the tail of a distribution [57]. Using the Central Limit Theorem for BER analysis can be misleading because the performance of low error rate systems is dominated by the low probability tail of the noise distribution [65].

The actual performance depends on the true detector noise statistics that have been shown to be best described by a NB pmf, as experimentally demonstrated in Chapter 3. In this Chapter, we analyze the performance of a spectrum-sliced WDMA system using the NB statistics. Improved performance is obtained that is consistent with the results when the erbium-doped fiber is used as a lightwave amplifier [50]. In the EDFA, spontaneous atomic emission contributes unwanted noise to the amplified output light. Li and Teich have shown in [50] that the Gaussian assumption for the EDFA leads to underestimation of the BER performance. However in that application, the SNR did not reach a limiting value and the error in using the Gaussian model was relatively modest [66].

## 4.1 Spectrum-sliced WDMA System Model

Figure 4.1 shows a block diagram of the spectrum-sliced WDMA system. The output of the EDFA source is spectrum-sliced by a narrow-band filter. The narrow-band ASE output is then on-off modulated by the binary symbol and coupled onto a WDM fiber channel. At the receiver, the desired user is detected by tuning a narrow-band filter to the appropriate sliced channel, or spectral chip. Such a system has certain advantages

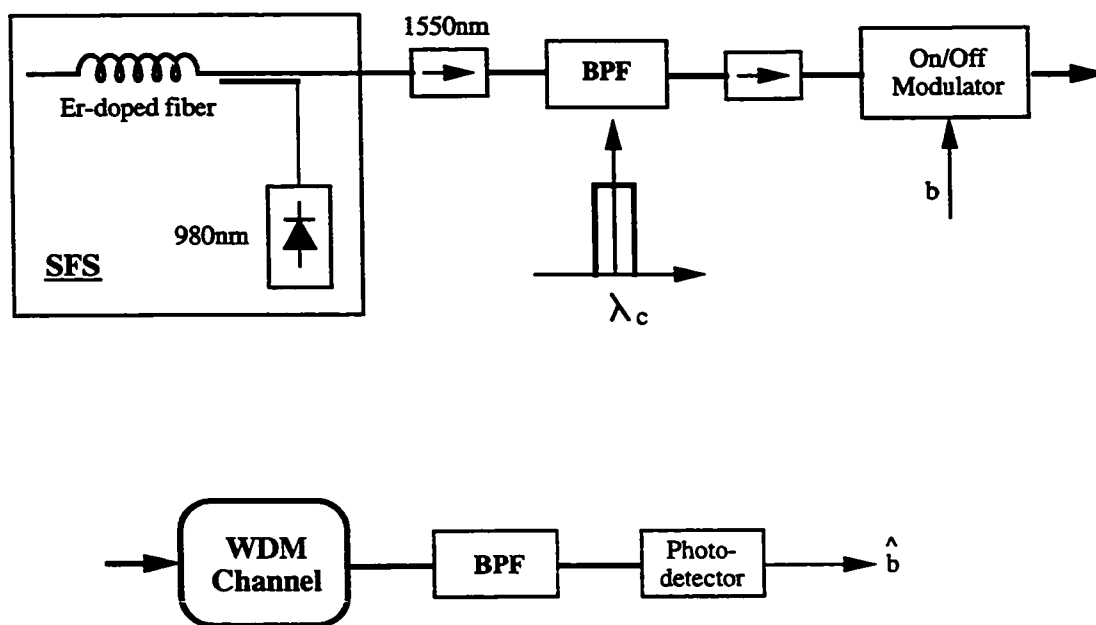


Figure 4.1 Block diagram of a spectrum-sliced WDMA system.

in the simplicity of the source and in the wavelength stability provided by the filter. Since the transmission capacity of the system is affected by the optical bandwidth and the symbol rate of each channel, it is desirable that their ratio, hence the mode number (or the limiting SNR) of spectrum-sliced fiber sources, be small. From the Central Limit Theorem, small mode numbers of the incident lightwave cause the Gaussian approximation to the true statistics to be highly questionable, especially for estimating the achievable BER performance. This situation is particularly true when the input light intensity exceeds the threshold power level of the receiver, so that excess noise dominates the decision statistics.

Now consider the light from a spectral chip that is on-off (ASK) modulated by a binary data stream at the transmitter, resulting in an intensity modulation waveform arriving at the photodetector. We assume an ideal photoelectron counting receiver by neglecting the dark current response of the photodiode and the thermal noise of the electronics. The receiver is taken to be synchronized to the transmitter. We further assume that the duration of the received modulation waveform for each transmitted symbol does not exceed the symbol period  $T$ , so that there is no intersymbol interference. The intensity of the arriving optical signal is given as  $\sum_{i=-\infty}^{\infty} b_i \Lambda(t - iT)$ , where  $b_i$  is the  $i^{th}$  binary, +1/0, symbol;  $\Lambda(t)$  is the intensity modulation waveform that is zero outside  $[0, T)$ .

## 4.2 BER Analysis

The probability of observing  $K$  photoelectrons during  $T$  is given by the Poisson pmf with mean  $\alpha W$ , where  $\alpha = \eta/h\nu$ , and  $W$  is the integrated intensity corresponding to the binary hypotheses:

$$H_0 : W = 0, \quad (4.1)$$

$$H_1 : W = \int_0^T \Lambda(\xi) d\xi. \quad (4.2)$$

Under  $H_0$ , the photoelectron count output is identically zero by the ideal receiver assumption. With equal *a priori* probabilities, the optimum decision rule compares the photoelectron count to a zero threshold to estimate the transmitted symbol. The assumption of no background noise and a zero threshold results in a consistent system that lends itself to a rigorous analysis and quantitative performance calculations. Clearly, if other noise sources were present the optimum threshold would be non-zero. Exact calculations for such a case are considerably more complex and quantitative estimates are discussed in Sec. 4.4. The results, however, would have the same character as the following analysis: BER performance is not determined solely by the SNR, independent of the received power.

The BER for the ideal receiver with the above optimum decision rule is given as  $\Pr(K = 0|H_1)/2$ . To compute this probability, we consider the conditional Poisson pmf of the count output under  $H_1$ , conditioned on  $W$ :

$$\Pr(K = k|H_1, W = w) = \frac{(\alpha w)^k}{k!} e^{-\alpha w}. \quad (4.3)$$

The unconditional probability under  $H_1$ ,

$$\Pr(K = k|H_1) = \int_0^\infty \frac{(\alpha w)^k}{k!} e^{-\alpha w} p_W(w) dw, \quad (4.4)$$

is known as Mandel's formula, or the Poisson transform of  $W$ , where the probability density function  $p_W(w)$  describes the stochastic nature of the source [49]. Using this result, we obtain:

$$BER = \frac{1}{2} \int_0^\infty e^{-\alpha w} p_W(w) dw. \quad (4.5)$$

The BER is thus simply the Laplace transform of the integrated intensity, or its moment generating function. Now for polarized thermal light, the integrated intensity  $W$  is approximately gamma distributed [48], [49] with parameters  $M$  and  $M/E[W]$ . Using this model for the SFS in (4.4) results in a NB pmf for  $\Pr(K = k|H_1)$  as given by (3.1). The BER can then be obtained as the moment generating function of the gamma distribution via (4.5), or by evaluating (3.1) at  $k = 0$ , to obtain:

$$BER = \frac{1}{2} \left( \frac{M}{M + E[K]} \right)^M = \frac{1}{2} \left( \frac{SNR}{E[K]} \right)^M. \quad (4.6)$$

This can also be expressed in terms of the average received power  $P = E[W]/T$  under  $H_1$ , and the coherence power  $P_c$  as previously defined:

$$BER = \frac{1}{2} \left( \frac{1}{1 + \eta P/P_c} \right)^M. \quad (4.7)$$

The count degeneracy parameter,  $\eta P/P_c$ , thus plays an important role in determining the BER of the system. If it is much smaller than unity, i.e. for a count

average much less than one count per mode, then the BER can be shown to approach the quantum-limited performance and is approximately equal to  $e^{-E[K]}/2$ . It is interesting to note, however, that given an optical bandwidth and a symbol rate, a better performance is obtained if the count degeneracy parameter is large, i.e., when the detected signals are dominated by excess noise. The BER can be improved by increasing the optical power of the incident lightwave, thereby making the count degeneracy parameter larger.

Since the limiting SNR is equal to the mode number, which is proportional to the ratio of the optical and the detection bandwidths, the maximum SNR is inversely proportional to the number of channels in a spectrum-sliced WDMA system. The BER expressions given by (4.6) and (4.7) demonstrate that the performance is not determined solely by the SNR, which becomes constant as the received power increases. In real systems, where other noise components may exist, this qualitative behavior is expected to hold for received power levels sufficient to exceed the threshold power of the receiver.

For partially polarized thermal light, the above analysis can also be applied with the corresponding counting statistics [48] to obtain:

$$BER = \frac{1}{2} \left[ 1 + \frac{\eta P}{P_c} + \left( \frac{\eta P}{2P_c} \right)^2 (1 - \mathcal{P}^2) \right]^{-M}, \quad (4.8)$$

which gives for unpolarized light:

$$BER = \frac{1}{2} \left( \frac{1}{1 + \eta P / 2P_c} \right)^{2M}. \quad (4.9)$$

This shows that the unpolarized fiber source has the advantage of requiring only half of the optical bandwidth, therefore the channel capacity can be doubled, compared to a polarized source, while still achieving the same symbol and bit-error rates at the same power level.

We observe that the BER values given by (4.6) through (4.9) decrease monotonically with  $\tau_c$ . Consequently, given a constant average power and a fixed 3 dB linewidth, a Lorentzian spectral shape can have a lower BER at a higher symbol rate compared to a Gaussian shape. The ideal rectangular spectral shape has the worst performance. The performance gain from the spectral shape must be considered against the channel crosstalk in WDMA since, not surprisingly, the tail of a Lorentzian shape has the slowest spectral decay. If there is no constraint on the 3 dB linewidth, we obtain a rather interesting theoretical result that the quantum limit of  $e^{-E[K]}/2$  is achieved (by taking the limit as  $\tau_c$  goes to zero in (4.6) through (4.9)) with a spectral shape that has an infinite linewidth with zero spectral height. Such a SFS can be termed “ideal” by this asymptotic behavior. In contrast, we recall that the quantum limit is also achieved by an ideal, coherent laser of infinite spectral height and zero linewidth. Physically, the asymptotic behavior of the SFS is expected because a detector of a finite bandwidth cannot follow the intensity fluctuations of an ideal SFS. The output noise statistics are thus affected only by the average input light intensity and are therefore purely Poisson, exactly as the case with an ideal laser.

According to (4.6) through (4.9), it is possible then, in a spectrum-sliced WDMA system, to increase the number of channels while maintaining a desired BER for a given symbol rate by increasing the received power per channel. This has important implications for spectral-amplitude optical CDMA systems that use a large number of spectral chips to support many subscribers. Invoking the Gaussian assumption when analyzing such a system [53], [59], [60], [61], [63] would lead to incorrect conclusions: the limiting SNR characteristic of the fiber source would result in the prediction of a BER floor and, consequently, a limited number of channels.

### 4.3 Numerical Examples

Figure 4.2 illustrates an example calculation of the required received power per channel versus the number of spectrum-sliced WDMA channels, assuming a polarized SFS linewidth of 30 nm and a detector quantum efficiency of 80% at 1550 nm wavelength. The plots are shown for the BER value of  $10^{-9}$ , a 1 Gbps symbol rate, and a detection bandwidth of 500 MHz. We assume that the source linewidth is spectrally sliced into a number of channels having identical, rectangular line shapes with no guard bands in between. The plot shows that the BER of the fiber source system can be maintained by steadily increasing the received power as the linewidth of the channels is reduced from 30 nm to .03 nm. The Gaussian assumption with the BER given by  $Q(\sqrt{SNR})$ , where  $Q(.)$  is the Marcum Q-function [57] and the SNR is calculated according to (3.5), overestimates the required received power and incorrectly predicts a limiting



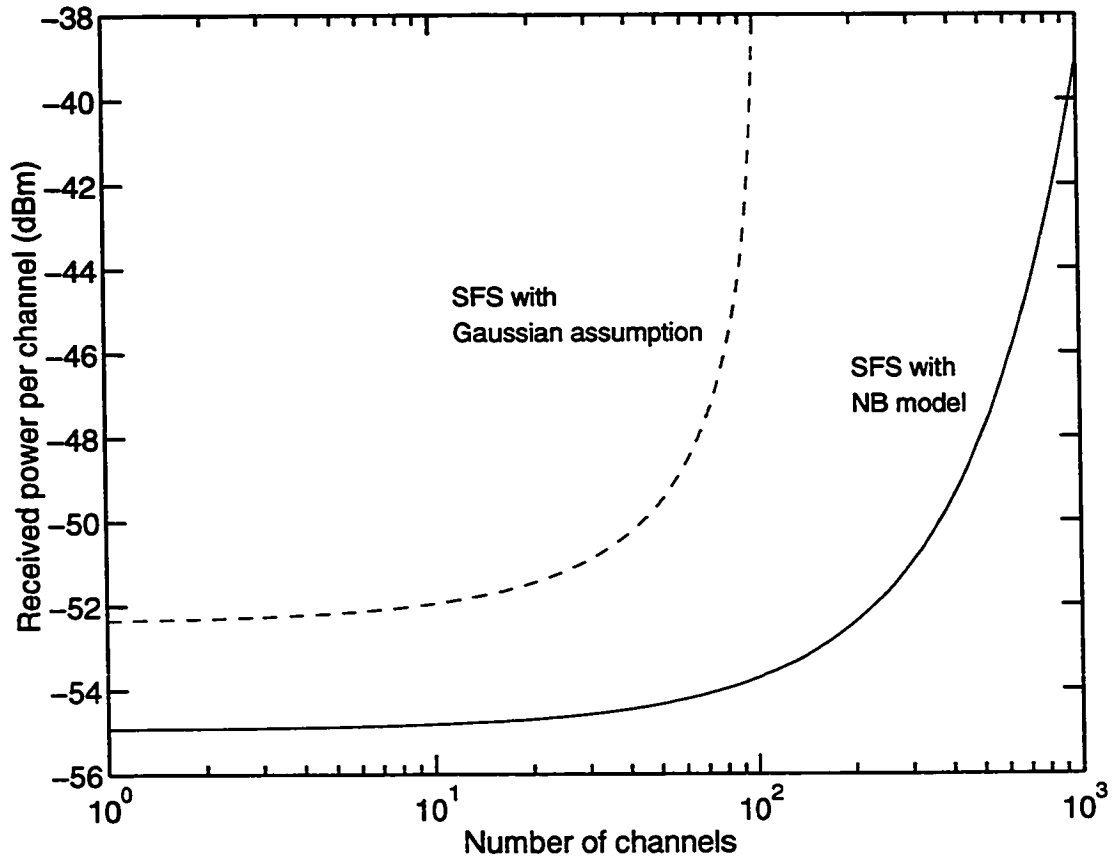


**Figure 4.2** Number of channels in a spectrum-sliced WDMA system.

Relationship between the number of spectrum-sliced WDMA channels and the required received power per channel. The BER value is  $10^{-9}$  at a 1 Gbps symbol rate ( $B_c = 500$  MHz). The linewidth of the polarized source is 30 nm and the detector quantum efficiency of the ideal receiver is 80% at 1550 nm. The channels are assumed to have identical rectangular lineshapes.

capacity of about 100 channels. It follows from the plot that a capacity of 1000 channels requires a total source power of about  $-7$  dBm, well within the range of output power of currently demonstrated fiber sources, which is typically in excess of a few milliwatts. Further amplification of the spectrum-sliced channel can be incorporated, either at the transmitter or the receiver, to overcome system losses or receiver noise.

One can show that the BER is lower bounded by using the fact that  $e^{-\alpha w}$  is convex over  $[0, \infty)$  and applying Jensen's inequality to (4.5) to obtain  $BER = E[e^{-\alpha W}]/2 \geq e^{-\alpha E[W]}/2$ . Thus, given an average integrated intensity, the quantum limit is the best that can be obtained. Accordingly, a light source that achieves this performance can be considered an ideal source, i.e. one that has a deterministic light intensity for which  $p_W(w) = \delta(w - E[W])$ , as would be expected from intuition. Figure 4.3 shows calculated BER values for the ideal laser source, the spectrum-sliced SFS with the Gaussian assumption and with the NB model. At the BER of  $10^{-9}$ , the NB model predicts the degradation from an ideal laser to be from 1.5 dB to 2.5 dB as the spectrum-sliced linewidth is reduced from 36 GHz to 18 GHz. The Gaussian assumption predicts a BER floor for high power level and significantly underestimates the true performance of the system.

#### 4.4 Performance under Gaussian Background Noise

In real systems, the presence of the background noise is unavoidable, as shown by the experimental results in Chapter 3. The ideal photoelectron counting receiver can only

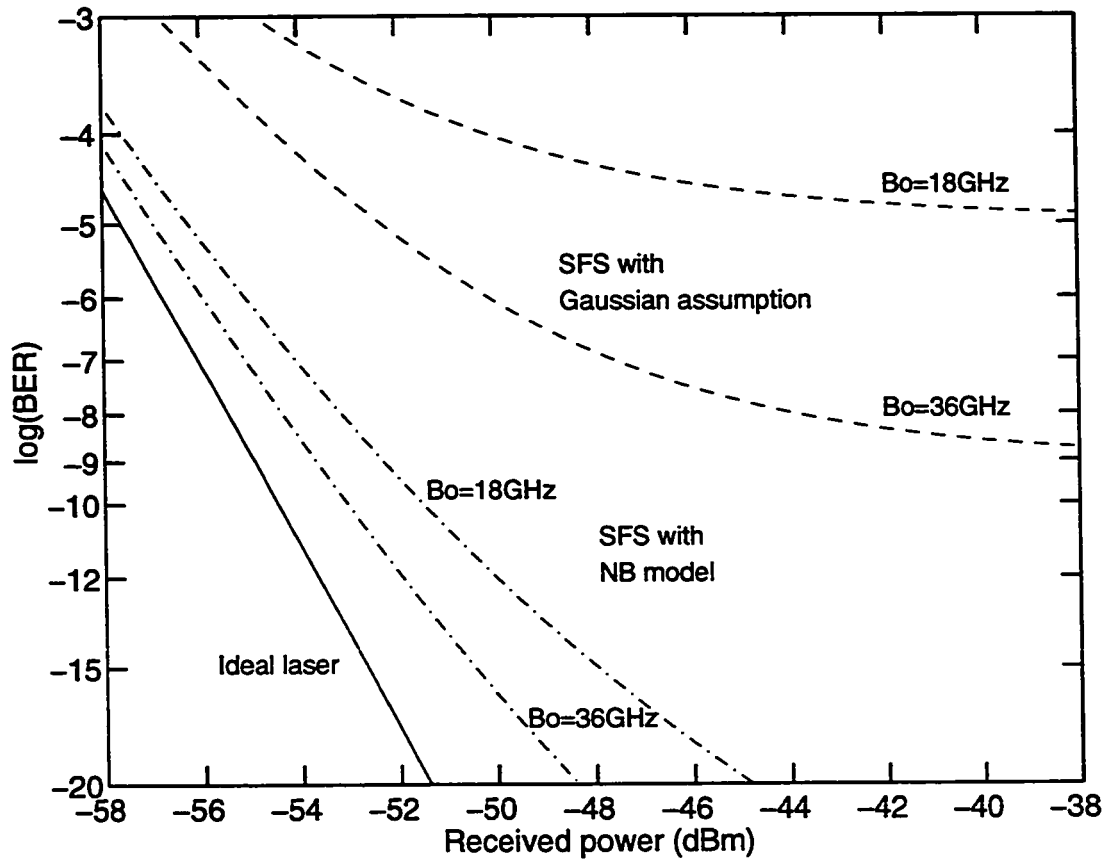


**Figure 4.3** BER comparison with an ideal receiver.

The symbol rate is 1 Gbps ( $B_c = 500\text{ MHz}$ ) and the example linewidths are 18 GHz and 36 GHz. The detector quantum efficiency is 80% at 1550 nm. Unlike the Gaussian assumption, the NB model predicts only a few dB's of degradation from an ideal laser at the  $10^{-9}$  BER.

be approached in practice. This receiver assumption must be relaxed for a realistic comparison with what is experimentally achievable. Taking the additive background noise into account will yield an optimum threshold that is greater than zero for ASK modulation. The resulting signal-dependent noise for symbol “1” is non-Gaussian and larger than the Gaussian noise associated with symbol “0”, meaning that the normalized optimum threshold should be reduced as the received power increases. While the Gaussian approximation in this case can be improved by optimizing the threshold settings [67], we emphasize that the tails of the NB and the Gaussian distribution behave very differently, and using the Gaussian approximation yields fundamentally inaccurate and pessimistic results. With binary FSK (using two spectrum-sliced channels — one for each symbol) or PPM modulations, the decision statistics for symbols “1” and “0” have the same distribution, resulting in an optimum threshold of zero that does not depend on the signal nor the noise characteristics. Again, the Gaussian approximation would incorrectly predict a performance floor due to the limiting SNR. The exact analysis for the various modulation formats that considers all statistical descriptions of the different random processes are considerably complicated. However under high received power, which is the situation of interest, an approximation based on the dominant statistical process can be made that reduces the complexity considerably while still yielding useful and consistent results.

Qualitatively, when the optical power level is below the threshold power of the receiver, the signal is dominated by the background noise, which can be modeled

well by a Gaussian. For high optical power, excess noise described by the NB model dominates. Thus the BER versus received power curves should follow a Gaussian behavior at low power level, change their slopes in the vicinity of the threshold power due to the increasing effect of excess noise, but continue to improve as the optical power increases as predicted by the NB model. This BER characteristic is illustrated in Figure 4.4 for a polarized SFS with uniform spectrum-sliced linewidths of 36 GHz and 18 GHz. The background noise of the PIN photodiode was taken to be  $P_n = 0.1 \mu\text{W}$  when referenced to the detector input. The detection bandwidth was 500 MHz for a 1 Gbps symbol rate, giving mode numbers of 36 and 18 for the example linewidths. As shown, the performance of the distributed feedback (DFB) diode laser at the example power levels is dominated by the Gaussian background noise, with  $BER = Q(.5P/P_n)$ . The performance of the SFS with the Gaussian assumption is given by  $BER = Q(P/P_*)$ , where:

$$P_* = P_n + \sqrt{P_n^2 + P(e/\mathcal{R}T + P/M)}. \quad (4.10)$$

The detector responsivity  $\mathcal{R}$  is taken to be 1 A/W at 1550 nm and  $e$  is the electronic charge. The second term in (4.10) represents the noise associated with symbol “1” that includes the background noise, shot noise and excess noise. The BER curves with the Gaussian assumption are plotted in Figure 4.4 as the “dashed” lines, showing the erroneous prediction of the performance floors at high power level.

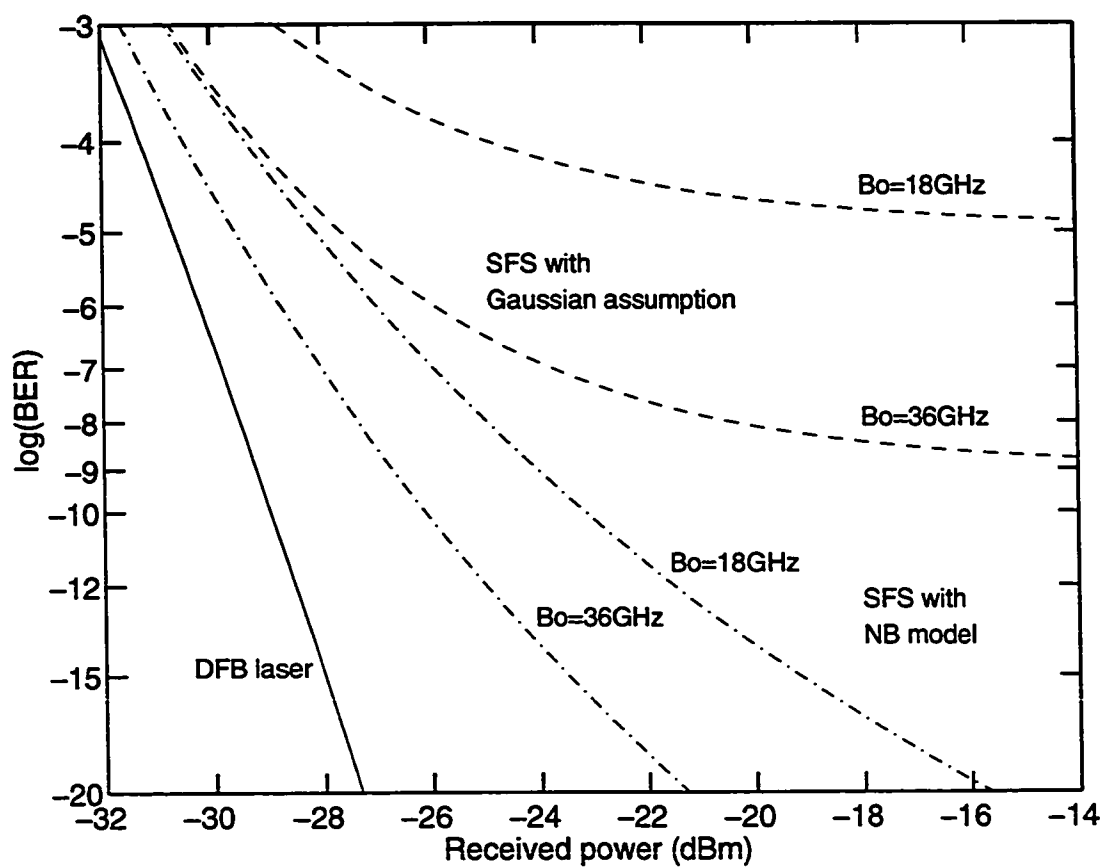


**Figure 4.4** BER comparison with Gaussian background noise.

The polarized spectrum-sliced WDMA system has an input background noise power of  $.1 \mu\text{W}$  in a 500 MHz detection bandwidth. The symbol rate is 1 Gbps and the responsivity of the PIN photodetector is  $1 \text{ A/W}$  at 1550 nm. The performance estimates with the Gaussian assumption (dash lines) are very pessimistic compared to the NB model (dot-dash lines) under high power for the example linewidths of 18 GHz and 36 GHz.

We estimate the system performance with the NB model by assuming that the noise statistics for symbol “1” are well described by a NB distribution. An exact analysis would consider a mixture of the NB and Gaussian statistics, and would be considerably more complicated. Unlike the Gaussian assumption, the statistical description based only on the NB model will become more accurate as the optical power received by the photodetector increases. The effect of the zero-mean background noise is incorporated into this model by preserving the total additive background noise power and the excess noise power. This is accomplished by effectively reducing the mode number of the NB distribution, thereby increasing its variance for a fixed mean intensity. Thus, it can be shown that an effective mode number of the NB distribution is given by:

$$M_e = \frac{M}{1 + M(P_n/P)^2}. \quad (4.11)$$

The measurement results in Chapter 3 have shown that in practice  $P_n$  is much larger than  $P_c$ , so that  $P_n\sqrt{M}$  is essentially the threshold power level of the receiver.

The BER with the effective NB distribution is then given by:

$$BER = .5Q(\alpha P/P_n) + .5 \sum_{k=0}^{\alpha E[K]} \Pr\{K = k\}. \quad (4.12)$$

The first term in (4.12) is the probability of error, according to the Gaussian statistics, associated with making the wrong symbol decision when symbol “0” is transmitted. Likewise, the second term is the probability of error, according to the effective NB statistics with mode number  $M_e$  in (4.11), when symbol “1” is transmitted. The

normalized threshold  $\alpha$  corresponds to the binary symbol-decision level based on the detector output. This likelihood threshold value is determined as the crossing between the zero-mean Gaussian probability density function for symbol “0” and the effective NB pmf for symbol “1”. Although there is no convenient analytical expression for  $\alpha$  in this case, it can be computed numerically from the parameters of the two statistics via direct evaluations of their distributional curves.

The performance estimates based on (4.12) are plotted as the “dot-dashed” curves in Figure 4.4 for the example linewidths. In comparison to the ideal laser at the BER of  $10^{-9}$ , the power penalty due to the thermal nature of the SFS increases from about 2.5 dB to 5 dB as the optical linewidth is reduced from 36 GHz to 18 GHz. When compared with Figure 4.3, the degradation from the ideal photoelectron counting receiver due to the background noise is in the order of 30 dB. The results show that the Gaussian assumption underestimates the system performance when excess noise dominates, especially under high power and narrow linewidth conditions. We note that the referenced experimental results show the change in the slopes of the BER curves [53], [59], [60], [61], but not the floor predicted by the Gaussian approximation. The experimental results were in fact reported to be better than the Gaussian prediction in some cases [53]. They are consistent with the qualitative behavior of the NB results given in Figure 4.4.



## 4.5 Remarks

The power penalties of the SFS with either ideal or real receiver assumptions are within a few dBs of one another according to the example calculations. Thus, the analytical results, while ideally simple, can provide useful performance estimates in real systems. For example, the required optical power per channel as calculated in Figure 4.2 can be expected to be around 30 dB higher for a receiver that has a background noise level of  $.1 \mu\text{W}$  referenced to the input. The results obtained from the Gaussian assumption and the effective NB model can be interpreted as the upper and lower bounds on the performance, respectively. As a function of the optical power, these bounds are not uniformly tight: the Gaussian upper bound is tight for low power, and the NB lower bound is tight under high power. A more accurate calculation of the system performance, especially for the optical power near the threshold power level of the receiver, would require an exact analysis that considers a mixture of the Gaussian and NB statistics.

As we have noted in Sec. 3.4, the noise figure of the EDFA is function of the wavelength within the EDFA bandwidth. The system performance of spectrum-sliced SFS is therefore generally expected to also be wavelength dependent: the excess noise amplitude may vary as the receiver is tuned to different slices of the spectrum.

## 4.6 Summary

The performance of a spectrum-sliced WDMA system using the SFS, in terms of BER, number of channels, and received power, is fundamentally different from the SNR-limited performance that would have been predicted with a Gaussian assumption. Fairly simple, yet rigorous, BER analysis was obtained for a system model consisting of the SFS and a detector described by a Poisson photodetection process. The analytical results of (4.6) through (4.9) represent the performance limits for the SFS, much like the quantum limit for an ideal laser is  $e^{E[K]}/2$ . The NB model correctly predicts the asymptotic result obtained purely from physical considerations, i.e., the “ideal” thermal source, with a spectral characteristic totally opposite to the ideal laser, should have the same quantum limit. The analytical results based on the NB model are in accord with our physical intuition that the system performance should improve as more optical power is received, barring any nonlinear effects. In this sense the Gaussian approximation leads to a rather counter-intuitive, or non-physical, prediction. The results here illustrate that the SNR, although a useful parameter, is not a true measure of the performance or the BER.

The performance estimates based on an effective NB model that incorporates the additive background noise, have demonstrated the same performance characteristics as the analytical results for the ideal receiver. We note that the effective NB model given by (4.11) and (4.12) is consistent in that it approaches the ideal analytical results as the background noise level is reduced.

When estimating the system performance at a high received power level, such that the input light intensity exceeds the threshold power of the receiver and excess noise dominates the decision statistics, the Gaussian assumption underestimates the BER and the number of channels, while it overestimates the required received power. In particular, the performance analysis using the true noise statistics shows that design compromises between the number of channels and the received power level are possible to achieve the desired symbol and bit-error rates. This has significant implication for spectral CDMA systems that use a large number of spectral chips to support many subscribers.

## Chapter 5

### Performance of Spectral Amplitude CDMA

We analyze the performance of the incoherent CDMA system that is based on the spectral encoding of a broadband SFS and correlation detection as described in Chapter 2. Bipolar,  $+1/-1$ , spreading codes that have been developed for the radio domain are employed. Orthogonality between users can theoretically be achieved, in spite of the incoherent reception of the optical signal. The performance in terms of the SNR and the probability of error ( $P_e$ ) is found to depend on the number of active users, even when orthogonal user signatures are used. This is different from the RF domain where the system performance is not affected by the presence of orthogonal users.

The performance analysis is based on the NB statistics and the additive light model to account for the thermal characteristics of the SFS. The SNR and  $P_e$  were computed and compared to a binary FSK, spectrum-sliced WDMA. The results demonstrate the interference-limited behavior of CDMA that imposes a performance penalty on the system due to the thermal nature of the SFS.

## 5.1 System Description

We consider the spectral encoding scheme described in Sec. 2.4.2 that employs bipolar codes and SFS. Figure 5.1 illustrates the incoherent spectral amplitude CDMA system. A portion of the power spectrum of an erbium-doped SFS is divided into  $2N$  spectral slices, or chips, for encoding a bipolar code  $X$  of a length- $N$  by means of a spectrum processor. The spectrum processor processes the power spectrum of the optical signal in the manner described by the example encoder pair  $E(\lambda)$  and  $\bar{E}(\lambda)$  depicted in Figure 2.7. It generates two outputs with complement spectral responses,  $A$  and  $\bar{A}$ . The waveguide switch selects one output for transmission according to the value of the binary symbol  $b$ . This allows orthogonal signalling of the digital data. The spectral encoded and data modulated light is connected to the network through a  $J \times J$  star coupler. At the receiver, the optical signal goes through a spectrum processor that is matched to a bipolar code  $Y$ , also of length- $N$ , of the desired user. The outputs of the spectrum processor are photodetected and the detector currents subtracted to obtain an estimate of the transmitted symbol.

Figure 5.2 illustrates the spectral amplitude encoding of bipolar codes. Let  $A(i)$  denote the pattern of the  $2N$  spectral chips, of bandwidth  $B_c$  each, that is based on the 2-tuple unipolar code  $(U, \bar{U})$  as follows:

$$A(i) = \begin{cases} U(i), & 0 \leq i \leq N-1 \\ \bar{U}(i-N), & N \leq i \leq 2N-1. \end{cases} \quad (5.1)$$

**Figure 5.1** Incoherent optical CDMA system based on spectral amplitude encoding of bipolar codes.

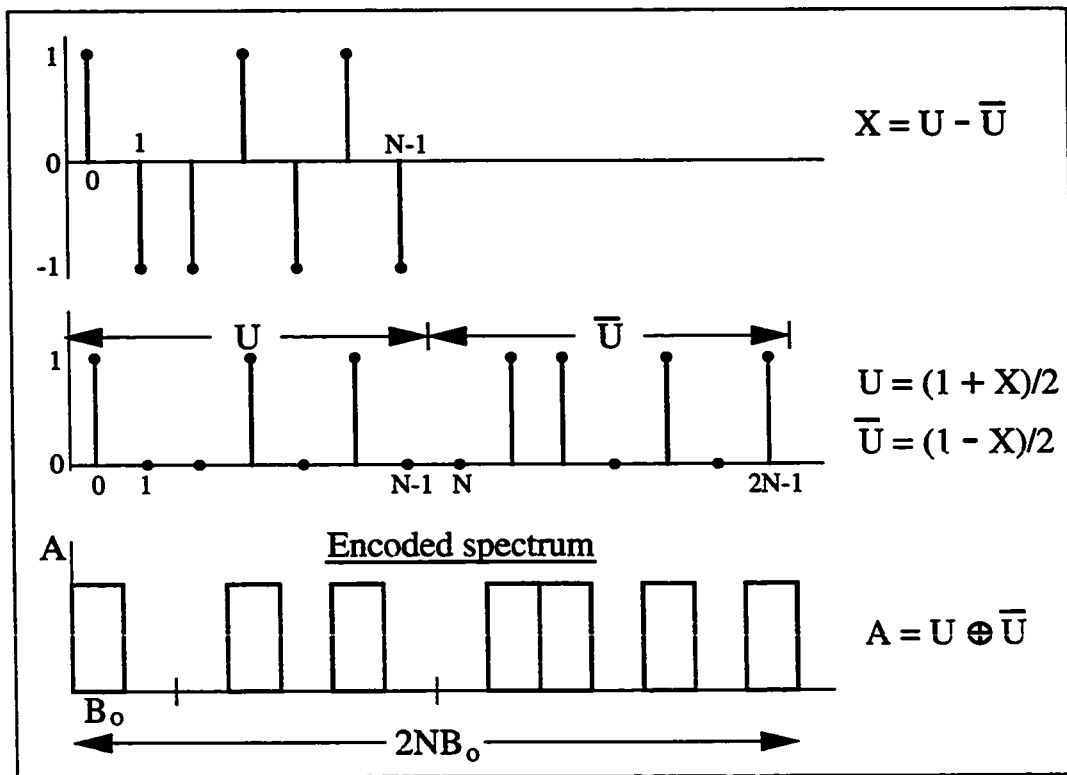


**Figure 5.2** Encoding of a broadband spectrum.

The spectral amplitude,  $A(i)$ , of the  $2N$  spectral chips is encoded by the concatenated unipolar code obtained from a length- $N$  bipolar code.

$A(i)$  corresponds to the concatenated unipolar code  $U \oplus \bar{U}$ , where  $U$  is obtained from  $X$  by replacing each  $-1$  by  $0$  and  $\bar{U}$  is the complement of  $U$ . The spectral responses of the spectrum processor outputs are therefore described by  $A(i)$  and  $\bar{A}(i)$ , which encode  $U \oplus \bar{U}$  and  $\bar{U} \oplus U$ , or  $X$  and  $-X$ , respectively.

The spectrum processor at the receiver in Figure 5.1 is matched to the desired user code  $Y$ , with the 2-tuple unipolar code  $(V, \bar{V})$  that describes the spectral response outputs,  $B(i)$  and  $\bar{B}(i)$ , in a similar manner. If the received signal was encoded with  $X$ , then the spectrum processor outputs at the receiver correspond to:

$$\sum_{i=0}^{2N-1} A(i)B(i) = \sum_{i=0}^{N-1} U(i)V(i) + \bar{U}(i)\bar{V}(i), \quad (5.2)$$

and:

$$\sum_{i=0}^{2N-1} A(i)\bar{B}(i) = \sum_{i=0}^{N-1} U(i)\bar{V}(i) + \bar{U}(i)V(i). \quad (5.3)$$

By subtracting (5.3) from (5.2), we obtain:

$$\sum_{i=0}^{N-1} [U(i) - \bar{U}(i)][V(i) - \bar{V}(i)] = \sum_{i=0}^{N-1} X(i)Y(i) = \theta_{XY}, \quad (5.4)$$

where  $\theta_{XY}$  denotes the zero-shift crosscorrelation of  $X$  and  $Y$ . The output current of the photodiode pair, connected in the balanced configuration in Figure 5.1, is therefore proportional to the difference of (5.2) and (5.3), or  $\theta_{XY}$ . The desired user can be detected if the codes are matched. In the multi-user situation, the sampled input to the threshold comparator,  $\theta$ , is proportional to  $\theta_{XY}$  and the multiple access interference from other users, plus noise. The interference to the desired user from other users is suppressed by using bipolar codes with ideally zero, or low, crosscorrelations.



The encoded portion of the power spectrum is taken to be uniform, so that the power in each spectral chip is identical over the total bandwidth  $B$ . We also assume that the codes of the interfering users are orthogonal to the desired user. Assuming that  $N$  is a power of 2, there are  $N$  orthogonal Walsh codes that can be assigned to the users. This is a situation of interest because it provides a benchmark comparison to the binary FSK, spectrum-sliced WDMA system shown in Figure 5.3. This system is similar to the ASK-WDMA system shown in Figure 4.1, with the exception that two spectral chips are used for orthogonal transmission of symbol “1” and “0”, respectively. Obviously, the FSK-WDMA system can also support  $N$  users on a strictly non-interfering basis using the same  $2N$  spectral chips. The crosstalks between the adjacent chips are taken to be ideally zero, assuming ideal rectangular chip. The bandwidth of each spectral chip is the same for all users:  $B_o = B/2N$ . The power transmitted by the  $j^{\text{th}}$  user is denoted  $P_j$ , so that the chip power of user  $j$  is  $P_j/2N$ . The mean photoelectron count associated with each chip from user  $j$  is given by:  $\overline{K}_j = \eta P_j T / 2N h \nu$ . We see that CDMA is  $N$  times more efficient in using the source spectral power: the power of user  $j$  is  $P_j/2$ , or  $N\overline{K}_j$ , for CDMA versus  $P_j/2N$ , or  $\overline{K}_j$  for WDMA. The dark currents of the two detectors are assumed to be identical with the mean photoelectron count denoted  $\overline{K}_d$ . From the thermal nature of the SFS, we assume that the count statistics for each detector are given by a NB model that includes the effect of the detector dark current, an assumption similar to [43]. The

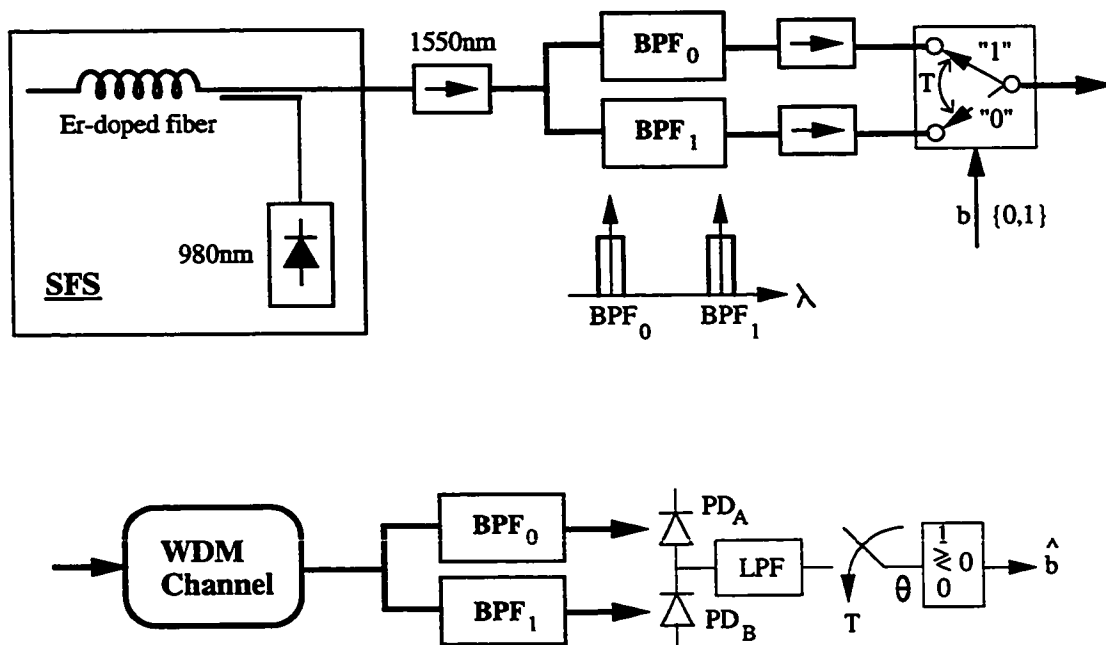


**Figure 5.3** Block diagram of a binary FSK, spectrum-sliced WDM system.

mode number of each spectral chip is equal to:  $M_o = B_o T$ , for a polarized SFS. We consider user 1 to be the desired user and assume equal *a priori* symbol probability.

## 5.2 SNR Analysis

As we have realized in Sec. 2.2, the binary FSK-WDMA is particular case of spectral CDMA. The photoelectron count outputs of the detectors in Figure 5.3 are effectively compared against each other and the symbol decision is made based on the largest output. Without loss of generality, let  $b = 1$ . The mean value of  $\theta$  is:  $E[\theta] = (\bar{K}_1 + \bar{K}_d) - \bar{K}_d = \bar{K}_1$ . From the NB model, the variance of the FSK-WDMA system is given by:

$$\begin{aligned}\sigma_{\text{WDMA}}^2 &= (\bar{K}_1 + \bar{K}_d)[1 + (\bar{K}_1 + \bar{K}_d)/M_o] + \bar{K}_d(1 + \bar{K}_d/M_o) \\ &= (\bar{K}_1 + 2\bar{K}_d) + \left[(1 + \bar{K}_d/\bar{K}_1)^2 + (\bar{K}_d/\bar{K}_1)^2\right] \frac{\bar{K}_1^2}{M_o}.\end{aligned}\quad (5.5)$$

The second term of (5.5) accounts for the excess noise of both detectors due to the thermal nature of the SFS. The first term reflects the shot noise. The signal-to-noise power ratio is:

$$SNR_{\text{WDMA}} = \frac{\bar{K}_1}{1 + 2\bar{K}_d/\bar{K}_1 + \left[(1 + \bar{K}_d/\bar{K}_1)^2 + (\bar{K}_d/\bar{K}_1)^2\right] \bar{K}_1/M_o}.\quad (5.6)$$

If the chip power is small, such that the average count per mode of each chip,  $\bar{K}_1/M_o$ , is much less than 1, then  $SNR_{\text{WDMA}} \approx \bar{K}_1/(1 + 2\bar{K}_d/\bar{K}_1)$  and the statistics are approximately Poisson. For large optical power ( $\bar{K}_1/M_o \gg 1$ ), the limiting SNR is equal to the mode number  $M_o$ , as discussed in Chapter 3.

For the spectral amplitude CDMA system, we consider the SNR of the decision statistic,  $\theta$ , at the input to the threshold comparator. We model  $\theta$  as the difference of two independent random variables  $K_A$  and  $K_B$  that represent the photoelectron counts measured by the two photodetectors  $PD_A$  and  $PD_B$  during the symbol interval  $T$ :

$$\theta = K_A - K_B. \quad (5.7)$$

$K_A$  and  $K_B$  are described by the NB models for the photoelectron count statistics of each detector. We assume that there are  $J$  simultaneously active users including the desired user 1. The distributions of  $K_A$  and  $K_B$ , conditioned on the transmitted symbol of user 1, obey the NB pmf. Their conditional means are given by:

$$E[K_A|b = 1] = E[K_B|b = 0] = N\bar{K}_1 + .5N \sum_{j=2}^J \bar{K}_j + \bar{K}_d \quad (5.8)$$

$$E[K_A|b = 0] = E[K_B|b = 1] = .5N \sum_{j=2}^J \bar{K}_j + \bar{K}_d, \quad (5.9)$$

The expected value of  $\theta$  is thus  $N\bar{K}_1$ . Its variance is given by:

$$\begin{aligned} \sigma_{\text{CDMA}}^2 = & \left( \sum_{j=1}^J \bar{K}_j + 2\bar{K}_d \right) + \left( N\bar{K}_1 + .5N \sum_{j=2}^J \bar{K}_j + \bar{K}_d \right)^2 / M_A \\ & + \left( .5N \sum_{j=2}^J \bar{K}_j + \bar{K}_d \right)^2 / M_B. \end{aligned} \quad (5.10)$$

$M_A$  and  $M_B$  are the effective mode numbers of the NB pmf's for  $PD_A$  and  $PD_B$ . From (3.3), they depend on the power spectra of the thermal light input to the detectors under the additive light model [28] for combining the optical signals from the users. As a result of encoding, these power spectra generally are piece-wise constant over

each spectral chip, despite the fact that each user's power spectrum is assumed to be uniform. To avoid the near-far effect, we further assume at this point that each user has the same source power, so that  $\overline{K}_j = \overline{K}_1$ ,  $j = 1, 2, \dots J$ . We then obtain from (5.10) that:

$$\begin{aligned} \sigma_{\text{CDMA}}^2 = & (JN\overline{K}_1 + 2\overline{K}_d) + [.5N(J+1)\overline{K}_1 + \overline{K}_d]^2/M_A \\ & + [.5N(J-1)\overline{K}_1 + \overline{K}_d]^2/M_B. \end{aligned} \quad (5.11)$$

Exact calculation of the effective mode numbers  $M_A$  and  $M_B$  are difficult since it requires a detailed description of the decoder spectra input to the detectors. This involves piece-wise additions of the code waveforms across the encoded spectrum and can be quite tedious, especially when the number of users is large. In order to circumvent this difficulty, we will instead compute the maximum values of  $M_A$  and  $M_B$  so that an upper bound on the SNR is obtained. From Chapter 3, the mode number is proportional to the product of the symbol or detection period and the normalized power bandwidth of the input light to the detector. Thus, given an average input power, we should seek the maximum input bandwidth that can accomodate the corresponding thermal light. Because of spectral encoding, the thermal light incident on each detector only occupies  $N$  spectral chips or one half of the total source bandwidth. The maximum number of modes is therefore  $NM_o$  for each detector. This can be obtained rigorously by applying Schwarz's inequality to the expression for the normalized power bandwidth of (3.3) under the fixed total power constraint. The

accuracy of this approximation for  $M_A$  and  $M_B$  is expected to improve as the number of users increases. This is because the decoder spectrum seen by each detector will be more or less uniform due to the pseudo-random nature of the codes.

From (5.11), the variance of  $\theta$  is then given as:

$$\sigma_{\text{CDMA}}^2 = (JN\bar{K}_1 + 2\bar{K}_d) + \left[ \frac{.5N^2(1 + J^2) + 2NJ\bar{K}_d/\bar{K}_1 + (\bar{K}_d/\bar{K}_1)^2}{N} \right] \frac{\bar{K}_1^2}{M_o}. \quad (5.12)$$

Again, the second term of (5.12) accounts for the excess noise of both detectors due to the thermal nature of the incident light. The first term reflects the shot noise that is equal to the sum of the average counts of each detector. The signal-to-noise power ratio for spectral CDMA system is:

$$SNR_{\text{CDMA}} = \frac{N\bar{K}_1/J}{1 + \frac{2\bar{K}_d/\bar{K}_1}{NJ} + \left[ \frac{1 + J^2}{2J} + \frac{2\bar{K}_d/\bar{K}_1}{N} + \frac{(\bar{K}_d/\bar{K}_1)^2}{N^2J} \right] \frac{\bar{K}_1}{M_o}} \quad (5.13)$$

If the average count per mode for each chip,  $\bar{K}_1/M_o$ , is much less than 1, then shot noise dominates and the SNR of CDMA system is better by a factor of approximately  $N/J$  when compared to WDMA system (5.6). Thus, since  $J \leq N$ , the efficient exploitation of the source power in CDMA results in better SNR performance than WDMA under shot-noise limited condition. However, for sufficient power levels that excess noise dominates, the limiting SNR for CDMA is given by:

$$SNR_{\text{CDMA}}^* = \frac{2N}{1 + J^2} M_o. \quad (5.14)$$

In comparison, the limiting SNR for WDMA system from (5.6) is  $M_o$ . Thus the effect of excess noise is quite severe in CDMA: the limiting SNR is worse if the number of

active users exceeds  $J = \sqrt{2N-1}$ . This stems from the thermal nature of the SFS that increases the noise contributed by those spectral chips that overlap due to the users' codes. In the WDMA system there are no such overlaps. A direct comparison of the two system can be obtained by taking the ratio of the SNR's given by (5.13) and (5.6), under the assumption that the optical power is much larger than the dark current (i.e.,  $\bar{K}_d/\bar{K}_1 \ll 1$ ):

$$\rho \approx \frac{1 + \bar{K}_1/M_o}{1 + \frac{1+J^2}{2J}(\bar{K}_1/M_o)} N/J. \quad (5.15)$$

An interpretation of the factor  $2N/(1+J^2)$  in (5.14) can be seen as follows. According to (5.15), if we were to keep the excess noise in CDMA to a level comparable to WDMA, then the chip power in CDMA must be reduced by a factor of  $2J/(1+J^2)$ . This also reduces the average count for CDMA by the same factor, and thereby reduces the SNR to  $(N/J) \times 2J/(1+J^2) = 2N/(1+J^2)$ . Example plots of  $\rho$  versus  $J$  with  $\bar{K}_1/M_o$  as a parameter are shown in Figure 5.4 for  $N = 64$ . We recall from Sec. 3.2 that the ratio  $\bar{K}_1/M_o$  is the count degeneracy of the source and is proportional to its spectral intensity. Typical values of  $\bar{K}_1/M_o = \eta P_1/h\nu B$ , range from 3 to 3000 for power levels between  $1.0 \mu\text{W}$  and  $1.0 \text{mW}$ , for a source bandwidth of about 1% at 1550 nm. The system is thus dominated by excess noise in practice. The plots show that excess noise effectively nullifies the SNR advantage of CDMA over WDMA. For a comparable limiting SNR performance, the number of users in CDMA must be reduced from 64 to 11 as the excess noise becomes increasingly dominant. The count

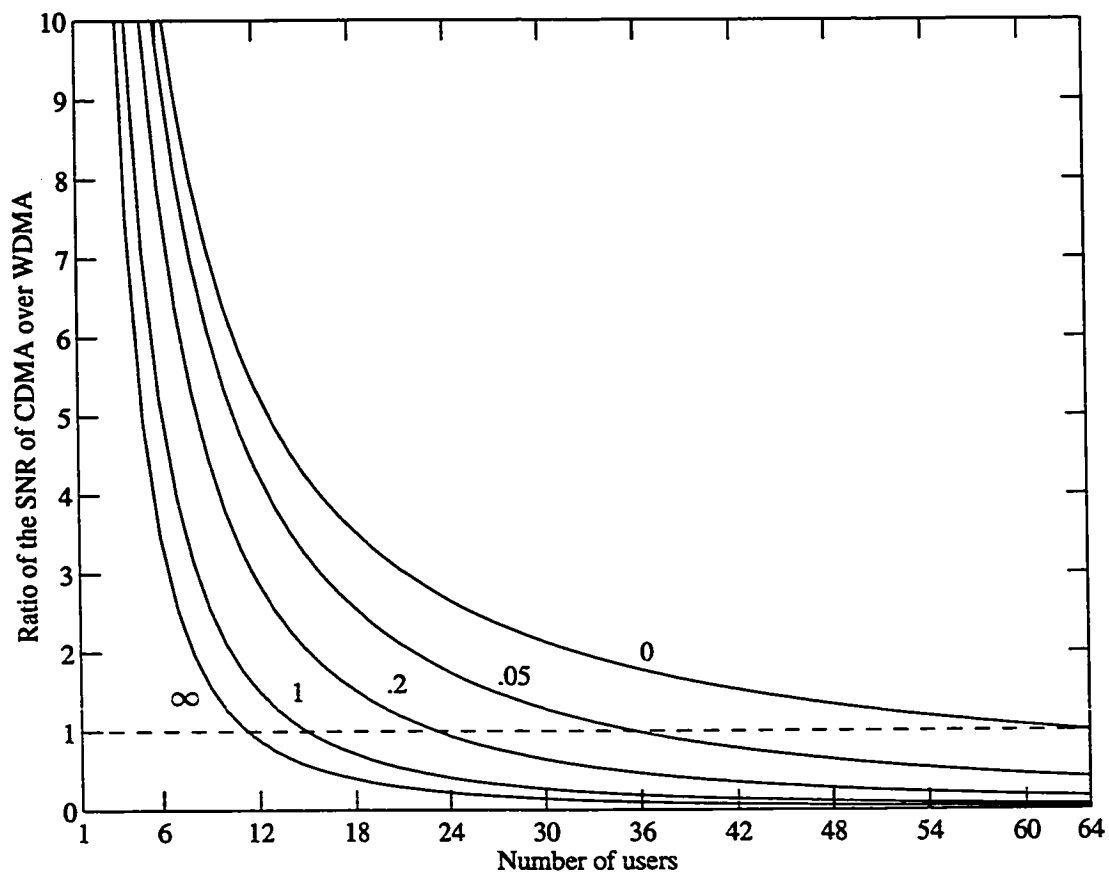


**Figure 5.4** SNR comparison of spectral CDMA and FSK-WDMA.

The average count per mode for each spectral chip,  $\bar{K}_1/M_o$ , or the count degeneracy parameter of the SFS, varies from 0 for shot noise (right-most curve) to  $\infty$  for excess noise (left-most curve). With  $N = 64$  (128 spectral chips), excess noise limits the number of users in CDMA to 11 for limiting SNR values comparable to WDMA.



degeneracy parameter tells us that for good noise performance, the “preferred” SFS should have a very low spectral intensity, i.e., a wide bandwidth for a given power level.

The SNR analysis points out the major difference between CDMA systems in the optical domain and RF domain. In the RF domain, the noise is additive and does not depend on the signal: if the user codes are orthogonal, the SNR is independent of the number of users. In the optical domain, the noise of each detector itself is generated by the total optical power in the channel, which becomes larger as more users are present. Thus even if the user codes are orthogonal, the noise cannot be canceled. The decision statistic,  $\theta$ , is the difference of two very noisy quantities,  $K_A$  and  $K_B$ . This effect is compounded by the effect of excess noise due to the thermal nature of the SFS. The signal advantage of CDMA over WDMA from the efficient exploitation of the source power,  $P_1/2$  versus  $P_1/2N$  or  $N\bar{K}_1$  versus  $\bar{K}_1$ , cannot overcome the noise contributed by other users by virtue of their presence despite the orthogonality of the spreading codes. Strict orthogonality or non-interference signalling as in WDMA system (or TDMA) therefore can never be achieved in optical CDMA with either time or spectral encoding, even with the use of orthogonal codes.

### 5.3 Probability of Error Analysis

In this section, we analyze and compare the probability of error for the spectral CDMA system with the FSK-WDMA system. Due to the symmetry in the descriptions of

both systems, the probability of error for CDMA or WDMA is given by:

$$P_e = \Pr\{\theta < 0|b = 1\} + \frac{1}{2}\Pr\{\theta = 0|b = 1\}. \quad (5.16)$$

The NB descriptions for  $K_A$  and  $K_B$  that were employed to compute the SNR's in Sec. 5.2 are specified by the means and the mode numbers of the counting statistics.

Under  $H_1$ , we have for WDMA:

$$P_{K_A}(k) \sim \text{NB}(\overline{K}_1 + \overline{K}_d, M_o) \quad (5.17)$$

$$P_{K_B}(k) \sim \text{NB}(\overline{K}_d, M_o), \quad (5.18)$$

and for CDMA:

$$P_{K_A}(k) \sim \text{NB}(.5(J+1)N\overline{K}_1 + \overline{K}_d, NM_o) \quad (5.19)$$

$$P_{K_B}(k) \sim \text{NB}(.5(J-1)N\overline{K}_1 + \overline{K}_d, NM_o). \quad (5.20)$$

Unfortunately, no closed analytical expression exists to described the difference statistic,  $\theta$ , of two NB random variables. Because of the limiting SNR characteristics of the NB random variables, we will refrain from approximate calculations of  $P_e$  based on the Gaussian assumption. Instead, we compute  $P_e$  exactly using numerical methods. From (5.7), the pmf of  $\theta$  is the correlation of the pmf's of  $K_A$  and  $K_B$ . It can be shown that the probability of error is given as:

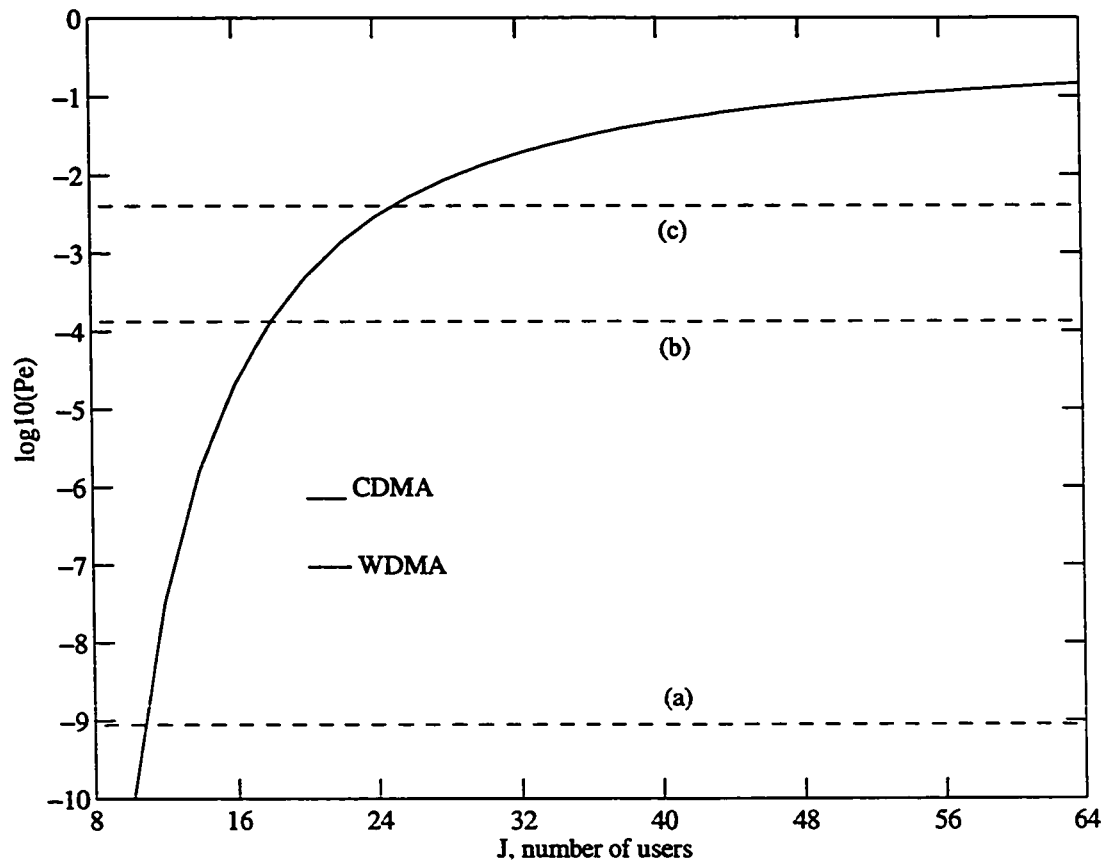
$$P_e = 1 - \sum_{k=0}^{\infty} P_{K_A}(k) \left[ \sum_{n=0}^k P_{K_B}(n) + \frac{1}{2}P_{K_B}(k) \right]. \quad (5.21)$$

Figure 5.5 shows the example calculation of  $P_e$  versus the number of users  $J$  for  $N = 64$ . The results demonstrate the interference-limited nature of CDMA. It also

illustrates the effect of excess noise on the system performance. The number of user is limited to 11 for a  $P_e$  comparable to FSK-WDMA system, consistent with the prediction from the SNR analysis. The comparison improves somewhat if we take into account the crosstalk between adjacent spectral chips in WDMA system and reduce the chip bandwidth for crosstalk protection.

The probability of error can be improved by increasing the number of modes per chip,  $M_o$ , as shown in Figure 5.6. Notice that the improvement with larger  $M_o$  diminishes as the number of users increases. Again the interference-limited behavior of CDMA is deteriorated by the excess noise of the SFS. For a given symbol rate, or detection interval  $T$ , the number of modes  $M_o$  can only be increased by making the spectral chips larger, thereby reducing the code length and hence the number of users, if the source bandwidth is fixed.

The probability of error performance for the prototype system in Chapter 6 has been computed using (5.19), (5.20) and (5.21). The results are plotted in Figure 5.7 as a function the optical power. The example calculations are shown for 1 to 8 users. The plot shows that the performance improves as more power is available. However, when there are multiple users, the effect of excess noise from the users is very difficult to overcome simply by increasing the optical power, as we have assumed that the users have equal power to avoid the near-far effect.



**Figure 5.5** Probability of error versus the number of users.

System parameters:  $N = 64$ ,  $\bar{K}_1 = 60$ ,  $\bar{K}_d = 6$ ,  $M_o = 36$ . CDMA is interference-limited compared to FSK-WDMA with no guard band (a), guard band = .5 chip (b), guard band = 2/3 chip (c). The thermal nature of the SFS imposes a performance penalty on CDMA system when the number of users is large.

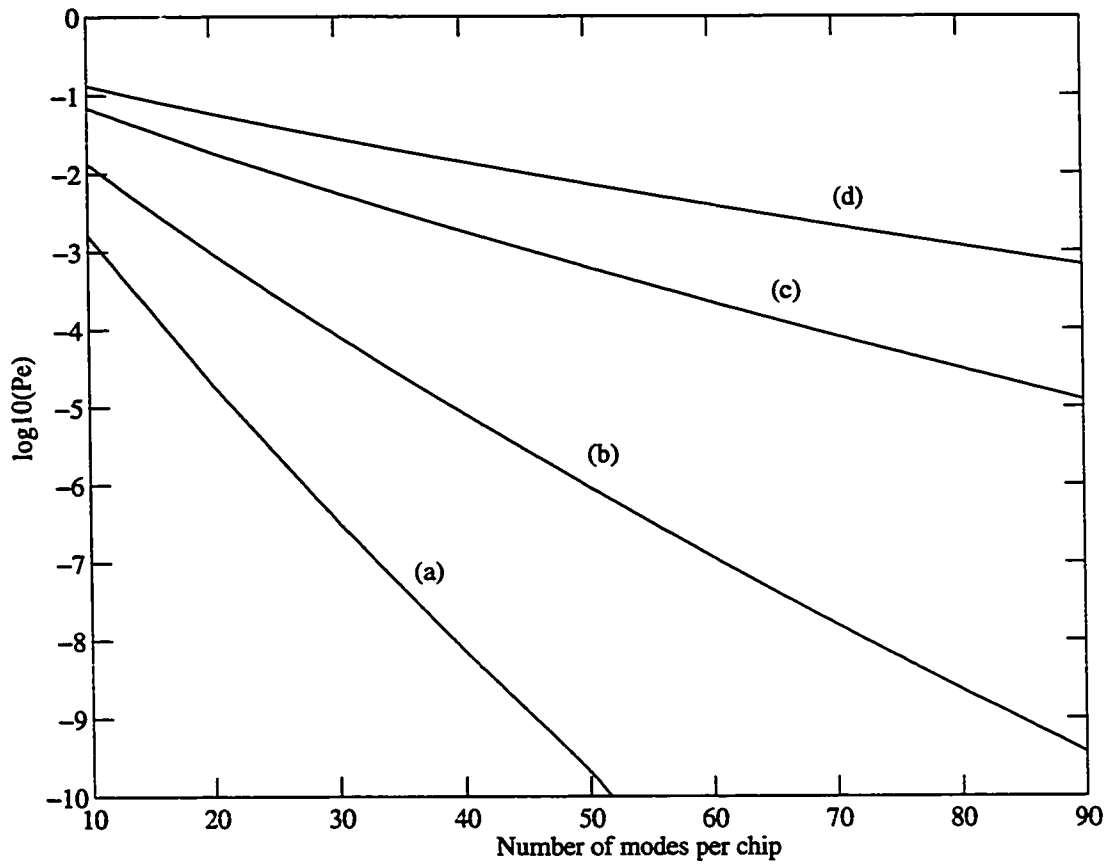


**Figure 5.6** Probability of error versus mode number per chip,  $M_o$ .

System parameters:  $N = 64$ ,  $\overline{K}_1 = 60$ ,  $\overline{K}_d = 6$ . The number of users  $J$  is 12 (a), 16 (b), 24 (c) and 32 (d).

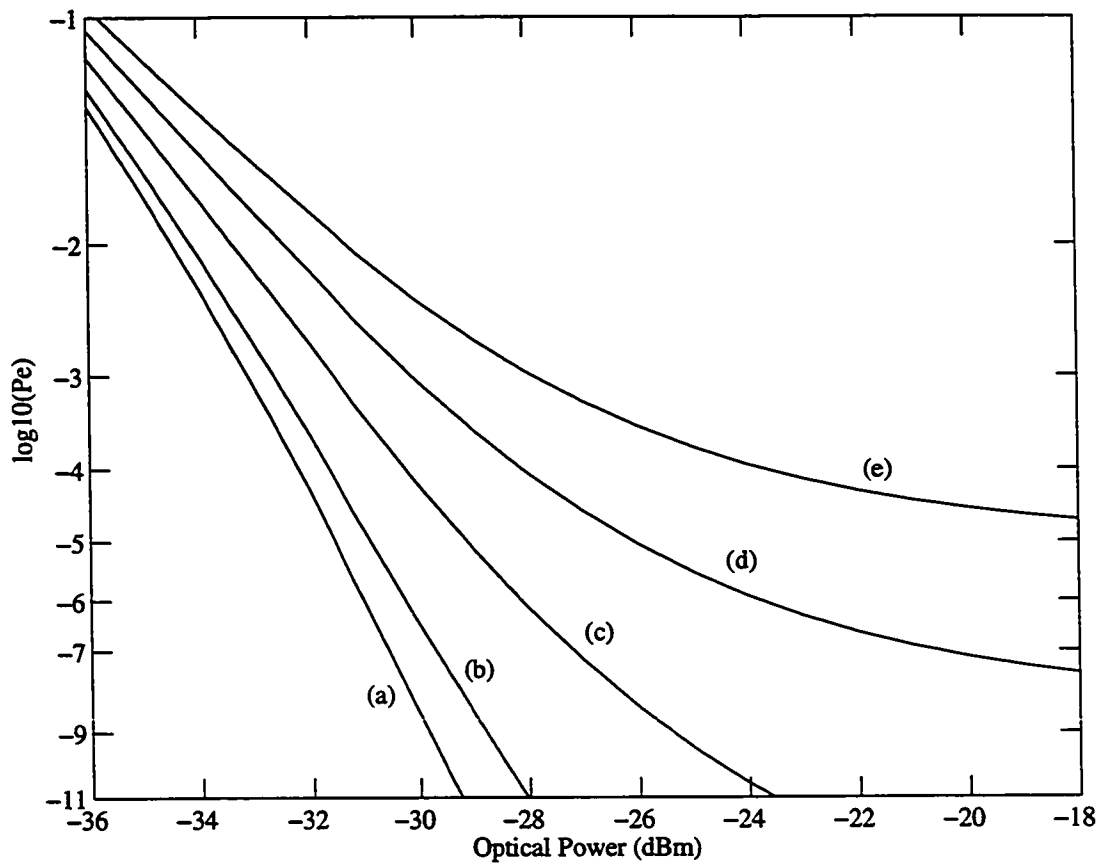


**Figure 5.7** Probability of error versus optical power.

Example calculations for the prototype system in Chapter 6:  $N = 16$ ,  $M_o = 36$ . The input noise power of the detectors is  $.1 \mu\text{W}$  in a 500 MHz bandwidth for a 1 Gbps symbol rate. The detector responsivity is 1 A/W at 1550 nm. The incident light at the decoder is assumed to be polarized. The performance is interference-limited as the number of users increases:  $J = 1$  (a), 2 (b), 4 (c), 6 (d), 8 (e).

## 5.4 Summary

The performance of spectral CDMA system is very dependent on the thermal nature of the light source. The NB statistics and the additive light model for combining the optical signals from multiple users were employed to account for the thermal characteristics of the SFS. We computed the performance of CDMA and FSK-WDMA to find that, unlike the RF system, the performance in terms of SNR and probability of error depends on the number of users, even when orthogonal user signatures are used. This is a consequence of the photodetection process that is compounded by the excess noise effect of the SFS. The results demonstrated the interference-limited behavior of CDMA that imposes a performance penalty on the system due to the thermal nature of the broadband source.

The negative binomial channel is thus a very noisy communication channel. It is expected therefore that some form of forward error-correction coding of the data to combat the channel noise will be required for spectral CDMA when the number of users is large.

## Chapter 6

# Experimental Demonstration of Optical CDMA System

We report the first experimental demonstration of spectral encoding and decoding techniques using bipolar codes for optical CDMA. Based on the modulation and detection principles developed in Chapter 2, we encoded the power spectrum of an erbium-doped superfluorescent fiber source with bipolar codes. A prototype system consisting of two encoders and one decoder was implemented with bulk optics and free-space transmission of the optical beams. The measurement results verify the correlations between the bipolar codewords, and demonstrate the rejection of the multiple access interference.

### 6.1 Experimental Description

The block diagram of the experimental setup is shown in Figure 6.1. The configuration of the SFS is similar to Figure 3.1 with a 25 m of highly doped, erbium fiber donated by AT&T. Under the full drive of the diode laser, about 35% of the 100 mW pump light at 980 nm was coupled into the fiber through the dichroic mirror (DM). The backward ASE output from the fiber is unpolarized and was collimated to beam of about 6 mm in diameter. About 5 mW of optical power was collected after the DM over a 50 nm



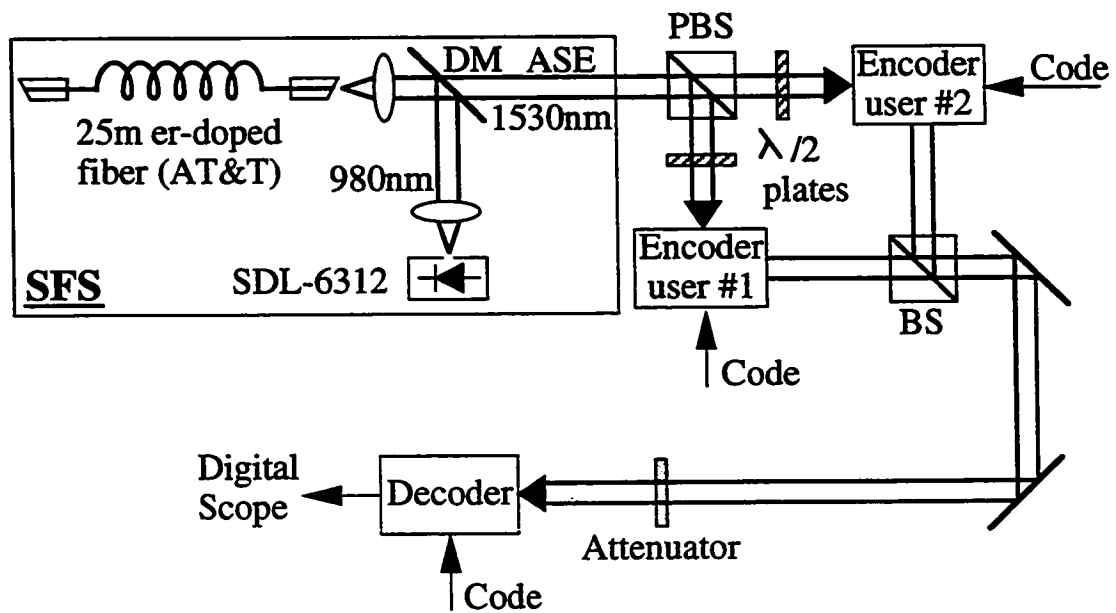
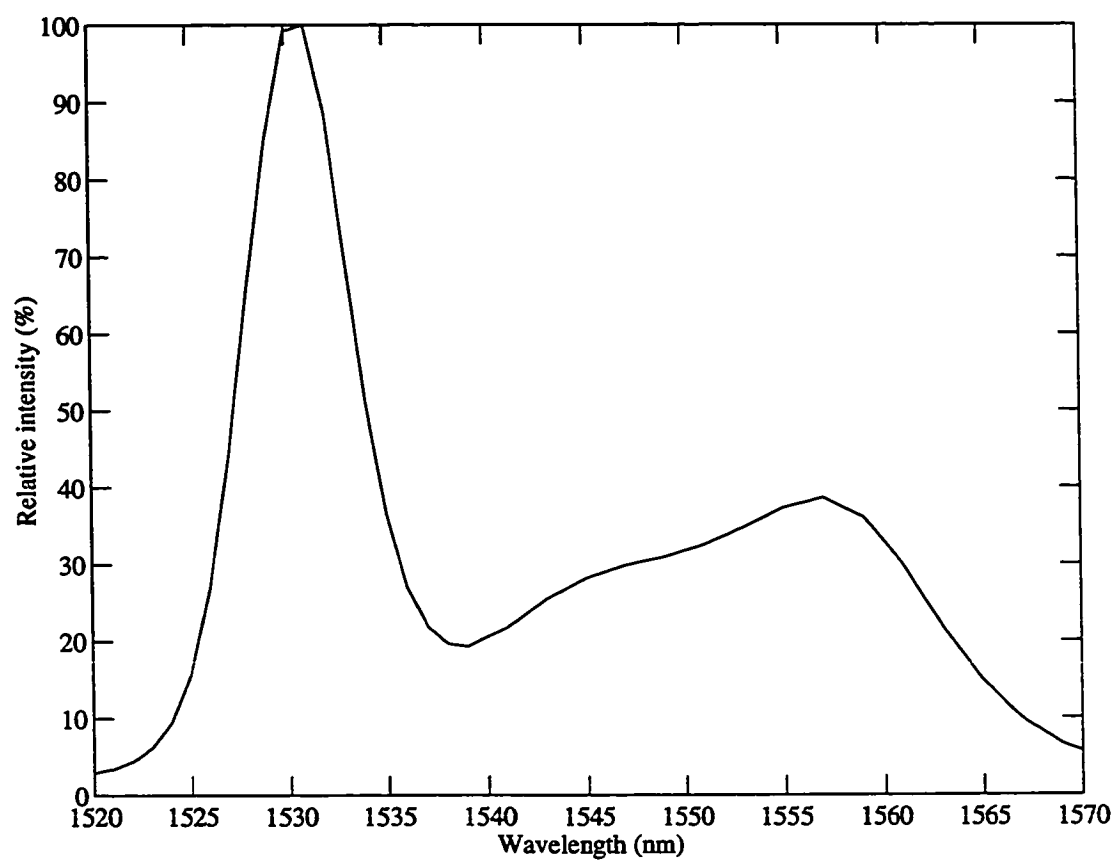


Figure 6.1 Experimental setup of the spectral amplitude CDMA system prototype.

wide spectrum centered around 1550 nm. As shown in Figure 6.2, the ASE spectrum is highly non-uniform. It has a dominant spectral peak at 1530 nm and a broad, lower peak at 1555 nm. About 10 nm of bandwidth around the 1530 nm wavelength were encoded in the prototype system. A polarization beam splitter (PBS) splits the unpolarized ASE input beam into two orthogonal, linearly polarized output beams, forming two light sources for a two-user configuration. The potential instability of the polarized beam intensities was a concern; however no instability was detected with this light source configuration. The two polarized outputs were sent to the half-wave plates that rotate the input beam polarizations to match the TM mode of the encoder gratings for maximum diffraction efficiency into the first order. The outputs of the encoders are combined by a non-polarization beam splitter (BS) to form a two-user channel that is sent to the decoder for measurement of the correlations of the codes and the multiple access interference. Figure 6.3 shows the block diagrams of the encoder (a) and decoder (b) configurations that utilize the spectrum processor. In the experiment, the outputs of the photodiodes in the decoder were also monitored separately by a digital oscilloscope to allow measurements of each photocurrent as well as the various effects on the balanced configuration.

The configuration of the grating-based spectrum processor is depicted in Figure 6.4. The planar holographic grating, which has a 1200 grooves/mm ruling density, operates at about  $3.6^\circ$  off Littrow at 1530 nm to provide beam clearance from the optics. The first-order efficiency of the grating is better than 90% in the



**Figure 6.2** ASE spectrum of erbium-doped SFS.

In the prototype system, about 10 nm of bandwidth centered around the 1530 nm spectral peak were encoded.

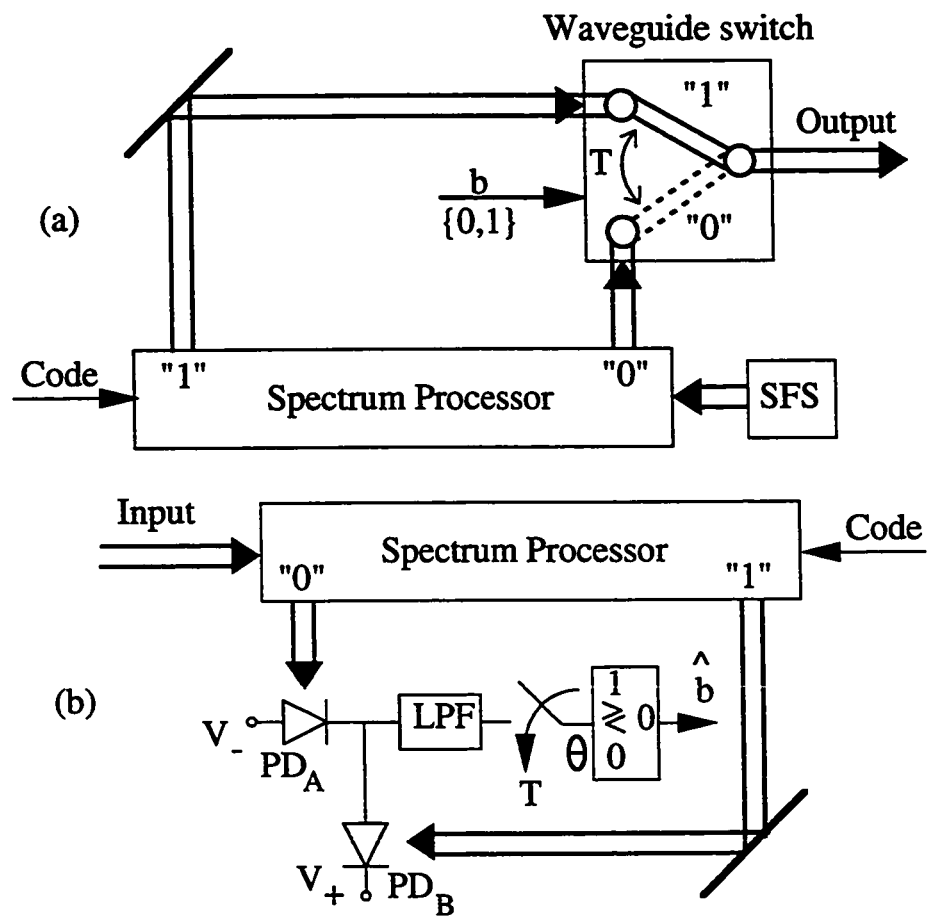


**Figure 6.3** Encoder and decoder configurations.

The spectrum processors are identical for both the encoder (a) and the decoder (b).

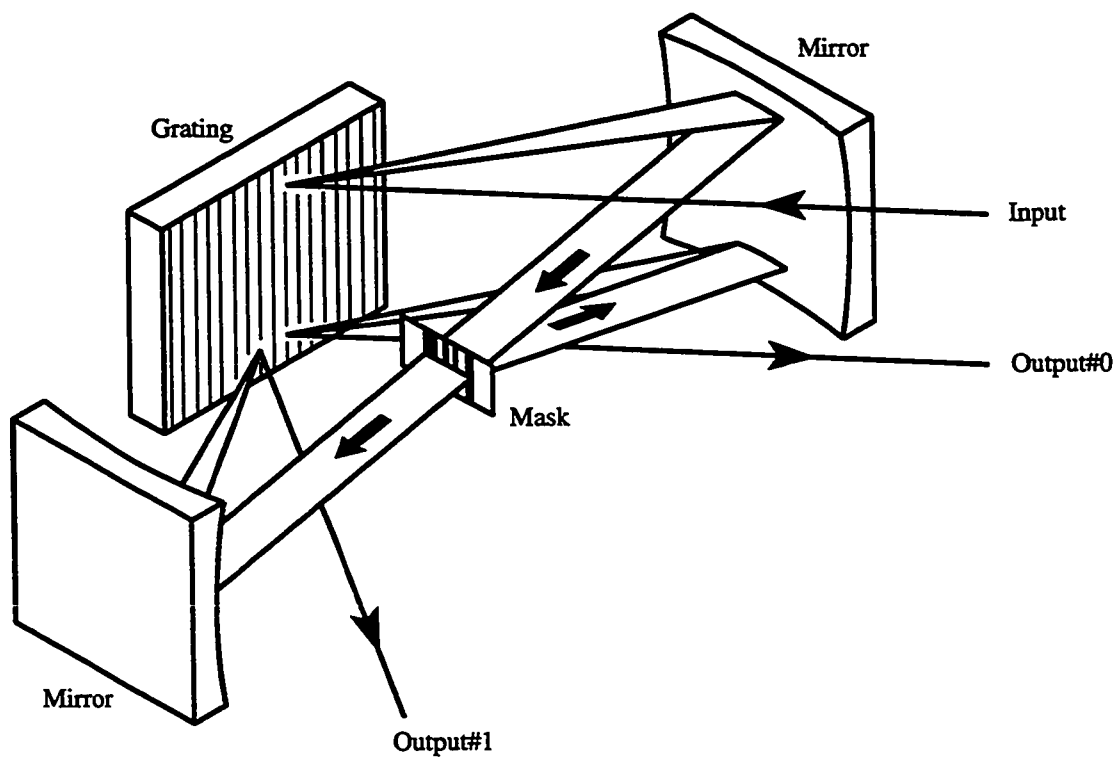


**Figure 6.4** Geometrical configuration of the spectrum processor.  
The spectral responses of the two outputs are complement of one another.

TM mode. The spectral components of the input beam are angularly dispersed from the grating and arrive at the spherical mirror to be focused onto an amplitude mask positioned on the focal plane of the mirror. The source spectrum is displayed as a horizontal stripe of  $30\text{ }\mu\text{m}$  in height at the mask plane. The mask patterns were photographically etched on a quartz window that had been coated with aluminum via evaporation. This produces clear and reflective stripes or chip patterns on the aluminum coated window. The portion of the beam reflected from the mask returned to the spherical mirror and was redirected back to the grating to form a collimated beam denoted “Output#0”. The transmitted portion of the beam continues toward a second, identical spherical mirror and was also redirected back to the same grating to form a second collimated beam denoted “Output#1”. Thus, the transfer functions of the spectrum processor outputs are the spectral complements of each other as required by Figure 2.7. The optical configuration of Figure 6.4, however, is much more simplified and compact. Notice that among the possible realizations of the spectrum processor, the configuration that has been described can be 3 dB more efficient in the use of the input optical power.

The pattern of the amplitude masks is based on the 2-tuple unipolar code, say,  $(U, \bar{U})$ , that was obtained from the bipolar code  $X$  in the manner described in Chapter 2. The clear stripes correspond to the “1’s” of the concatenated unipolar codeword  $U \oplus \bar{U}$  and the reflective stripes correspond to the “0’s”. Thus not only are the transfer functions of the spectrum processor outputs spectral complements,

but also each encoded beam has an anti-periodic characteristic:

$$A(i + N) = \overline{A(i)}, i = 1, 2, \dots, N. \quad (6.1)$$

$A(i) \in \{1, 0\}$  denotes the clear or reflecting amplitude stripes on the mask that correspond to the encoded spectrum as illustrated in Figure 5.2.

In the experiment, bipolar Walsh codes were employed so that encoder and decoder characteristics could be determined without consideration of the codes. Since the codes are orthogonal, deviations from the ideal correlation and MAI rejection provide a measure of the performance of the encoder and decoder apparatus. Figure 6.5 shows the example mask patterns corresponding to three length-16 Walsh codes used in the experiments. The width of each spectral chip was varied to compensate for the non-uniform spectrum of the ASE, so that the power per chip is constant as required by the encoding. The black and shaded chips correspond to  $A(i)$  being 1 and 0, respectively. They correspond to the transmission and reflection chips on the mask. Figure 6.6 shows the enlarged patterns of the encoder and decoder masks for the three unipolar codes, A1, B1, C1, and their complements, A0, B0, C0. The suffixes 1 and 0 denote the encoding of symbol “1” and “0”, respectively. The black, center stripe and the single narrow vertical strips were included for alignment purpose. The masks were mounted on vertical translation stages to allow successive changes of codes during the measurement.

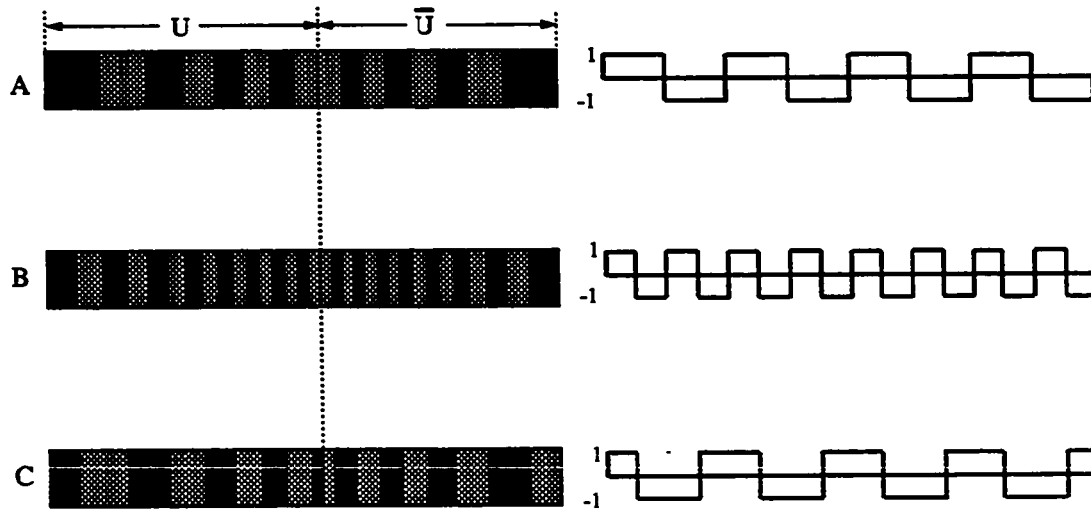


**Figure 6.5** Spectral amplitude code patterns.

The spectral codes (left) are obtained from the corresponding bipolar Walsh codes (right). The widths of the spectral chips were varied to compensate for the non-uniform source spectrum.



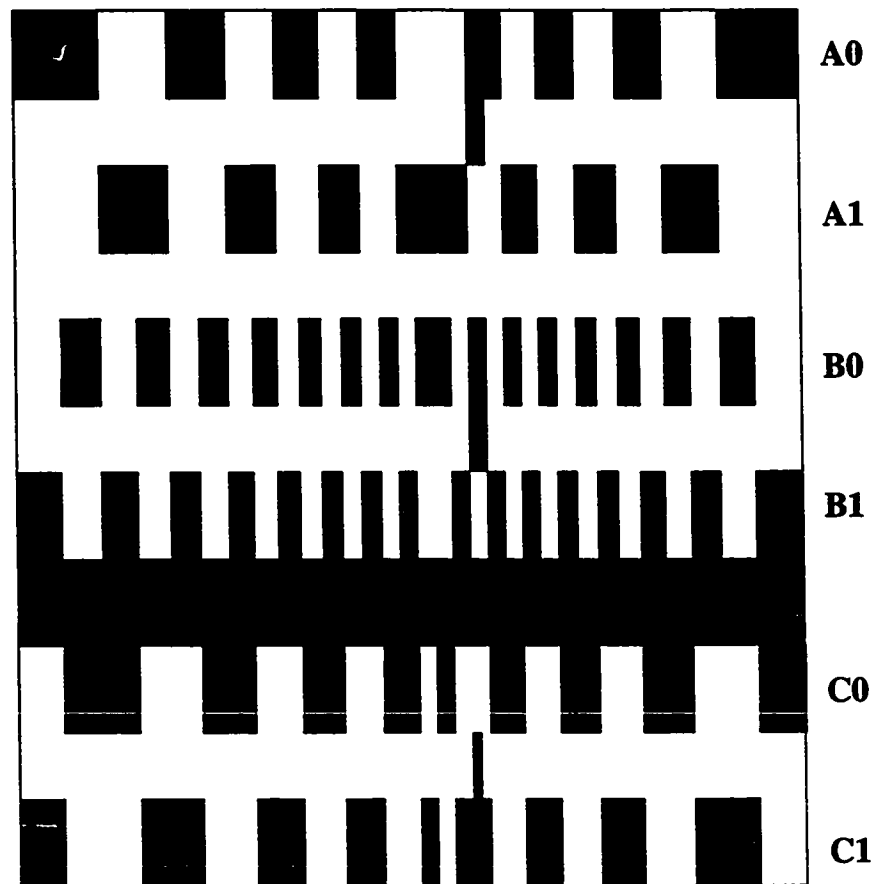


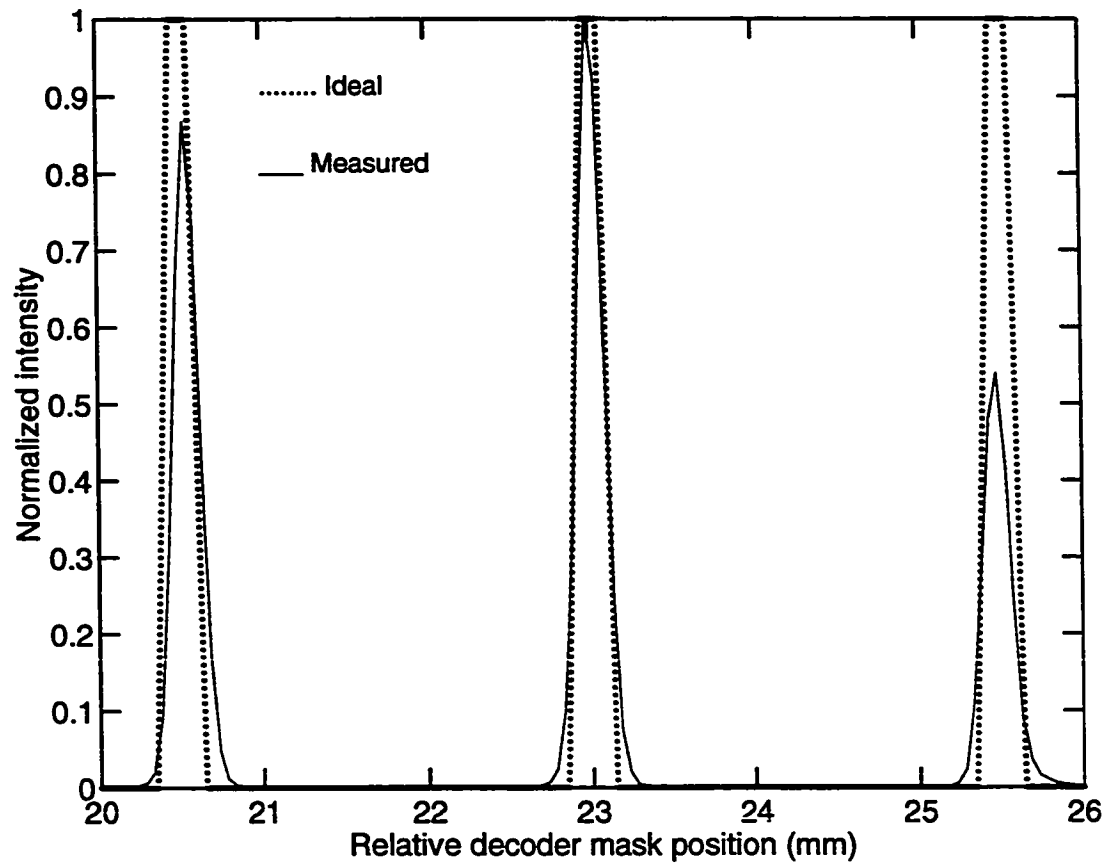
**Figure 6.6** Amplitude mask patterns.

The encoded linewidth was 10 nm. The amplitude patterns of the spectral codes and its complements are shown. The clear, center stripe and vertical strips are for alignment purposes. The widths of the spectral chips are varied to compensate for the non-uniform source spectrum.

## 6.2 System Characterization

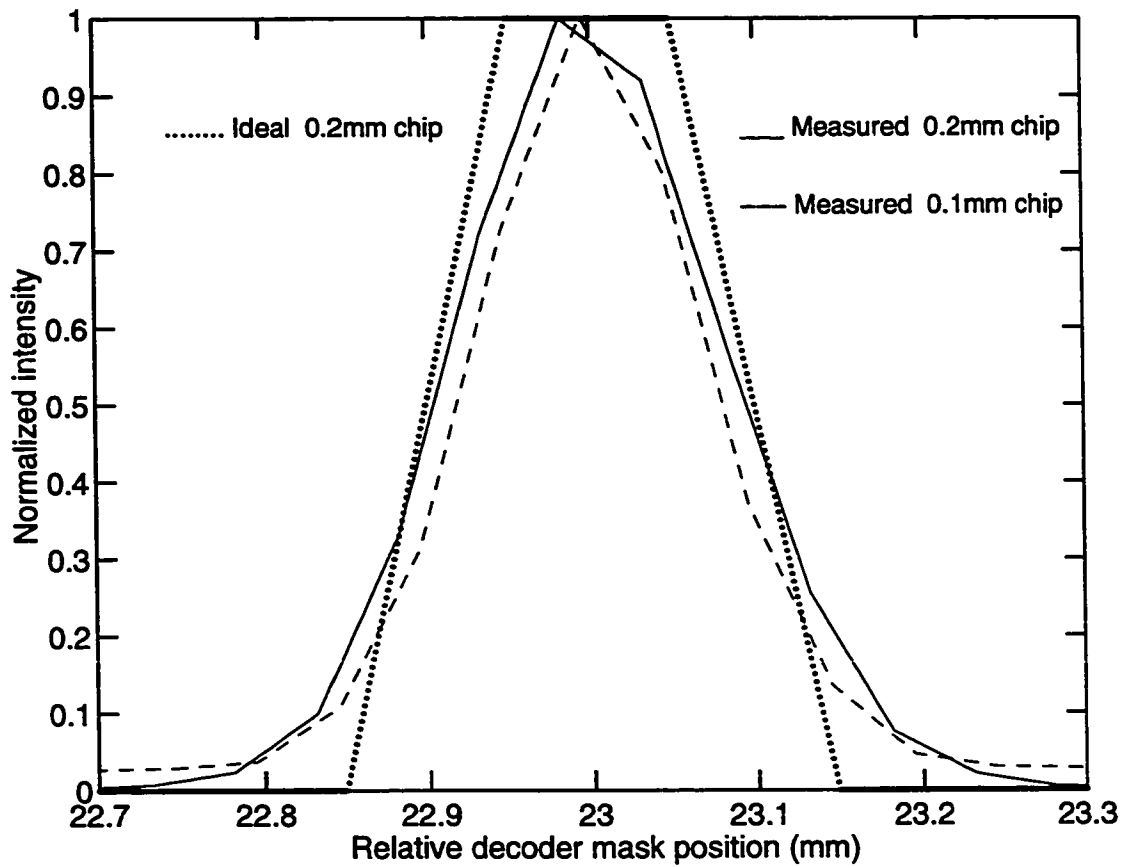
For proper operations, the encoder and decoder should have matched dispersion characteristics. The minimum chip width is established by the spectral resolution of the spectrum processor. We determined these quantities with a back-to-back measurement of the apparatus using an encoder mask pattern consisting of three  $200\text{ }\mu\text{m}$ -wide chips positioned at  $2.5\text{ mm}$  apart. The decoder mask consists of a single  $100\text{ }\mu\text{m}$ -wide chip. Figure 6.7 shows the transmitted optical intensity through the decoder mask as the decoder chip scans across the  $5.0\text{ mm}$  width. The expected calculation shows that the linear dispersion of the combined encoder/decoder apparatus has an rms distortion of about  $30\text{ }\mu\text{m}$  over the  $5.0\text{ mm}$  distance, or less than 1%. The difference in the relative amplitudes of the peaks is due to the non-uniform source spectrum. Figure 6.8 shows the detail scans for the encoder chips of  $200\text{ }\mu\text{m}$  and  $100\text{ }\mu\text{m}$  wide. The resolution of the system is seen to be about  $200\text{ }\mu\text{m}$  at FWHM: the reduction in the size of the scanned chip is marginal and nowhere near the factor of two that is expected when the width of the encoder chip was reduced from  $200\text{ }\mu\text{m}$  to  $100\text{ }\mu\text{m}$ .

Figure 6.9 shows the power spectrum of the optical signal propagated through the clear, center stripe of the encoder and sampled with a single  $100\text{ }\mu\text{m}$  chip at the decoder. The measured spectrum corresponds to about  $11\text{ nm}$  of bandwidth around the  $1530\text{ nm}$  spectral peak of the ASE as verified by an independent measurement of the ASE spectrum with a spectrometer. The results indicate that the linear disper-



**Figure 6.7** Relative dispersion of the encoder/decoder system.

The relative positions of the encoder chips seen at the decoder demonstrate that the rms distortion across a 5.0 mm width is less than 1.0%.



**Figure 6.8** Resolution of the encoder/decoder system.

Detail scans by a  $100\text{ }\mu\text{m}$ -wide decoder chip for the encoding chips of  $200\text{ }\mu\text{m}$  and  $100\text{ }\mu\text{m}$ . The resolution of the system is estimated to be about  $200\text{ }\mu\text{m}$  FWHM.

sion of the system is about 1 nm/mm. The resolution of the prototype system can be seen to exceed that of the spectrometer. Based on a polynomial fit to the measured spectrum, the variable widths of the spectral chips were computed so that the optical power in each chip is the same across the 10 nm bandwidth of the encoded spectrum. The smallest chip at the peak of the spectrum was limited to the 200  $\mu\text{m}$  resolution. Figure 6.10 shows an example encoded spectrum for code C1 as measured at the decoder that illustrates the chip compensation technique: the chips are progressively wider as the spectral power diminishes from the peak wavelength. Notice that the encoded spectrum lines up quite well with the decoder's amplitude mask. This indicates the correct alignment of the optics so that the encoder and decoder apparatus are optically matched in terms of the dispersion characteristics, a condition crucial to the proper operation of the system. This alignment objective is facilitated with the cavity-like configuration of the spectrum processor geometry.

### 6.3 Measurements

We measured the correlations between the transmitter and receiver codes with the single-user configuration by blocking one of the encoded beams to the non-polarization beam splitter. The decoder mask was sequentially set to a particular code, while the codes on the encoder mask were successively selected for transmission so that the correlation measurements between all the codes could be performed. For MAI measurements, both beams from the two encoders were sent to the decoder, forming

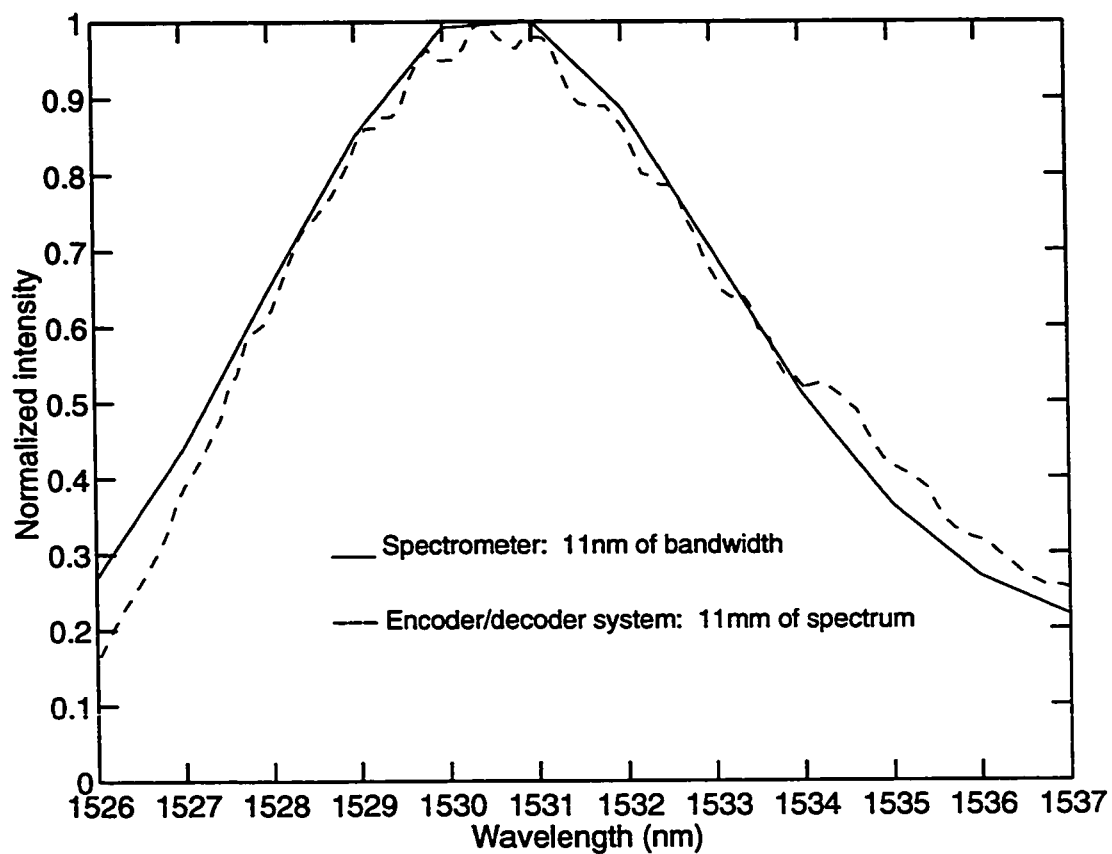


**Figure 6.9** ASE spectrum measurements.

Independent measurements of the ASE spectrum with the prototype system and a spectrometer: the prototype results correspond to a 11 mm wide spectrum on the mask and centered at 1530 nm. The results of the two measurements show that the linear dispersion of the system is about 1.0 nm/mm. Notice the high resolution measurements with the prototype system relative to the spectrometer.

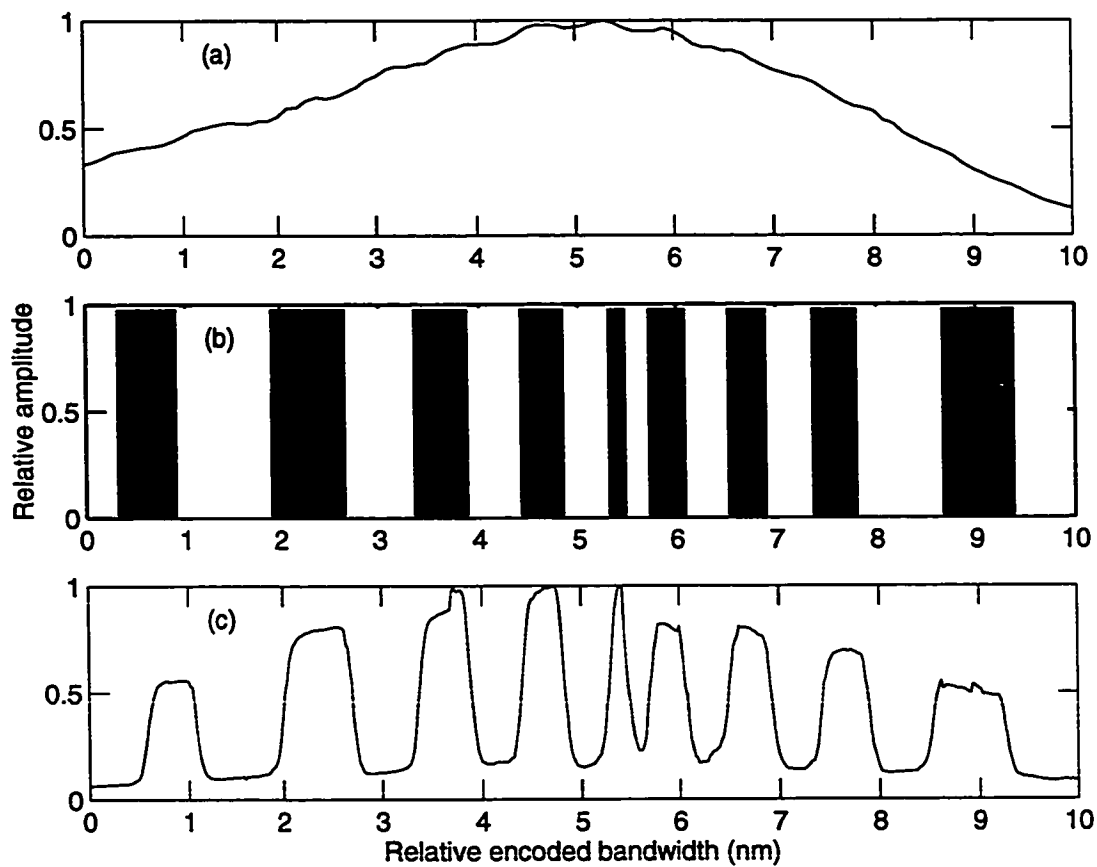


**Figure 6.10** Encoded and decoded ASE spectra.

Source spectrum (a), encoder mask for code C1 (b), and decoder spectrum (c). The decoder spectrum lines up with the encoder mask, indicating that the encoder and the decoder are optically matched in terms of dispersion, a condition crucial for proper operation.

a two-user system. The decoder mask was selected to receive the code of the desired user, while the codes of the interfering user were successively selected for transmission. By sequentially changing the codes of the desired user on the mask, the MAI effect of the codes can be measured. The input power to the decoder is adjusted by an attenuator to prevent detector saturation. Since the correlations and MAI of the codes can be measured without symbol modulation, the measurement bandwidth was less than 100 KHz for an SNR better than 40 dB. The power levels of the two users were kept comparable to one another by adjusting the half-wave plates, effectively varying the efficiency of the encoders so that the output beams have the same intensity.

## 6.4 Results

Figure 6.11 shows the measured correlations of the spectral codes. The voltage waveforms, recorded by the digital scope and displayed in plots A, B and C, are the outputs of the decoder and correspond to the decoder mask that was selected to receive A1, B1, and C1, respectively. It can be seen that when the transmitter codes are matched to the receiver codes, large autocorrelation magnitudes with the proper polarity are detected. Transmitter codes that are not matched to the receiver codes result in small crosscorrelation magnitudes. Since the codes are orthogonal by design, the crosscorrelations should ideally be zero. Thus, the residue values provide an overall measure of the performance of the encoder and decoder apparatus. In this case the crosscorrelation values are about 7% or less relative to the autocorrelation



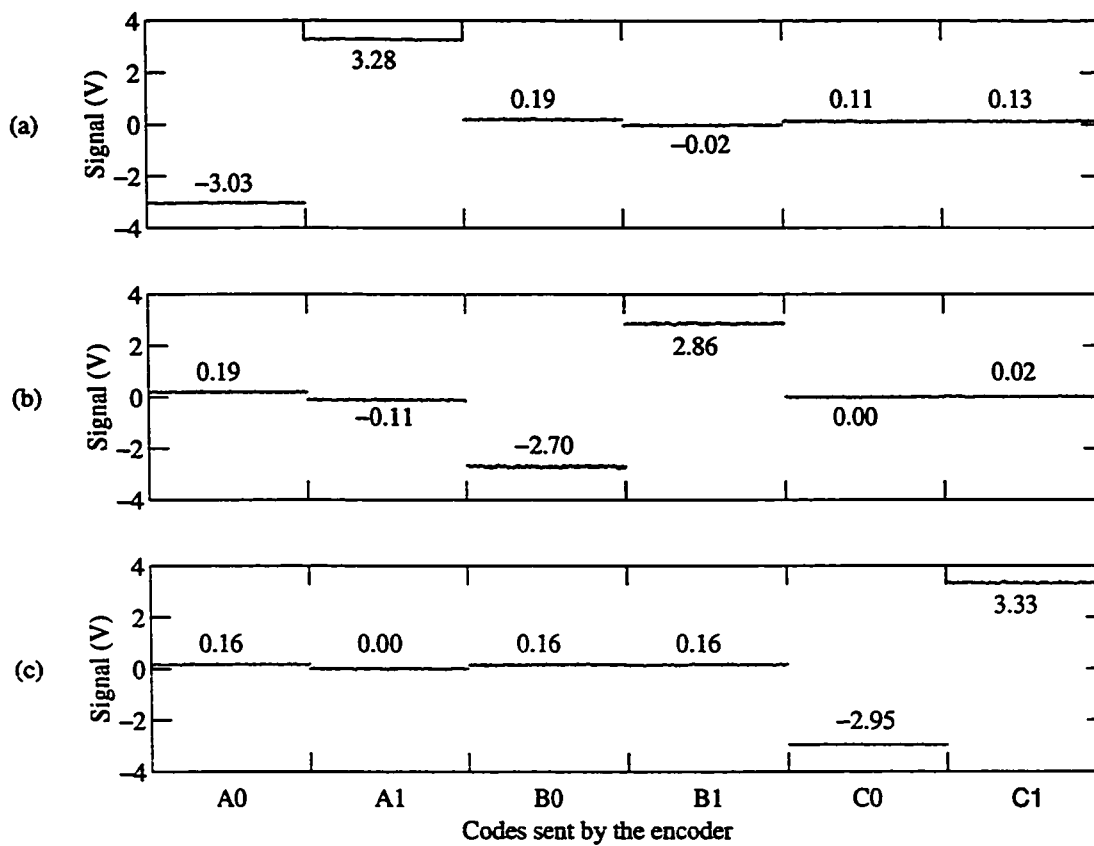


**Figure 6.11** Correlation of the spectral codes.

Measured correlations between the spectral codes: (a) decoder set to A1, (b) decoder set to B1, (c) decoder set to C1. The binary symbol values from the desired user can be recovered with a threshold operation.

values. The good contrast verifies the modulation and detection principles described in Chapter 2. It shows that the binary symbol can be recovered with an appropriate threshold operation on the decoder output.

Figure 6.12 shows the effect of MAI on the decoder output in the presence of another user. The voltage waveforms displayed in plots A and B correspond to the desired user's codes that were selected to be B1 and C1, respectively <sup>†</sup>. As we might have expected, the receiver cannot discriminate the desired user against the interfering user if their codes are matched. The signal level is increased if the interference codes are the same as the desired codes; it is reduced if they are complement of one another. This also provides the evidence that the two encoders and the decoder have been properly aligned so that they are optically matched. It can be seen from Figure 6.12 that an interfering user has little effect on the average signal of the desired user if their codes are not matched. The apparent change in the voltage signals for unmatched codes are due to a slow drift in the systems during the measurement. The magnitude of the MAI, obtained as the difference between the detected signals for the two-user and single user configurations, is about 10% or less relative to the desired signals of the single user. This demonstrates the MAI rejection capability of the receiver in a multi-user situation.

---

<sup>†</sup>Because of the physical arrangements of the two encoder masks, code A could not be examined in a two-user configuration for the MAI effect.

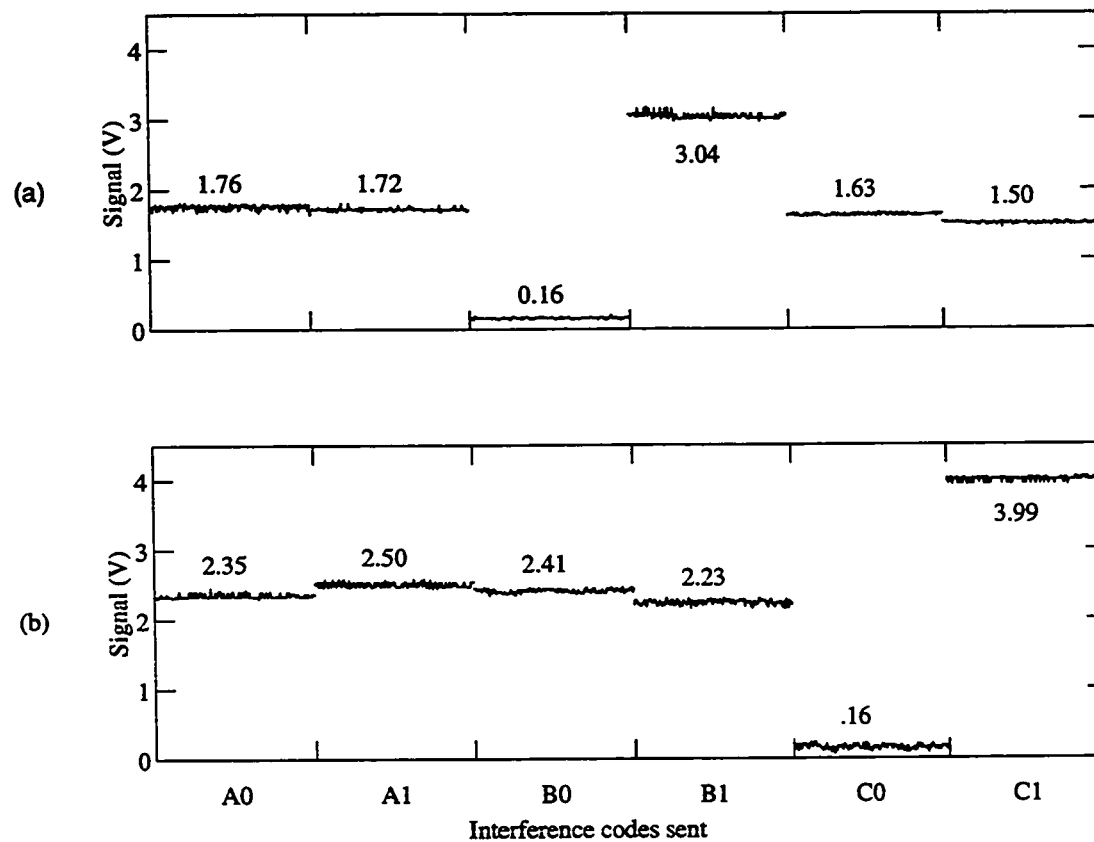


**Figure 6.12** Effect of the multiple-access interference.

The rejection of MAI is demonstrated with the decoder set to B1 (a), the decoder set to C1 (b). The interfering user has little effect on the desired user unless their codes are matched.

## 6.5 Discussions

In spectral amplitude CDMA application, performance of the encoder and decoder is characterized by the code length, or the number of resolvable chips at the amplitude mask plane. The size of a resolvable chip depends on the wavelength resolution,  $\mathcal{R}$ , and linear dispersion,  $\mathcal{D}$ , of the spectrum processor:

$$\mathcal{R} = \frac{2d \cos \theta}{\pi w} \lambda, \quad (6.2)$$

$$\mathcal{D} = \frac{d \cos \theta}{f}, \quad (6.3)$$

where  $d = 1/1200$  mm is the spacing of the grating rules,  $\theta = 70.9^\circ$  is the angle of the diffracted beam at the grating for an incident beam angle of  $63^\circ$  at 1530 nm,  $w = 3.0$  mm is the input beam radius and  $f = 300$  mm is the focal length of the mirror. The wavelength resolution is thus about 0.09 nm. The linear dispersion is the change in wavelength per unit distance along the horizontal spectrum at the mask; it is about 0.91 nm/mm for the above parameter values. The measured dispersion of about 1 nm/mm from Figure 6.9 is thus slightly larger than the designed value. The chip resolution  $\Delta$  at the mask is given by the ratio of  $\mathcal{R}$  and  $\mathcal{D}$ :

$$\Delta = \frac{2f\lambda}{\pi w}, \quad (6.4)$$

This gives a chip resolution of about  $100 \mu\text{m}$  on the mask from the above parameter values. The measured resolution of  $200 \mu\text{m}$ , as shown in Figure 6.8, indicates that the prototype system performs reasonably well in terms of the achievable resolution,

being only a factor of 2 from the diffraction limited performance. Nevertheless, using a code that is twice as long for the chip width of highest resolution of  $100\text{ }\mu\text{m}$ , we found that the contrast of the correlation values is rather poor in comparison to the shorter codes. This is consistent with the limited resolution and was clearly observed to result from the overlapping of the spectra between the adjacent, higher resolution chips in the experiment. It is clear from (6.2) or (6.4) that the resolution can be improved easily by doubling the beam size to  $12.0\text{ mm}$  without making the optics excessively large.

We note that the broadband nature of the source spectrum contributes to limiting the number of resolvable chips. This is because with the broadband spectrum being a continuum, the spectral energy at the chip boundary cannot be fully isolated within one chip. This effect adds to the crosstalk between the adjacent chips. The crosstalk can be reduced by introducing absorbing, uniform guard bands between the spectral chips. We expect therefore that the finite contrast in the correlation measurements, as well as the MAI results, will improve with the use of guard bands. This however will complicate the fabrication of the mask, besides reducing the encoded portion of the spectrum and hence the code length.

Finally, it is obvious that the length of code can be made longer by encoding more spectrum. Thus there is a need to improve the uniformity of the source spectrum. With a wider usable portion of the source spectrum, the distortion in the linear dispersion could be problematic. The distortion is caused in part by the geometry of

the spectrum processor that employs the spherical mirrors for focusing off-axis beams. This inherent distortion can be eliminated with shaped mirrors or other compensation. Additionally, with a wider encoded spectrum and a large beam size, the third order aberration of the mirrors could place a limit on the achievable resolution due to the limited spot size of the focus, or spectrum stripe, that can be achieved on the mask. Accurate analysis of the optical system is required to determine these effects and minimize them.

## **6.6 Summary**

We have implemented an optical CDMA system prototype that demonstrates all-optical application of bipolar codes for spectral amplitude encoding. The prototype employs an erbium-doped SFS, and consists of two encoders and one decoder that were realized with bulk optics and free-space transmission. The correlation measurements have shown that the binary information symbol can be recovered with an appropriate threshold operation. The multiple-access interference has been shown to be rejected in a multi-user situation. Measurements on the encoder and decoder apparatus have identified key parameters that influence the performance of the system. The prototype results demonstrate the feasibility of the modulation and detection principles that have been developed in Chapter 2. To our knowledge, the system is the first experimental demonstration of spectral encoding of bipolar codes on an optical channel.

## Chapter 7

### Conclusions

The single-mode optical fiber, with its vast communication bandwidth and extremely low loss characteristics, can be an ideal medium for multiple-access communication networks, such as the LANs. Among the various multiple-access approaches, CDMA has received considerable attention. The application of CDMA communication techniques to the optical domain, however, has not been as successful as in the RF domain. This primarily is due either to a lack of available good codes, or to the complexity of the system. The research that has been described herein addresses both of these issues. We have developed new modulation and detection principles that enable a direct application of the RF codes to the optical domain. This has finally placed optical CDMA on the same footing as its RF counterpart in terms of the utilization of the available spreading codes. The implication of this result is rather significant in that one of the central issues in CDMA systems is the design of good codes. Practical implementations of these principles were considered that retain the inherent advantages offered by the optical domain. The feasibility of the proposed approaches was demonstrated with a CDMA system prototype based on these new ideas. Experimental investigation of the broadband fiber source employed in the pro-

prototype system has verified the statistical description of the photodetector noise. The analysis based on this statistical model has shown that the thermal nature of the broadband source imposes a penalty on the system performance, due to the effect of excess noise associated with such a light source.

There remains many issues that warrant further investigation, as well as new research topics that could be undertaken from this work. The basic ideas behind computing the bipolar correlation in a unipolar system can just as easily be applied to convolution or filtering operations. Thus, these ideas can be extended to signal processing applications that can benefit from all-optical signal processing. Potentially, these operations can be implemented at a very high speed with all-optical approaches.

The performance penalty imposed on spectral amplitude CDMA by the thermal nature of the SFS indicates that its application could be selective. An optimum detector based on the NB statistics for the multi-channel model described in Chapter 2 should improve the performance. However, the improvement is likely to be marginal. This is due to the noise process of photodetection in the optical domain. Since the detector noise is generated by the optical signals themselves, it cannot be reduced or separated once the additive light from different users overlaps due to encoding. This effect can be observed under the multi-user situation in the prototype system described in Chapter 6. The decoder output in Figure 6.12 is clearly noisier than the single user situation shown in Figure 6.11. Thus, it is likely that the improvement will be more substantial either by using coherent source, or by employing noise reduction



techniques [68], [69]. Moreover, since the NB model describes a very noisy communication channel, forward error-correction coding of the data can be profitably employed to combat the channel noise with the available coding gain, when the number of users is large.

The multi-channel model opens up the possibility of code design for multi-channel optical communication. While the bipolar codes have been shown to be applicable for a 2-channel system, there could be advantages to consider codes that are designed specifically for the multi-channel system based on (2.29) and (2.37). Multi-user detection for the multi-channel system is expected to yield high performance with the attendant increase in the receiver complexity. We also note here the intriguing possibility of applying the multi-dimensional codes and the multi-channel concept to the RF domain. The equivalent multi-channel concept in the RF domain can be found in CDMA systems with multi-carrier or frequency diversity modulations [70], [71]. These systems have been shown to be effective in multi-path fading channels or in the rejection of narrow-band interferences. However, the multi-dimensional concept of the spreading codes combined with multi-carrier modulations in such systems has not been suggested nor studied.

The time-domain CDMA should also be considered since it has some advantages over TDMA. Time-encoded optical CDMA should have better tolerance of the fiber dispersion that causes the pulse broadening that is detrimental to optical TDMA. The dual-channel transmission requirement is best realized via time-multiplexing, or

wavelength multiplexing using the two fiber windows at 1300 nm and 1550 nm where commercial components are readily available. Dual polarization approach will not be practical due to the need for polarization control, a difficult proposition at best in a fiber network. Practically, the use of fiber delay lines in the encoder and decoder can be difficult if long codes are used. Clearly techniques will have to be developed to make these components practical, either with fiber or integrated waveguide delay lines. In this respect, the differential configuration of Figure 2.3 should be employed since it can simplify the decoder complexity by eliminating one half of the matched filters and only requires one photodetector. Notice that this also alleviates the balance requirement on the photodetector. In a multi-channel or multi-wavelength system where  $Q$  is large, the possibility of efficient bandwidth utilizations combined with code designs, as alluded to previously, could be an interesting research subject.

A number of issues related to the prototype development is also worth considering. Replacing the various elements with fiber components would make the system more robust and allow symbol modulations for BER measurements. The performance calculations shown in Figure 5.7 can then be validated. The use of a concave diffraction grating can further simplify the optical configuration of the spectrum processor. An accurate analysis of the optical system will be required to determine the optical performance and the limitation of the design. The amplitude mask should be anti-reflection coated to eliminate specular reflections from the transmission chips, as well as incorporating the absorbing guard chips for cross-talk reduction. Alternate realizations

of the mask, such as arrays of quantum-well modulators, deformable micro-mirrors, or spatial light modulators, could make the user codes programmable. Ultimately, photonic integration of the system can potentially make it compact and practical.

The performance analysis of the prototype that includes additional models of the actual hardware components is critical to understanding and designing of the system. This can be studied using the Signal Processing Workstation (SPW) simulation tool. However since the Monte Carlo technique is quite inefficient in the simulation study of systems at low BER, importance sampling techniques will have to be developed. We have extended the results in [72] to study the prototype system that employs an ideal, coherent source. Additional steps to incorporate the thermal source, and the multi-user scenario, have not been done. Finally, it would be very useful to extend the infinitesimal perturbation analysis techniques developed in [73] to the prototype system. This will permit efficient sensitive analysis of CDMA system, as well as optimization of its performance, to the variations of the hardware components or system parameters.

## Bibliography

- [1] M. K. Simon, J. K. Omura, R. A. Scholtz, and B. K. Levitt, *Spread Spectrum Communications*, vol. I, II and III. Rockville, MD: Computer Science Press, 1985.
- [2] M. B. Pursley, *Spread-Spectrum Multiple-Access Communications*. Vienna and New York: In Multi-User Communication Systems, G. Longo ed., 1983.
- [3] A. J. Viterbi, *CDMA: Principles of Spread Spectrum Communication*. Reading, MA: Addison-Wesley, 1995.
- [4] M. B. Pursley, "Performance Evaluation for Phase-Code Spread-Spectrum Multiple-Access Communication – Part I: System Analysis," *IEEE Trans. Commun.*, vol. COM-25, pp. 795–799, Aug. 1977.
- [5] E. Geraniotis and M. B. Pursley, "Error Probabilities for Direct-Sequence Spread-Spectrum Multiple-Access Communications – Part II: Approximations," *IEEE Trans. Commun.*, vol. COM-30, pp. 985–995, May 1982.

- [6] B. Aazhang and H. V. Poor, "Performance of DS/SSMA Communications in Impulsive Channels – Part I: Linear Correlation Receivers," *IEEE Trans. Commun.*, vol. COM-35, pp. 1179–1188, Nov. 1987.
- [7] B. Aazhang and H. V. Poor, "Performance of DS/SSMA Communications in Impulsive Channels – Part II: Hard-Limiting Correlation Receivers," *IEEE Trans. Commun.*, vol. COM-36, pp. 88–97, Jan. 1988.
- [8] G. Turin, "The Effect of Multipath and Fading on the Performance of Direct Sequence CDMA Systems," *IEEE Journal Selected Areas Commun.*, vol. SAC-2, pp. 597–603, July 1984.
- [9] J. Holtzman and L. M. A. Jalloul, "Rayleigh Fading Effect Reduction with Wideband DS/SS," *IEEE Trans. Commun.*, vol. COM-42, pp. 1012–1016, Feb. 1994.
- [10] J. S. Lehnert and M. B. Pursley, "Multipath Diversity Reception of Spread-Spectrum Multiple-Access Communications," *IEEE Trans. Commun.*, vol. COM-35, pp. 1189–1198, Nov. 1987.
- [11] S. Verdu, "Minimum Probability of Error for Asynchronous Gaussian Multiple-Access Channels," *IEEE Trans. Info. Theory*, vol. IT-32, pp. 85–96, Jan. 1986.
- [12] R. Lupas and S. Verdu, "Linear Multiuser Detectors for Synchronous Code Division Multiple-Access Systems," *IEEE Trans. Info. Theory*, vol. IT-35, pp. 123–136, Jan. 1989.

- [13] M. Varanasi and B. Aazhang, "Multistage Detection in Asynchronous Code Division Multiple-Access Systems," *IEEE Trans. Commun.*, vol. COM-38, pp. 509–519, Apr. 1990.
- [14] Z. Xie, R. T. Short, and C. K. Rushforth, "A Family of Suboptimum Detectors for Coherent Multiuser Communications," *IEEE Journal Selected Areas Commun.*, vol. SAC-8, pp. 683–690, May 1990.
- [15] A. Duel-Hallen, "A Family of Multiuser Decision-Feedback Detectors for Asynchronous Code-Division Multiple-Access Channels," *IEEE Trans. Commun.*, vol. COM-43, pp. 421–434, Feb./Mar./Apr. 1994.
- [16] M. B. Pursley and D. V. Sarwate, "Performance Evaluation for Phase-Coded Spread-Spectrum Multiple-Access Communication – Part II: Code Sequence Analysis," *IEEE Trans. Commun.*, vol. COM-25, pp. 800–803, Aug. 1977.
- [17] D. V. Sarwate and M. B. Pursley, "Crosscorrelation Properties of Pseudorandom and Related Sequences," *Proceedings of the IEEE*, vol. 68, pp. 593–619, May 1980.
- [18] F. R. K. Chung, J. Salehi, and V. K. Wei, "Optical Orthogonal Codes: Design, Analysis, and Applications," *IEEE Trans. Info. Theory*, vol. IT-35, pp. 595–604, May 1989.

- [19] H. Chung and P. V. Kumar, "Optical Orthogonal Codes – New Bounds and an Optimal Construction," *IEEE Trans. Info. Theory*, vol. IT-36, pp. 866–873, July 1990.
- [20] G. C. Yang and W. C. Kwong, "Performance Analysis of Optical CDMA with Prime Codes," *Electron. Letters*, vol. 31, pp. 569–570, Mar. 1995.
- [21] M. J. Parham, C. Smythe, and B. L. Weiss, "Code Division Multiple-access Techniques for use in Optical-fibre Local-area Networks," *Electron. Commun. Eng. Journal*, pp. 206–212, Aug. 1992.
- [22] R. A. Griffin, D. D. Sampson, and D. A. Jackson, "Demonstration of Data Transmission Using Coherent Correlation to Reconstruct a Coded Pulse Sequence," *IEEE Photonics Tech. Letters*, vol. 4, pp. 513–515, May 1992.
- [23] J. H. Hui, "Pattern Code Modulation and Optical Decoding – a Novel Code-division Multiplexing Technique for Multifiber Networks," *IEEE Journal Selected Areas Commun.*, vol. SAC-3, pp. 916–927, Nov. 1985.
- [24] J. Salehi, "Code Division Multiple-access Techniques in Optical Fiber Networks – Part I: Fundamental Principles," *IEEE Trans. Commun.*, vol. COM-37, pp. 824–833, Aug. 1989.

- [25] J. A. Salehi and C. A. Brackett, "Code Division Multiple-access Techniques in Optical Fiber Networks – Part II: Systems Performance Analysis.," *IEEE Trans. Commun.*, vol. COM-37, pp. 834–842, Aug. 1989.
- [26] D. Brady and S. Verdu, "A Semiclassical Analysis of Optical Code Division Multiple Access," *IEEE Trans. Commun.*, vol. COM-39, pp. 85–93, Jan. 1991.
- [27] H. M. H. Shalaby, "Performance Analysis of Optical Synchronous CDMA Communication Systems with PPM Signaling," *IEEE Trans. Commun.*, vol. COM-43, pp. 624–634, Feb./Mar./Apr. 1995.
- [28] S. Verdu, "Multiple-access Channel with Point-process Observations: Optimum Demodulation," *IEEE Trans. Info. Theory*, vol. IT-32, pp. 642–651, Sept. 1986.
- [29] M. B. Pearce and B. Aazhang, "Multiuser Detection for Optical Code Division Multiple Access Systems," *IEEE Trans. Commun.*, vol. COM-42, pp. 1801–1810, Feb./Mar./Apr. 1994.
- [30] D. Zaccarin and M. Kavehrad, "Performance Evaluation of Optical CDMA Systems using Non-coherent Detection and Bipolar Codes," *IEEE Journal of Lightwave Tech.*, vol. LT-12, pp. 96–105, Jan. 1994.
- [31] E. L. Walker, "A Theoretical Analysis of the Performance of Code Division Multiple Access Communications over Multimode Optical Fiber Channels – Part



- I: Transmission and Detection,” *IEEE Journal on Selected Areas Commun.*, vol. SAC-12, pp. 751–761, May 1994.
- [32] N. Karafolas and D. Uttamchandani, “Self-homodyne Code Division Multiple Access Technique for Fiber Optic Local Area Networks,” *IEEE Photonics Tech. Letters*, vol. 6, pp. 880–883, July 1994.
- [33] N. Karafolas and D. Uttamchandani, “Optical CDMA System using Bipolar Codes and Based on Narrow Passband Optical Filtering and Direct Detection,” *IEEE Photonics Tech. Letters*, vol. 7, pp. 1072–1074, Sept. 1995.
- [34] S. Tamura, S. Nakano, and K. Okazaki, “Optical Code-multiplex Transmission by Gold Sequences,” *IEEE Journal of Lightwave Technology*, vol. LT-3, pp. 121–127, Feb. 1985.
- [35] T. O’Farrell and S. Lochmann, “Performance Analysis of an Optical Correlator Receiver for SIK DS-CDMA Communication Systems,” *Electron. Lett.*, vol. 30, pp. 63–65, Jan. 1994.
- [36] D. Zaccarin and M. Kavehra, “New Architecture for Incoherent Optical CDMA to Achieve Bipolar Capacity,” *Electron. Lett.*, vol. 30, pp. 258–259, Feb. 1994.
- [37] L. Tancevski, L. Bazgaloski, I. Andonovic, and J. Budin, “Incoherent Asynchronous Optical CDMA using Gold Codes,” *Electron. Lett.*, vol. 30, pp. 721–723, Apr. 1994.

- [38] H. L. V. Trees, *Detection, Estimation, and Modulation Theory: Part I*. New York, NY: John Wiley & Sons, 1968.
- [39] B. Reiffen and H. Sherman, "An Optimum Demodulator for Poisson Processes: Photon Source Detectors," in *Proceedings of the IEEE*, vol. 51, pp. 1316–1320, Oct. 1963.
- [40] I. Bar-David, "Communication under the Poisson Regime," *IEEE Trans. Info. Theory*, vol. IT-15, pp. 31–37, Jan. 1969.
- [41] R. B. Ash, *Real Analysis and Probability*. San Diego, CA: Academic Press, 1972.
- [42] A. Weiner, J. Heritage, and J. Salehi, "Encoding and Decoding of Femtosecond Pulses," *Optics Letters*, vol. 13, pp. 300–302, Apr. 1988.
- [43] M. Brandt-Pearce, *High Throughput Optical Code-Division Multiple-Access Communication Systems*. PhD thesis, Rice University, Apr. 1993.
- [44] D. Zaccarin and M. Kavehrad, "An Optical CDMA System Based on the Spectral Encoding of LED," *IEEE Photonics Tech. Letters*, vol. 4, pp. 479–482, Apr. 1993.
- [45] M. Kavehrad and D. Zaccarin, "Optical Code-division-multiplexed Systems based on Spectral Encoding of Noncoherent Sources," *IEEE Journal Lightwave Tech.*, vol. LT-13, pp. 534–545, Mar. 1995.

- [46] P. F. Wysocki, M. J. F. Digonnet, and B. Y. Kim, "1.55  $\mu\text{m}$  Broadband Fiber Sources Pumped near 980 nm," *SPIE Fiber Laser Sources and Amplifiers II*, vol. 1373, pp. 66–77, 1990.
- [47] P. R. Morkel, R. I. Laming, and D. N. Payne, "Noise Characteristics of High-power Doped-fibre Superluminescent Sources," *Electron. Lett.*, vol. 26, pp. 96–98, Jan. 1990.
- [48] C. L. Mehta, "Theory of Photoelectron Counting," in *Progress in Optics* (E. Wolf, ed.), vol. 8, pp. 375–440, Amsterdam: North-Holland, 1970.
- [49] J. W. Goodman, *Statistical Optics*. New York, NY: John Wiley & Sons, 1985.
- [50] T. Li and M. C. Teich, "Bit-Error Rate for a Lightwave Communication System Incorporating an Erbium-doped Fibre Amplifier," *Electron. Lett.*, vol. 27, pp. 598–600, Mar. 1991.
- [51] P. G. Hoel, S. C. Port, and C. J. Stone, *Introduction to Probability Theory*. Boston, MA: Houghton Mifflin, 1971.
- [52] H. Hodara, "Statistics of Thermal and Laser Radiation," *Proceeding of the IEEE*, vol. 53, pp. 696–704, July 1965.
- [53] J. S. Lee, Y. C. Chung, T. H. Wood, J. P. Meester, C. H. Joyner, C. A. Burrus, J. Stone, H. M. Presby, and D. J. Digiovanni, "Spectrum-sliced Fiber Ampli-

- fier Light Source with a Polarization-insensitive Electroabsorption Modulator,” *IEEE Photonics Tech. Letters*, vol. 6, pp. 1035–1038, Aug. 1994.
- [54] F. A. Johnson, T. P. McLean, and E. R. Pike, “Photon-counting Statistics,” in *Physics of Quantum Electronics* (P. L. Kelley, B. Lax, and P. E. Tannenwald, eds.), pp. 706–714, NY: McGraw Hill, 1966.
- [55] D. B. Scarf, “Measurements of Photon Correlations in Partially Coherent Light,” *Phys. Rev.*, vol. 175, pp. 1661–1668, Nov. 1968.
- [56] B. Saleh, *Photoelectron Statistics*. Berlin: Springer-Verlag, 1978.
- [57] D. H. Johnson and D. E. Dudgeon, *Array Signal Processing*. Englewood Cliffs, NJ: Prentice Hall, 1993.
- [58] E. Desurvire, “Spectral Noise Figure of  $Er^{3+}$ -doped Fiber Amplifier,” *IEEE Photonics Tech. Letters*, vol. 2, pp. 208–210, Mar. 1990.
- [59] D. D. Sampson and W. T. Holloway, “100mW Spectrally-uniform Broadband ASE Source for Spectrum-sliced WDM,” *Electron. Lett.*, vol. 30, pp. 1611–1612, Sept. 1994.
- [60] D. D. Sampson and W. T. Holloway, “Transmission of 622 Mbits/s Spectrum-sliced WDM Channel over 60 km of Nondispersion-shifted Fibre at 1550 nm,” *Electron. Lett.*, vol. 30, pp. 1767–1768, Oct. 1994.

- [61] J. S. Lee, Y. C. Chung, and D. J. Digiovanni, "Spectrum-Sliced Fiber Amplifier Light Source for Multichannel WDM Applications," *IEEE Photonics Tech. Letters*, vol. 5, pp. 458–461, Dec. 1993.
- [62] L. Nguyen, B. Aazhang, and J. F. Young, "All-optical CDMA with Bipolar Codes," *Electron. Lett.*, vol. 31, pp. 469–470, Mar. 1995.
- [63] K. Liu, "Noise Limits of Spectral Slicing in Wavelength-Division Multiplexing Applications," in *Optical Fiber Conference '92*, vol. poster WM7, (San Jose, CA), p. 174, Feb. 1992.
- [64] E. D. J. Smith, P. T. Gough, and D. P. Taylor, "Noise Limits of Optical Spectral-Encoding CDMA Systems," *Electron. Lett.*, vol. 31, pp. 1469–1470, Aug. 1995.
- [65] D. J. Warren and J. B. Thomas, "Signal-to-Noise Ratio and Central Limit Theorem Considerations in Non-Gaussian Detection," in *23rd Annual Allerton Conference on Communication, Control, and Computing*, (Urbana, IL), pp. 35–44, 1985.
- [66] T. Li and M. C. Teich, "Photon Point Process for Travelling-Wave Laser Amplifiers," *IEEE Journal of Quantum Electronics*, vol. JQE-29, pp. 2568–2578, Sept. 1993.

- [67] A. A. Al-Orainy and J. J. O'Reilly, "Optimized Threshold Setting for Performance Enhancement of Spectrum Sliced WDM Systems," in *LEOS '95*, vol. 2, OC6.7, (San Francisco, CA), pp. 63-64, Oct. 1995.
- [68] R. P. Moeller and W. K. Burns, "1.06  $\mu\text{m}$  All-fiber Gyroscope with Noise Subtraction," *Optics Letters*, vol. 16, pp. 1902-1904, Dec. 1991.
- [69] A. J. Keating, W. T. Holloway, and D. D. Sampson, "Feedforward Noise Reduction of Incoherent Light for Spectrum-sliced Transmission at 2.5 Gbs," *IEEE Photonics Tech. Letters*, vol. 7, pp. 1513-1515, Dec. 1995.
- [70] S. Kondo and L. B. Milstein, "Performance of Multicarrier DS CDMA System," *IEEE Trans. Commun.*, vol. 44, pp. 238-246, Feb. 1996.
- [71] E. A. Sourour and M. Kakagawa, "Performance of Orthogonal Multicarrier CDMA in a Multipath Fading Channel," *IEEE Trans. Commun.*, vol. 44, pp. 356-367, Mar. 1996.
- [72] N. B. Mandayam and B. Aazhang, "Importance Sampling for Direct-detection Optical Communication System," *To appear in IEEE Trans. Commun.*
- [73] N. B. T. Mandayam, *A Sample Realization Approach for Optimization of Code Division Multiple Access System*. PhD thesis, Rice University, May 1994.